Electronic Supplementary Information for

Charge-Assisted Hydrogen Bonding in A Bicyclic Amide Cage: An Effective Approach to Anion Recognition and Catalysis in Water

Chengkai Xu, Quy Gia Tran, Dexin Liu, Canjia Zhai, Lukasz Wojtas, Wenqi Liu*

Department of Chemistry, 4202 E. Fowler Ave, University of South Florida, Tampa, FL, 33620, USA

*wenqi@usf.edu

Table of Contents

1. General Method.

All commercially available solvents and chemicals were purchased from Sigma-Aldrich, Fisher Scientific, and Ambeed and used without further purification unless otherwise stated. Water was deionized and micro-filtered through a Milli-Q water filtration system. Reactions were monitored by analytical thin-layer chromatography (TLC) on silica gel 60-F_{254} plates, visualized by an ultraviolet (254 nm) lamp. Microwave reactions were performed using a Biotage Initiator microwave synthesizer. Mettler Toledo XRS105 microbalance with 0.01 mg accuracy was used to measure sample weight, and Eppendorf Research plus micropipettes were used to transfer the solutions. Nuclear magnetic resonance (NMR) spectra were recorded on the Varian Unity Inova 600 MHz spectrometer or Varian Unity Inova 400 MHz system. The chemical shift was presented in ppm and referenced by residual non-deuterated solvent peaks (D_2O: δ = 4.79 ppm, DMSO-d_6: δ = 2.50 ppm, $CDCl_3$: δ = 7.26 ppm). High-resolution mass spectrometry (HRMS) was obtained on Agilent LC-MS QTOF 6540 using an ESI source or Waters Synapt G2 mass spectrometer using an ESI source. UV-Vis absorption spectra were collected by Thermo Scientific Evolution 201 UV/Vis Spectrometer. Flash Column chromatography was performed using a Biotage Selekt system with silica gel (SilicaFlash P60 from SILICYCLE) as the stationary phase. Isothermal titration was performed on the MicroCal iTC_{200} system, and samples were all filtered through a 0.45 μm PTFE filter before use. ITC Data were analyzed on MicroCal iTC_{200} analysis software. Detailed experimental procedures are provided below in the appropriate sections of this supporting information.

2. Synthesis and Compound Characterization

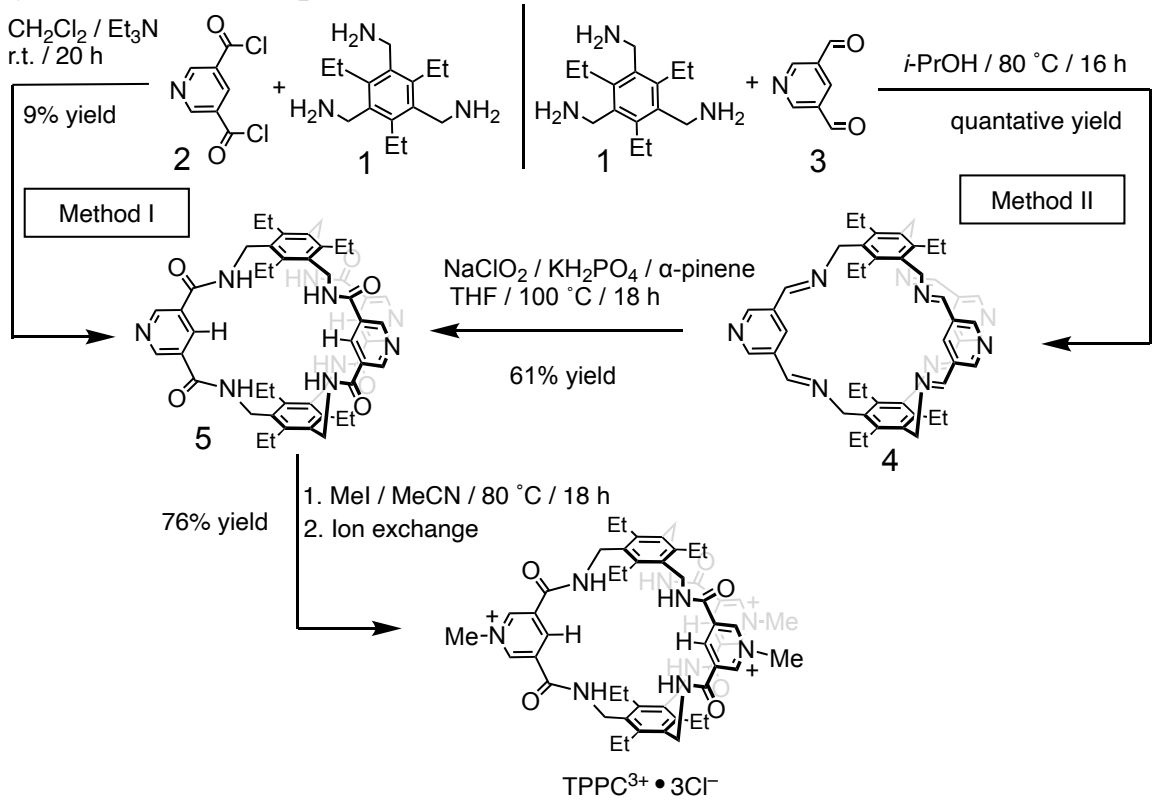

Scheme S1. Synthesis of $TPPC^{3+}$•$3Cl^-$ using conventional high dilution approach (method I) and dynamic approach (method II).

Method I

Et_3N (2 mL, 14.4 mmol, 9.4 equiv.) and dry CH_2Cl_2 (500 mL) were added to a 1 L round-bottom flask. Freshly prepared pyridine-3,5-dicarbonyl dichloride 2 (500 mg, 2.4 mmol, 1.6 equiv.) was dissolved in CH_2Cl_2 (10 mL) and transferred to a 25 mL syringe. (2,4,6-Triethylbenzene-1,3,5-triyl)trimethanamine 1 (382 mg, 1.5 mmol, 1.0 equiv.) was also dissolved in CH_2Cl_2 (10 mL) and transferred to another 25 mL syringe. Both solutions were added to the flask via a syringe pump over 3 hours. The reaction mixture was then stirred overnight. The solvent was removed under reduced pressure, and the residue was purified by flash column chromatography (eluent: CH_2Cl_2/MeOH = 10:1 with 1% Et_3N as an additive). After removing the solvent, the residue was washed with water (5 mL × 3) to afford the amide cage 5 as a white solid (60 mg, 9% yield). ^{1}H NMR (400 MHz, DMSO-d_6) δ 9.07 (d, J = 2.0 Hz, 6H), 8.53 (t, J = 4.7 Hz, 6H), 8.28 (s, 3H), 4.46 (d, J = 5.0 Hz, 12H), 2.83 (q, J = 7.5 Hz, 12H), 1.11 (t, J = 7.4 Hz, 18H). ^{13}C NMR (101 MHz, DMSO-d_6) δ 165.7, 151.6, 145.3, 134.1, 132.6, 130.6, 38.6, 23.1, 17.1. HRMS(ESI) *m/z:* $[M+2H^+]^{2+}$ Calcd for $[C_{51}H_{59}N_9O_6]^{2+}$ 446.7289; found: 446.7309.

Method II

Pyridine-3,5-dicarbaldehyde 3 (50 mg, 0.37 mmol) and (2,4,6-triethylbenzene-1,3,5-triyl)trimethanamine 1 (61 mg, 0.25 mmol) were added to a microwave vial along with isopropanol (5 mL) as the solvent. The vial was sealed, and the reaction mixture was stirred at 80 ˚C overnight. After cooling to room temperature, the solvent was removed under reduced pressure. The resulting white solid showed decent purity and was directly used in the next step without further purification.^{1}H NMR (400 MHz, DMSO-d6) δ 8.96 (d, *J* = 2.0 Hz, 6H), 8.40 (s, 6H), 8.15 (s, 3H), 4.86 (s, 12H), 2.45 (m, 12H), 1.11 (t, *J* = 7.5 Hz, 18H).

Amide cage 5: A microwave vial was charged with imine cage 4 (50 mg, 0.063 mmol), $NaClO_2$ (136 mg, 1.5 mmol, 24 equiv.), KH_2PO_4 (68 mg, 0.5 mmol, 8 equiv.), α-pinene (0.48 mL, 3.0 mmol, 48 equiv.), and dry THF (2.5 mL) as the solvent. The vial was sealed, and the reaction mixture was stirred at 100 ˚C overnight. After cooling to room temperature, the solvent was removed under reduced pressure. The resulting crude product was purified by flash column chromatography (eluent: CH_2Cl_2/MeOH = 10:1 with 1% Et_3N as an additive). The residue was then washed with water (5 mL × 3) to afford the amide cage 5 as a white solid (34 mg, 61%). The ^{1}H NMR spectrum matches the product obtained through Method I.

$TPPC^{3+}$•3Cl^{-}: A microwave vial was charged with amide cage 5 (10 mg, 0.011 mmol), iodomethane (23.0 μL, 0.36 mmol, 33 equiv.), and MeCN (1 mL) as the solvent. The vial was sealed, and the reaction mixture was stirred at 80 ˚C overnight. After cooling to room temperature, the solvent was removed under reduced pressure. The residue was dissolved in DMF, and the counter anion was exchanged by adding KPF_6 (40 mg, 0.22 mmol, 20 equiv.) to the solution. Water was added to precipitate the cage as a white solid, which was isolated by centrifugation. The solid was then redissolved in MeCN and treated with TBACl (61 mg, 0.22 mmol, 20 equiv.). The resulting white solid was isolated by centrifugation and dried under vacuum to yield $TPPC^{3+}$•3Cl^{-} (8.9 mg, 76%). ^{1}H NMR (400 MHz, D_2O) δ 9.51 (s, 3H), 9.41 (s, 6H), 4.61 (s, 12H), 4.49 (s, 9H), 2.59 (q, *J* = 7.0 Hz, 12H), 1.11 (t, *J* = 7.3 Hz, 18H). ^{13}C NMR (101 MHz, D_2O) 162.3, 147.8, 145.6, 139.7, 132.6, 129.6, 49.1, 39.0, 22.6, 15.0. HRMS(ESI) *m/z:* M^{3+} Calcd for $[C_{54}H_{66}N_9O_6]^{3+}$ 312.1707; found: 312.1696. Note: The basic principle of the ion exchange process used in our protocol is that the pyridinium salt, when associated with PF_6^- anions, will precipitate from water and become highly soluble in MeCN. Conversely, when the pyridinium salt is associated with Cl- anions, it will precipitate out from MeCN and become highly soluble in water. By introducing a

large excess of KPF_6, the hydrophobic PF_6^- anion selectively forms a hydrophobic ion pair with the organic pyridinium salt, causing the molecule to precipitate as $TPPC^{3+}•3PF_6^-$ from water. The corresponding $TPPC^{3+}•3PF_6^-$ in MeCN will then precipitate out as $TPPC^{3+}•3Cl^-$ upon the introduction of TBACl.

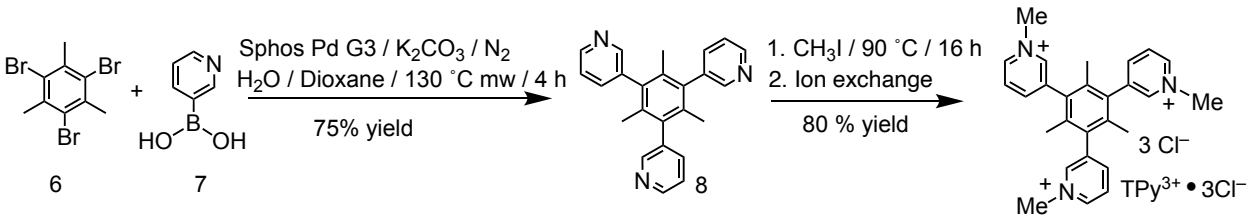

Scheme S2. Synthesis of $TPy^{3+}•3Cl^-$.

Intermediate 8: K_2CO_3 (1.9 g, 14 mmol) was dissolved in a microwave vial prefilled with H_2O (4 mL). To this solution, 1,3,5-tribromo-2,4,6-trimethylbenzene (1.0 g, 2.8 mmol) and pyridin-3-ylboronic acid (1.3 g, 11.2 mmol) were added, followed by the addition of dioxane (12 mL). The reaction mixture was purged with a flow of N_2 for 10 minutes and then sealed with a septum cap. The reaction was heated under microwave irradiation at 130 ˚C for 4 hours. After cooling to room temperature, the organic layer was separated and filtered through a 0.45 μm PTFE syringe filter, and the solvent was removed under vacuum. The remaining residues were washed with MeOH to obtain the product (8) as a white solid (0.74 g, 75% yield). ^{1}H NMR (400 MHz, $CDCl_3$) δ 8.62 (d, J = 4.8 Hz, 3H), 8.51 (t, J = 11.6 Hz, 3H), 7.66 – 7.51 (m, 3H), 7.48 – 7.35 (m, 3H), 1.71 (s, 9H). ^{13}C NMR (101 MHz, $CDCl_3$) δ 150.2, 148.4, 137.1, 136.9, 136.5, 134.8, 123.6, 19.8. HRMS(ESI) *m/z:* M+H^+ Calcd for $[C_{24}H_{22}N_3]^+$ 352.1809; found: 352.1816.

$TPy^{3+}•3Cl^-$: Intermediate 8 (100 mg, 0.28 mmol) was dissolved in MeCN (15 mL). Iodomethane (160 μL, 2.5 mmol) was added to the reaction mixture, which was then heated to 90 ˚C for 16 h. After cooling to room temperature, the solvent was removed under reduced pressure. The remaining residue was dissolved in DMF, and the counter anion was exchanged by adding KPF_6 (2.0 g, 11 mmol) to the solution. Water was added to precipitate $TPy^{3+}•3PF_6^-$ as a white solid, which was isolated by centrifugation. The isolated solid was redissolved in MeCN and treated with TBACl (2.0 g, 7.2 mmol). The resulting white solid was precipitated by centrifugation and dried under vacuum to yield $TPy^{3+}•3Cl^-$ (113 mg, 80% yield).^{1}H NMR (400 MHz, D_2O) δ 8.98 – 8.71 (m, 6H), 8.61 – 8.40 (m, 3H), 8.20 (t, J = 7.1 Hz, 3H), 4.46 (s, 9H), 1.75 (s, 9H). ^{13}C NMR (101 MHz, D_2O) δ 146.7, 145.1, 144.3, 140.5, 136.2, 132.9, 128.3, 48.3, 18.9. HRMS(ESI) *m/z:* M^{3+} Calcd for $[C_{27}H_{30}N_3]^{3+}$ 132.0808; found: 132.0829.

3. Mass Spectrometry

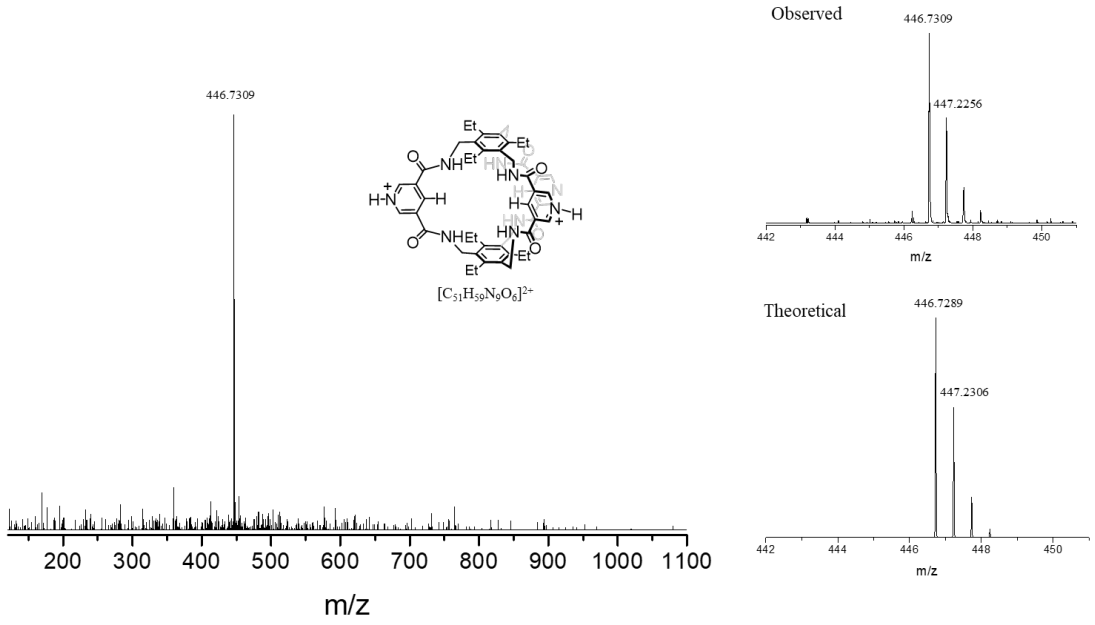

Fig. S1. HRMS (ESI) spectra of the amide cage 5, showing m/z values representing $[5+2H^+]^{2+}$.

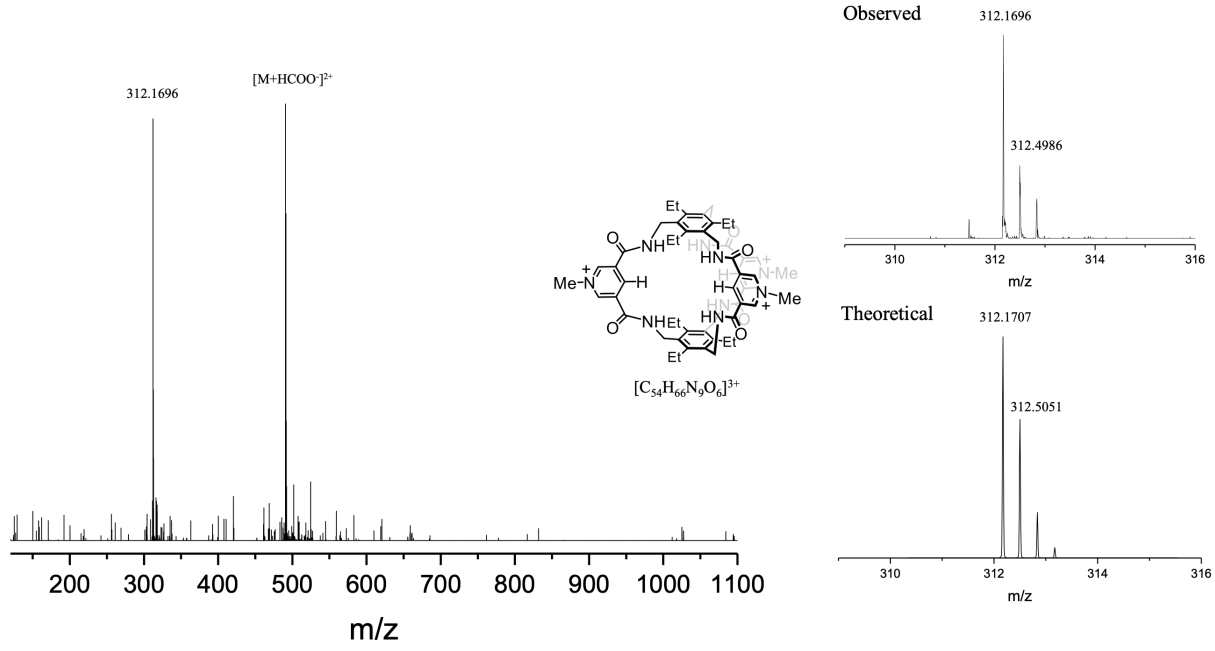

Fig. S2. HRMS (ESI) spectra of $TPPC^{3+}•3Cl^-$ showing m/z values representing $TPPC^{3+}$.

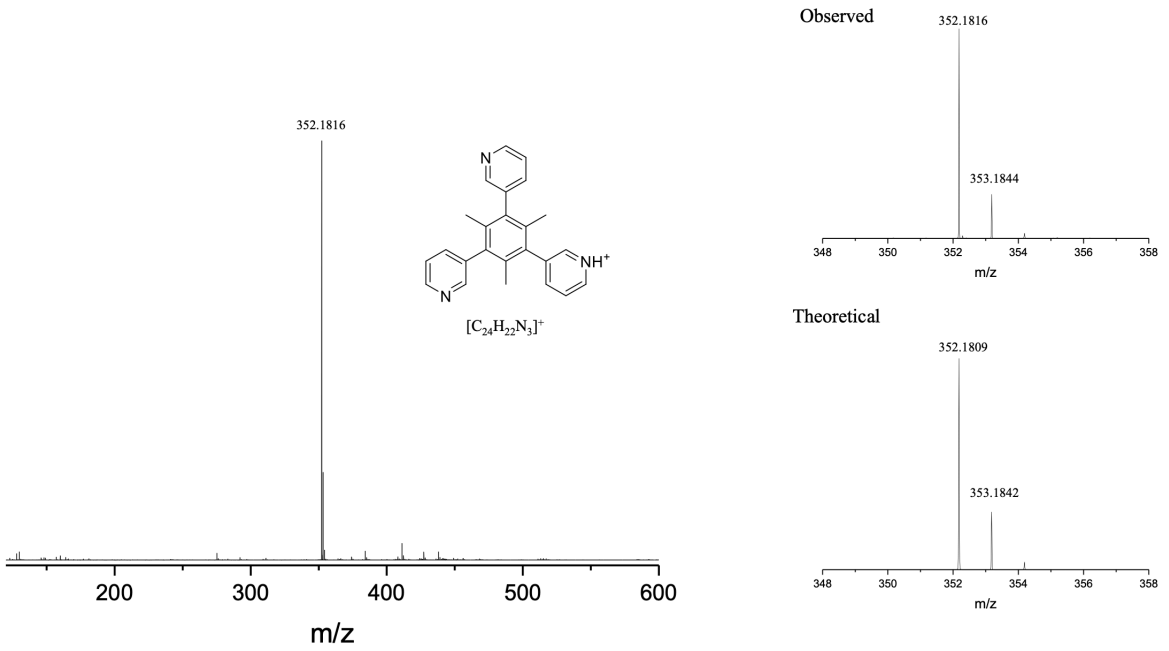

Fig. S3. HRMS (ESI) spectra of intermediate 8, showing m/z values representing $[8+H^+]^+$.

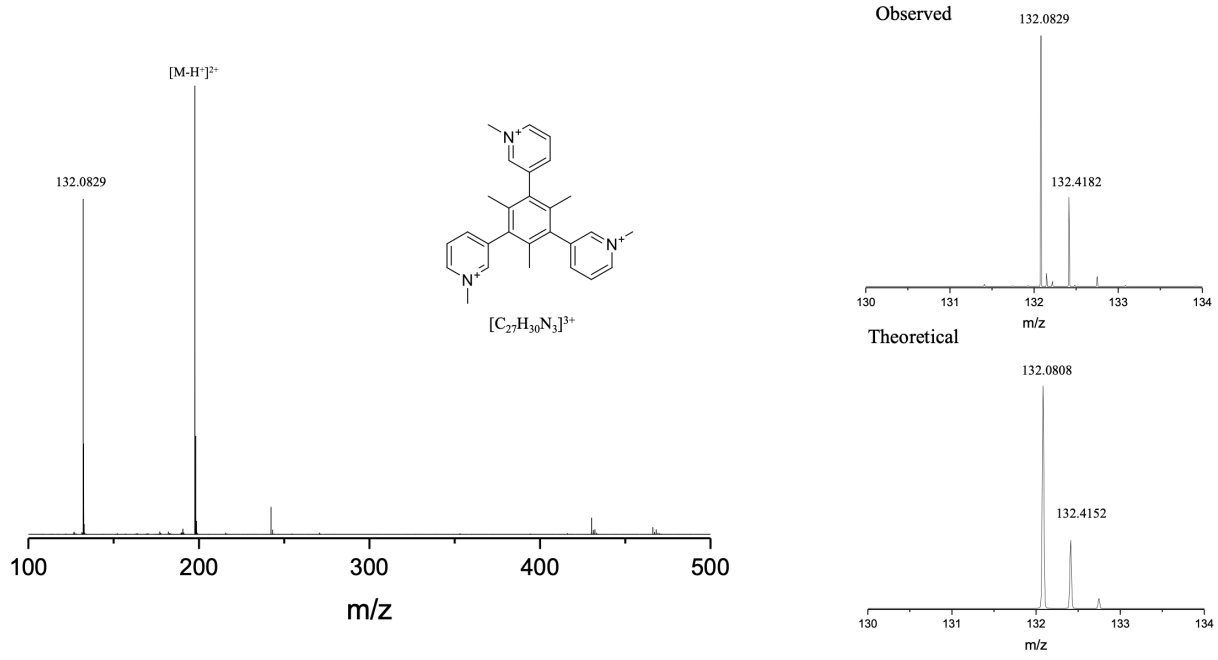

Fig. S4. HRMS (ESI) spectra of TPy^{3+}, showing m/z values representing TPy^{3+}.

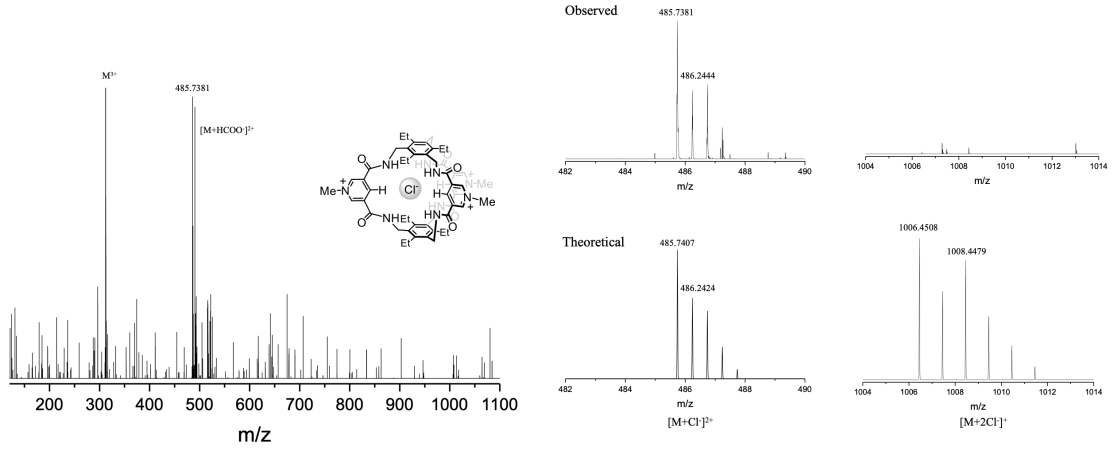

Fig. S5. HRMS (ESI) spectra of a mixture of NaCl and $TPPC^{3+}$•$3Cl^{-}$ showing m/z values representing $Cl^{-}\subset TPPC^{3+}$. No peak representing $[2Cl^{-}\subset TPPC^{3+}]^{+}$ at 1006.4508 was observed.

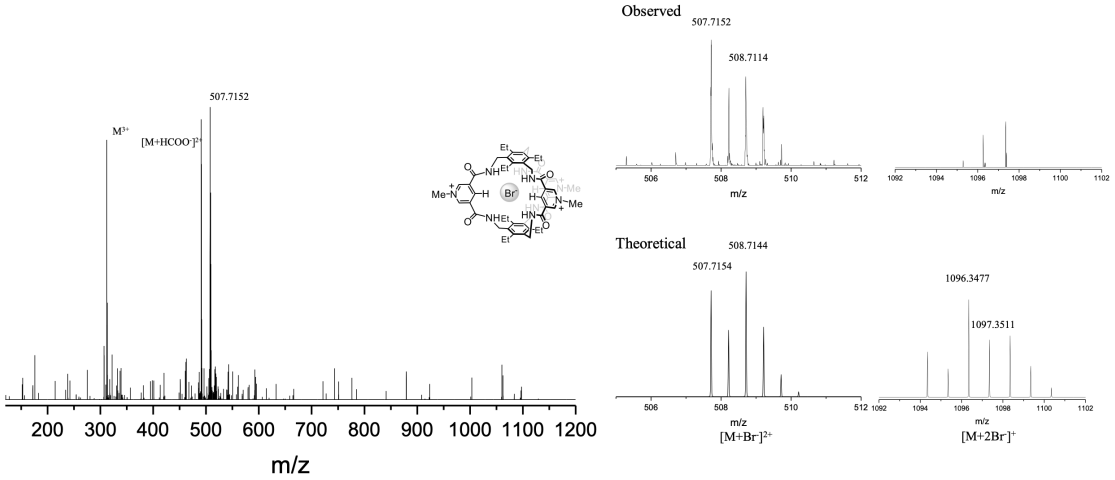

Fig. S6. HRMS (ESI) spectra of a mixture of NaBr and $TPPC^{3+}$•$3Cl^{-}$ showing m/z values representing $Br^{-}\subset TPPC^{3+}$. No peak representing $[2Br^{-}\subset TPPC^{3+}]^{+}$ at 1096.3477 was observed.

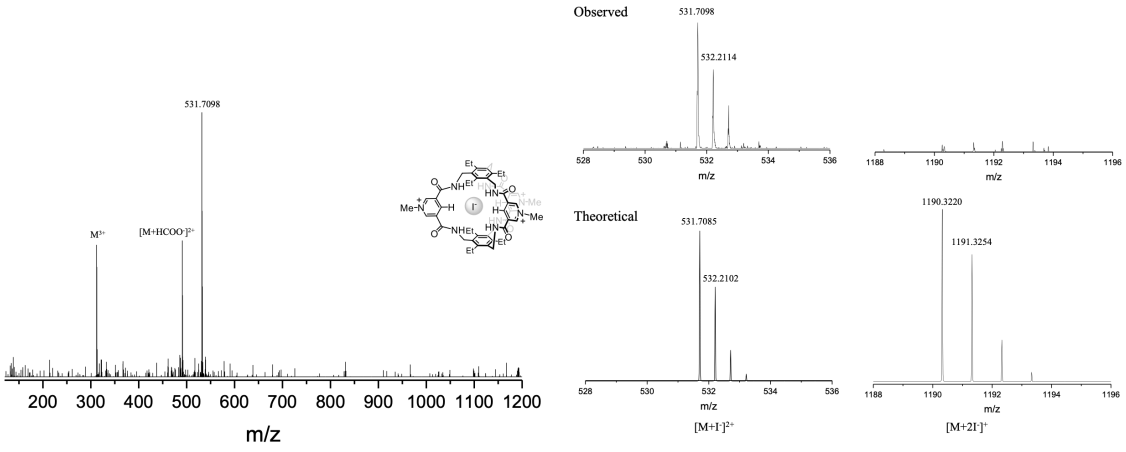

Fig. S7. HRMS (ESI) spectra of a mixture of NaI and $TPPC^{3+}$•$3Cl^{-}$ showing m/z values representing $I^{-}\subset TPPC^{3+}$. No peak representing $[2I^{-}\subset TPPC^{3+}]^{+}$ at 1190.3220 was observed.

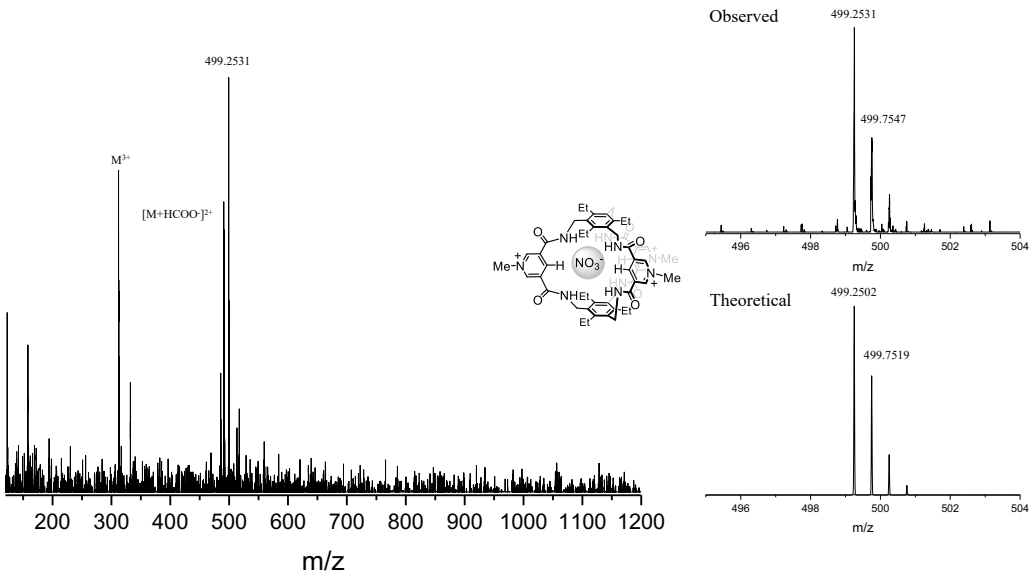

Fig. S8. HRMS (ESI) spectra of a mixture of $NaNO_3$ and $TPPC^{3+}$•$3Cl^-$ showing m/z values representing NO_3^-⊂$TPPC^{3+}$.

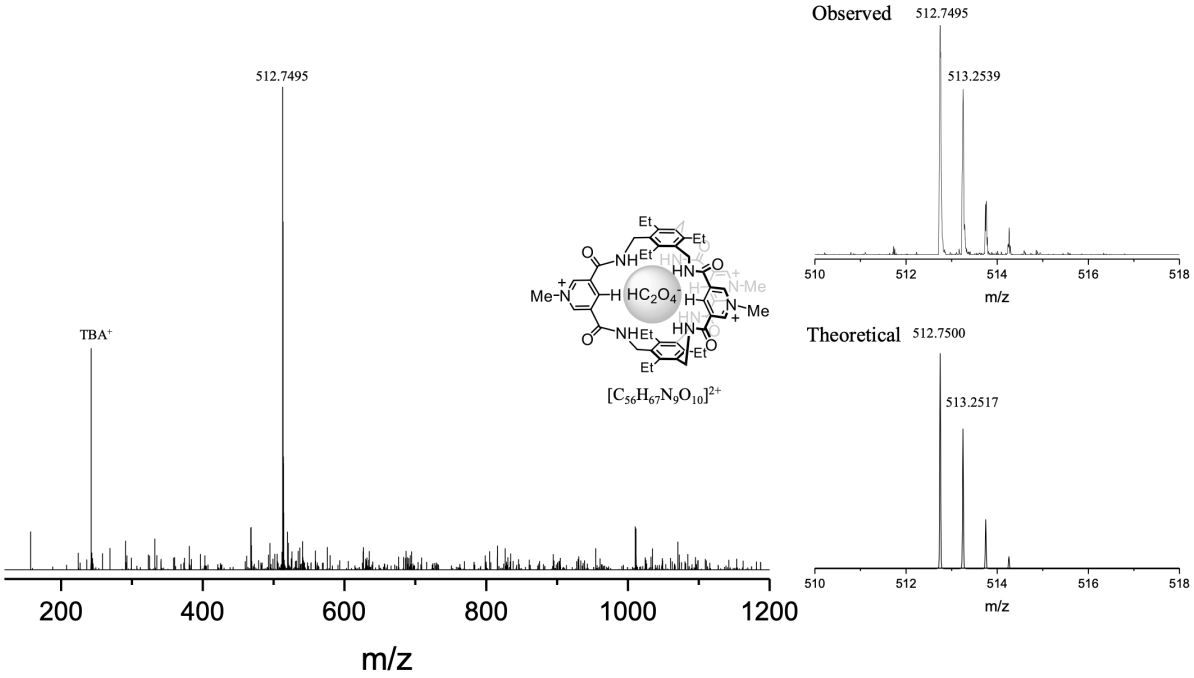

Fig. S9. HRMS (ESI) spectra of a mixture of $Na_2C_2O_4$ and $TPPC^{3+}$•$3Cl^-$ showing m/z values representing $HC_2O_4^-$⊂$TPPC^{3+}$. Note: the $C_2O_4^{2-}$ is protonated as $HC_2O_4^-$ since the solvent used for HRMS contains formic acid.

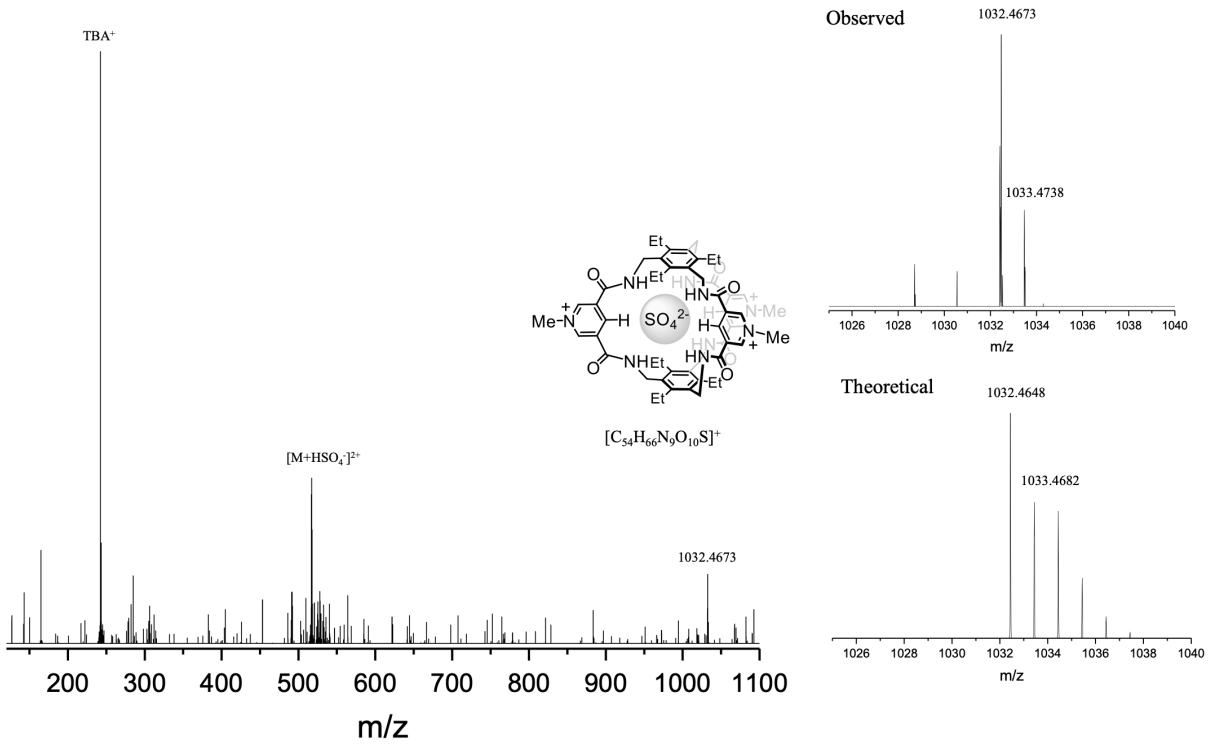

Fig. S10. HRMS (ESI) spectra of a mixture of Na_2SO_4 and $TPPC^{3+}\bullet 3Cl^-$ showing m/z values representing $SO_4^{2-}\subset TPPC^{3+}$

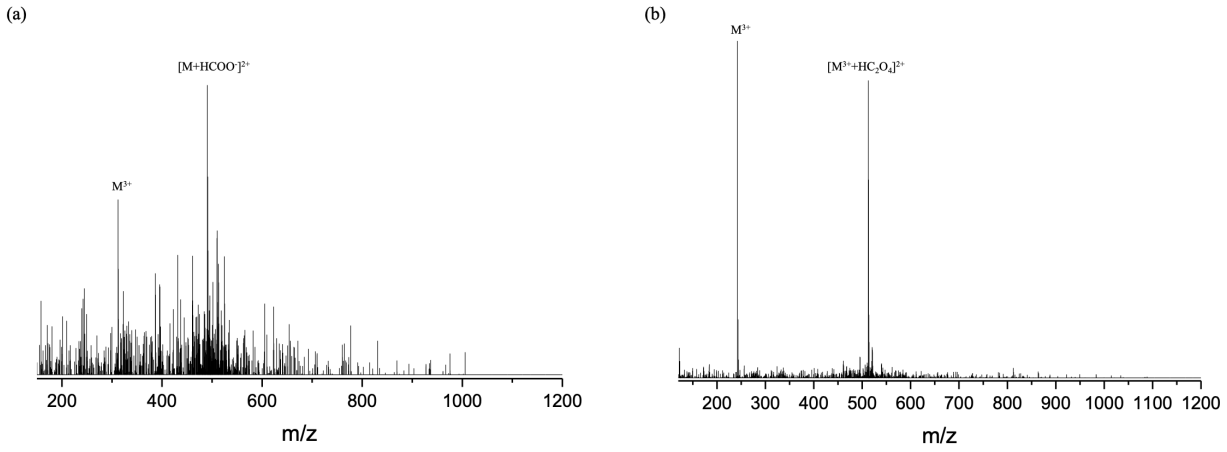

Fig. S11. HRMS (ESI) spectra of (a) a 1:1 mixture of $TPPC^{3+}\bullet 3Cl^-$ and $KMnO_4$ (b) a 1:1:1 mixture $TPPC^{3+}\bullet 3Cl^-$, $KMnO_4$, and $H_2C_2O_4$.

4. NMR Spectroscopy

Compound Characterization

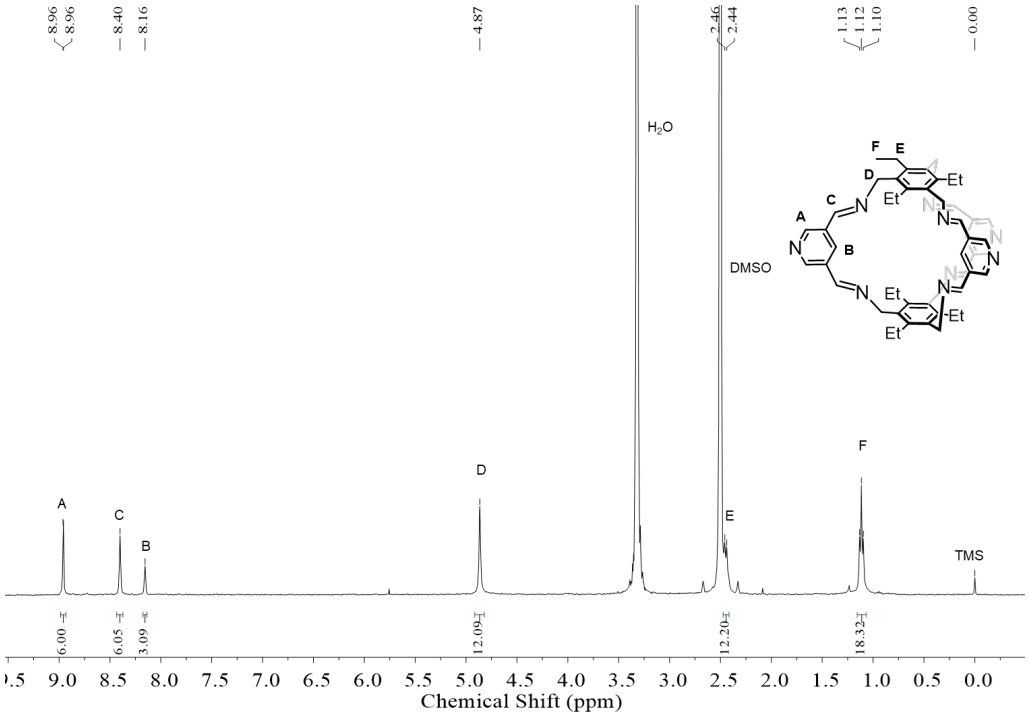

Fig. S12. ^{1}H NMR (400 MHz, DMSO-d6) spectrum of the imine cage 4.

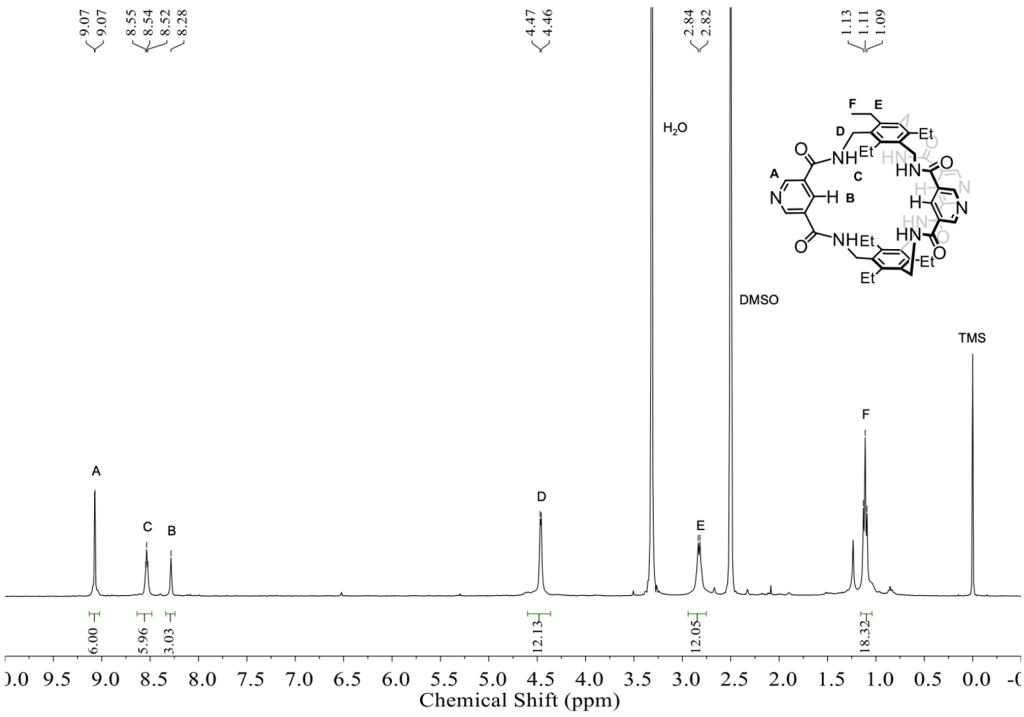

Fig. S13. ^{1}H NMR (400 MHz, DMSO-d6) spectrum of the amide cage 5.

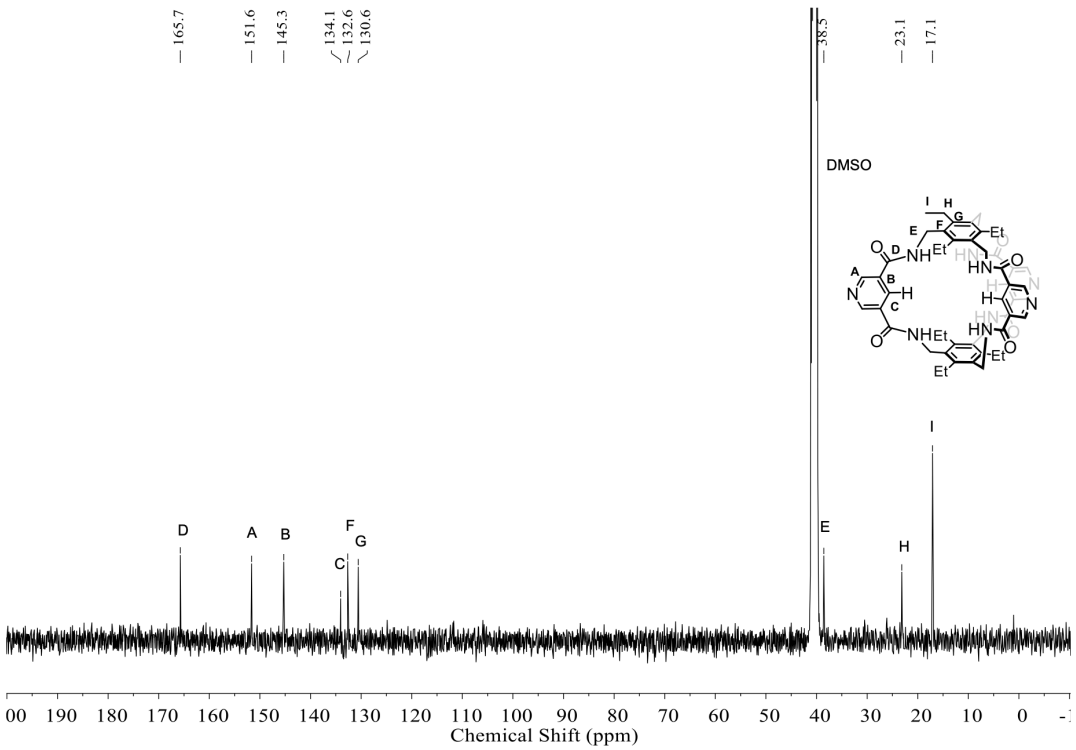

Fig. S14. ^{13}C NMR (101 MHz, DMSO-d6) spectrum of the amide cage 5.

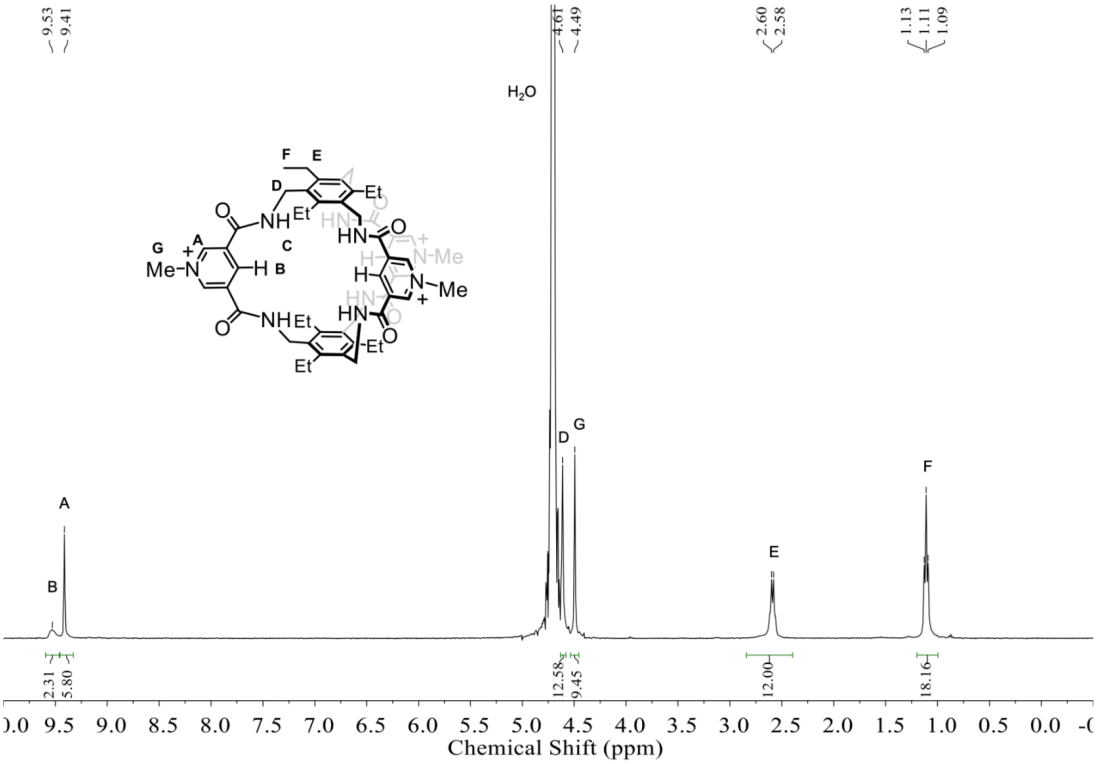

Fig. S15. ^{1}H NMR (400 MHz, D_2O) spectrum of $TPPC^{3+}\bullet 3Cl^{-}$.

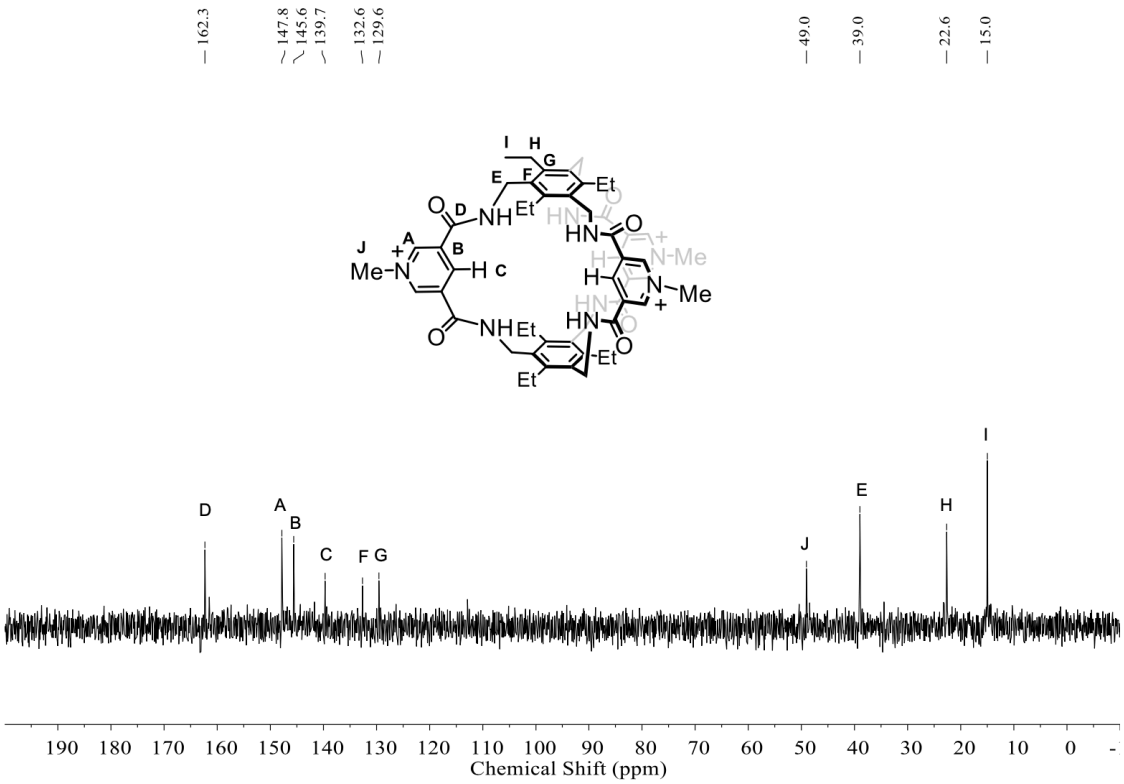

Fig. S16. ^{13}C NMR (101 MHz, D_2O) spectrum of $TPPC^{3+}\bullet 3Cl^-$.

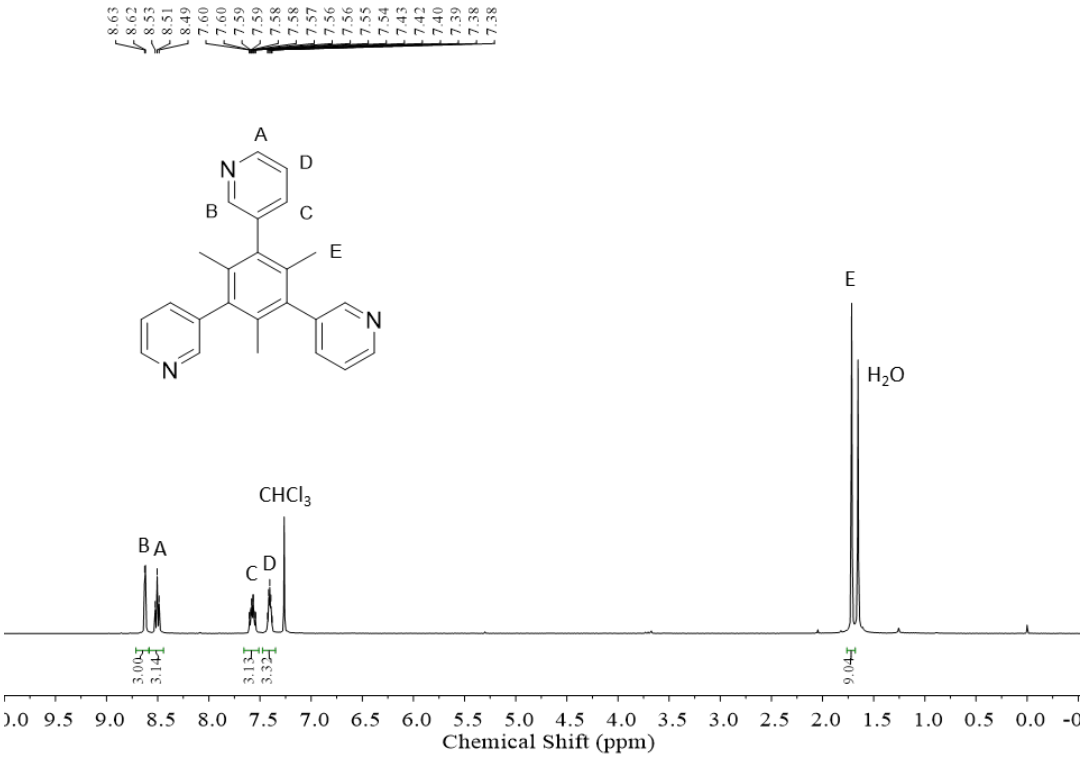

Fig. S17. ^1H NMR (400 MHz, $CDCl_3$) spectrum of intermediate 8.

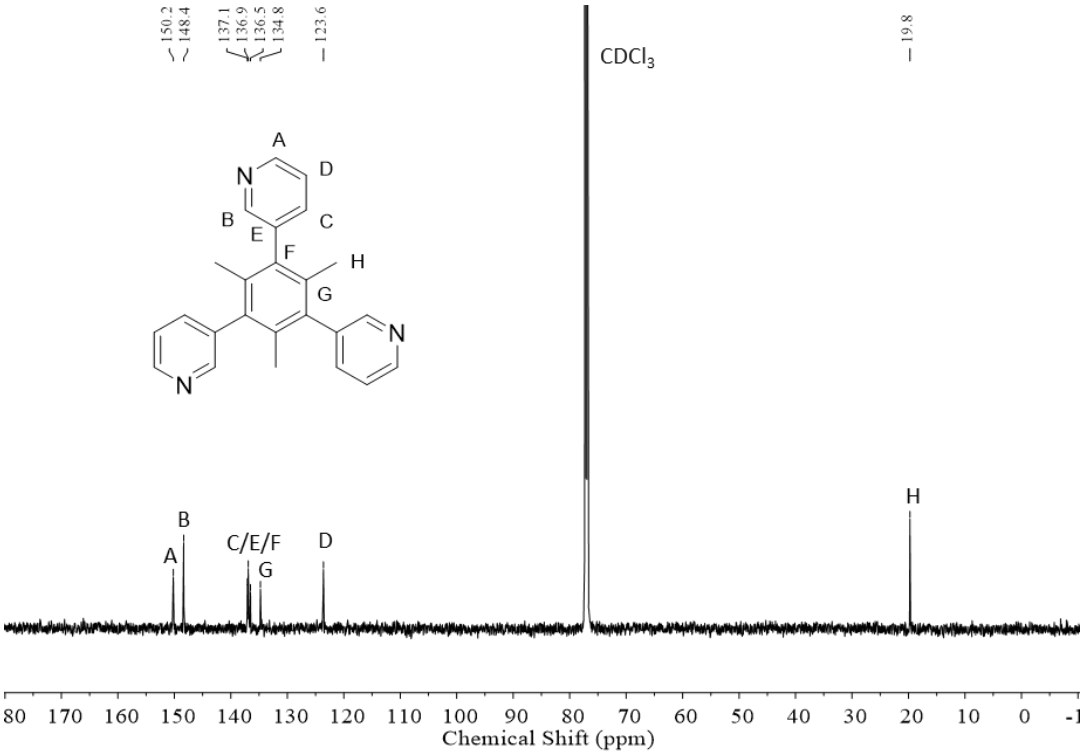

Fig. S18. ^{13}C NMR (101 MHz, $CDCl_3$) spectrum of intermediate 8.

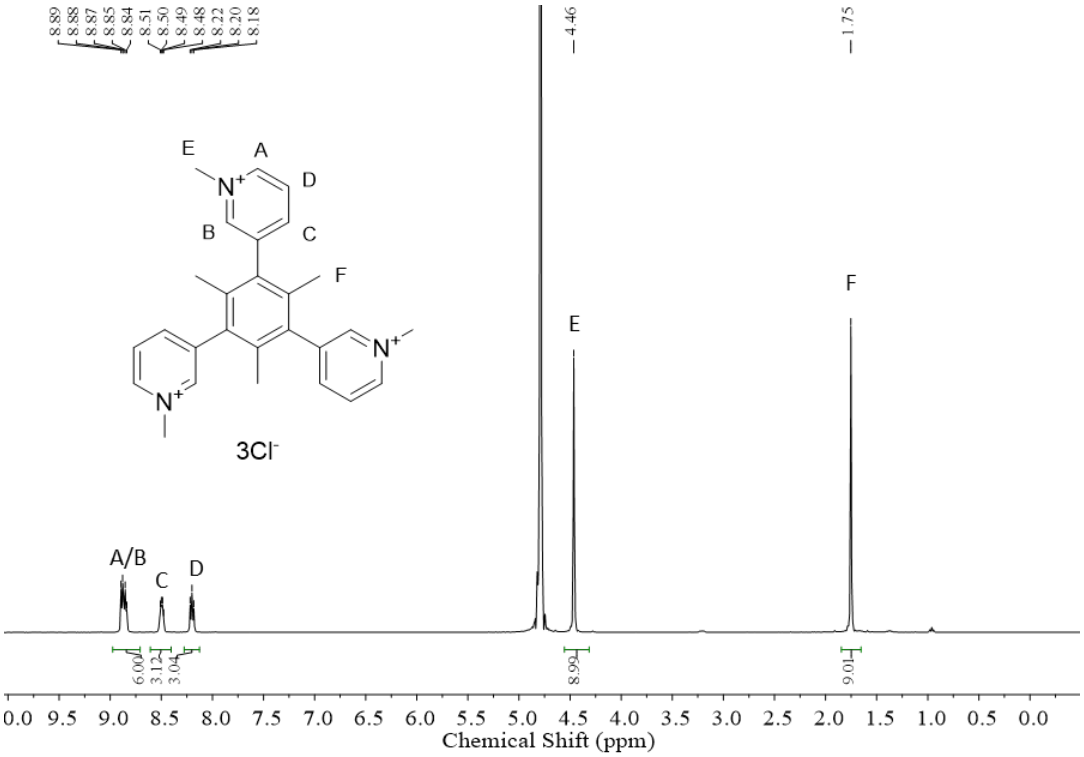

Fig. S19. ^{1}H NMR (400 MHz, D_2O) spectrum of $TPy^{3+}•3Cl^{-}$.

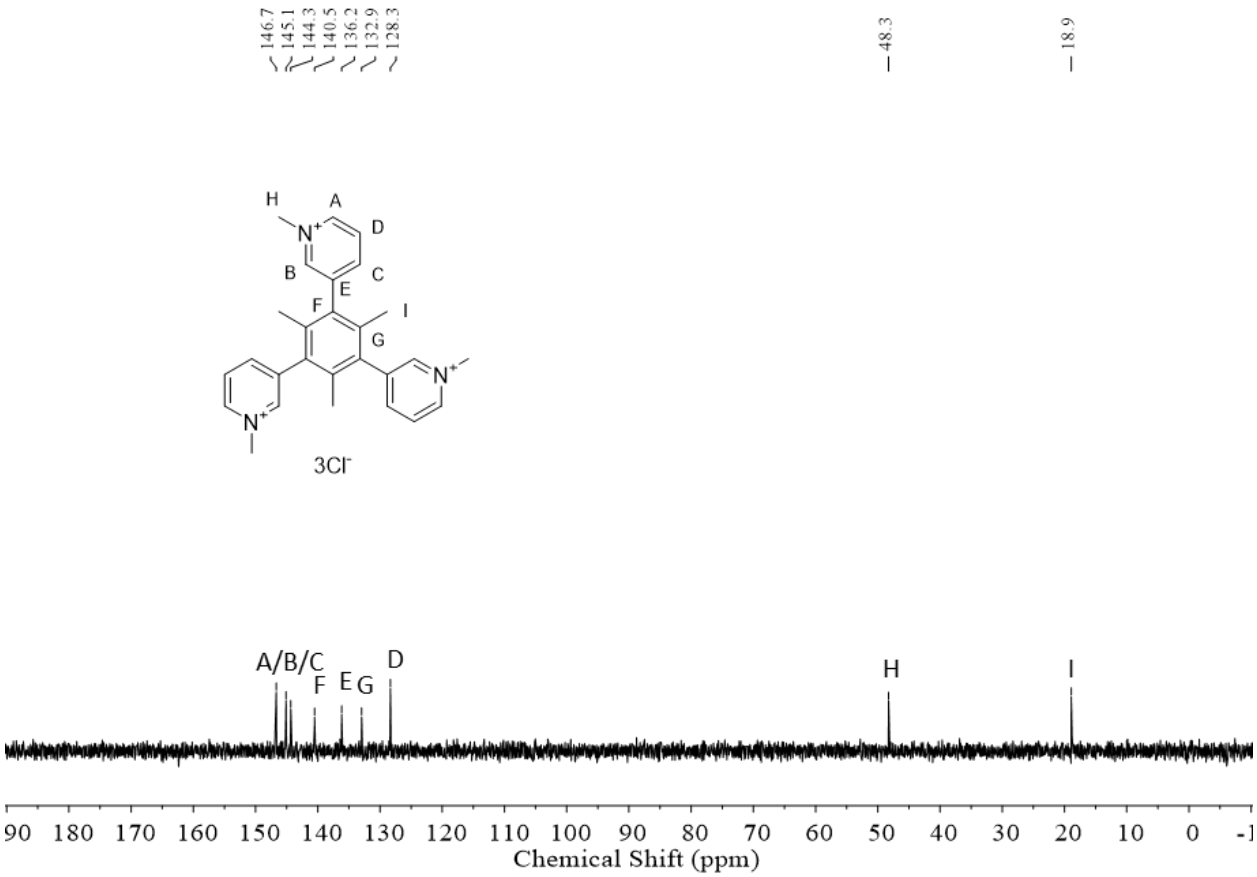

Fig. S20. ^{13}C NMR (101 MHz, D_2O) spectrum of $TPy^{3+}•3Cl^-$.

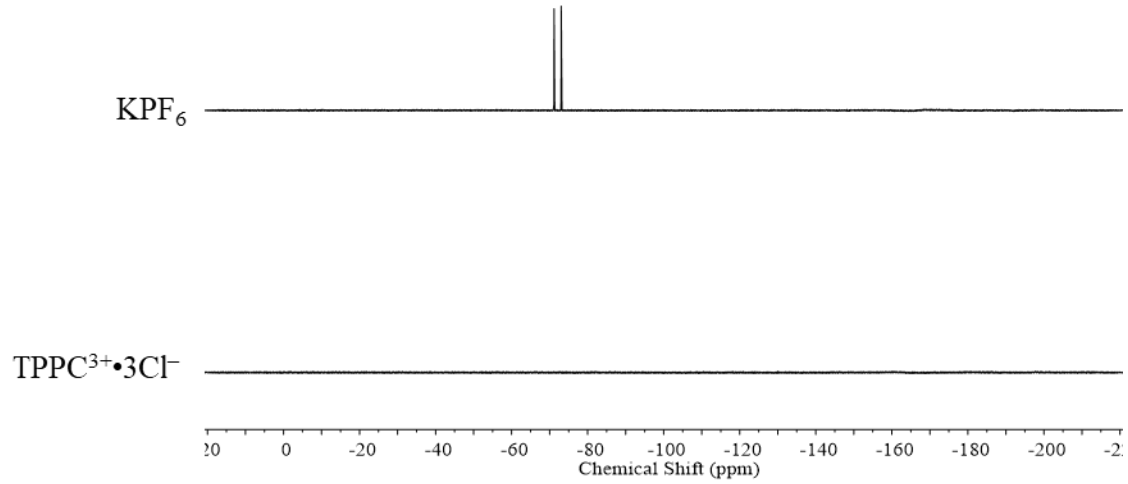

Fig. S21. ^{19}F NMR (376 MHz, D_2O) spectrum of KPF_6 (top) and $TPPC^{3+}•3Cl^-$ (bottom), suggesting the absence of PF_6^- in the sample of $TPPC^{3+}•3Cl^-$.

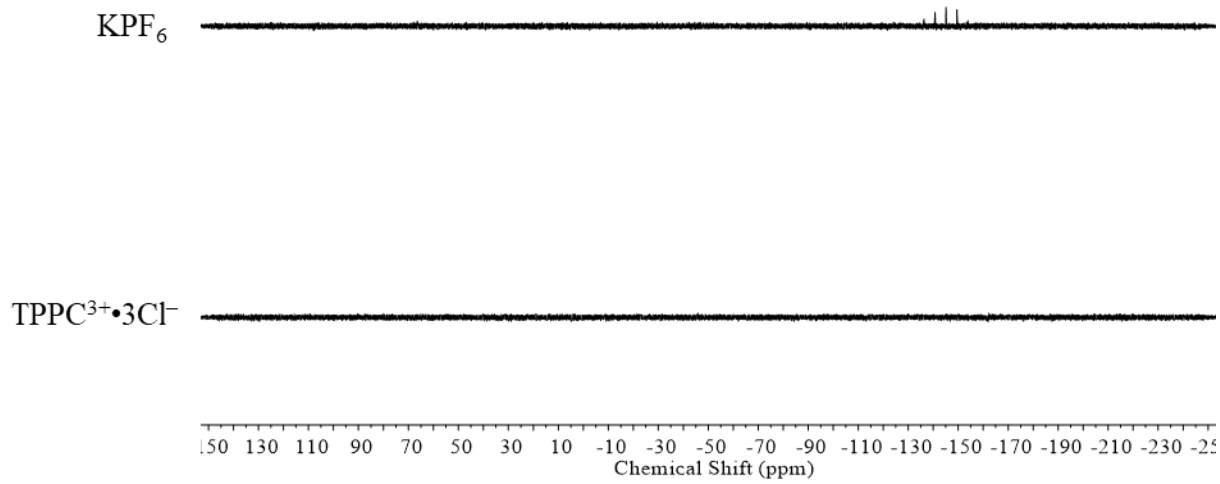

Fig. S22. ^{31}P NMR (162 MHz, D_2O) spectrum of KPF_6 (top) and $TPPC^{3+}$•$3Cl^-$ (bottom), suggesting the absence of PF_6^- in the sample of $TPPC^{3+}$•$3Cl^-$.

Anion Binding Analysis by ^{1}H NMR Titration.

^{1}H NMR titrations in D_2O were conducted at 298 K on a Varian Unity Inova 400 MHz system equipped with a cryoprobe. Aliquots from a stock solution containing the corresponding sodium salts (10–100 mM) were added sequentially to an NMR tube containing a solution of the $TPPC^{3+}$•$3Cl^-$ (600 μL). The ^{1}H NMR spectrum was acquired after each addition. Under these conditions, the added solution volume constitutes less than 10% of the host solution volume during titration. Consequently, changes in concentration have a minimal impact on the chemical shift of the receptor. The ^{1}H NMR titration spectra were analyzed by MestReNova software. The NMR titration isotherms were fitted[S1,S2] to a 1:1 host-guest binding model using Thordarson's equations at http://app.supramolecular.org/bindfit/. The data were then plotted using OriginLab software. The binding constants, K_a, were presented with standard deviations from the fitting outcomes.

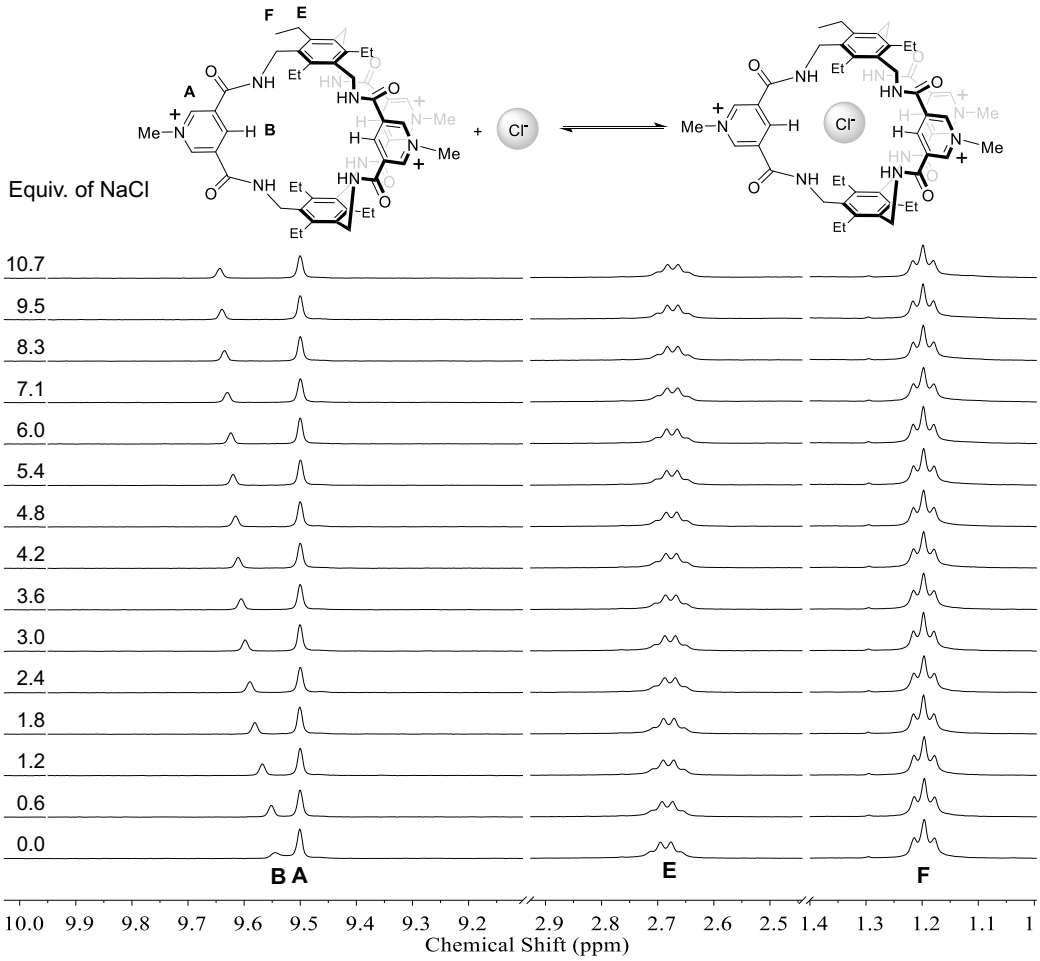

Fig. S23. ^{1}H NMR spectra (400 MHz, D_2O, 298 K) of $TPPC^{3+}$•$3Cl^{-}$ (0.42 mM) titrated with NaCl.

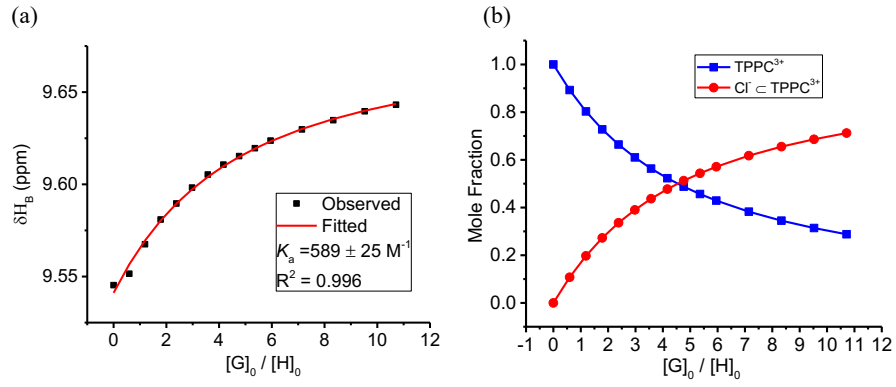

Fig. S24. (a) Titration isotherm created by monitoring changes in the chemical shift of proton B for $TPPC^{3+}$•$3Cl^{-}$ (0.42 mM) caused by the addition of NaCl in D_2O at 298 K. Red lines are the curve fitting using a 1:1 host-guest binding model. (b) Calculated changes of mole fractions for $TPPC^{3+}$ (blue trace) and $Cl^{-}\subset TPPC^{3+}$ (red trace) over the guest-host molar ratio.

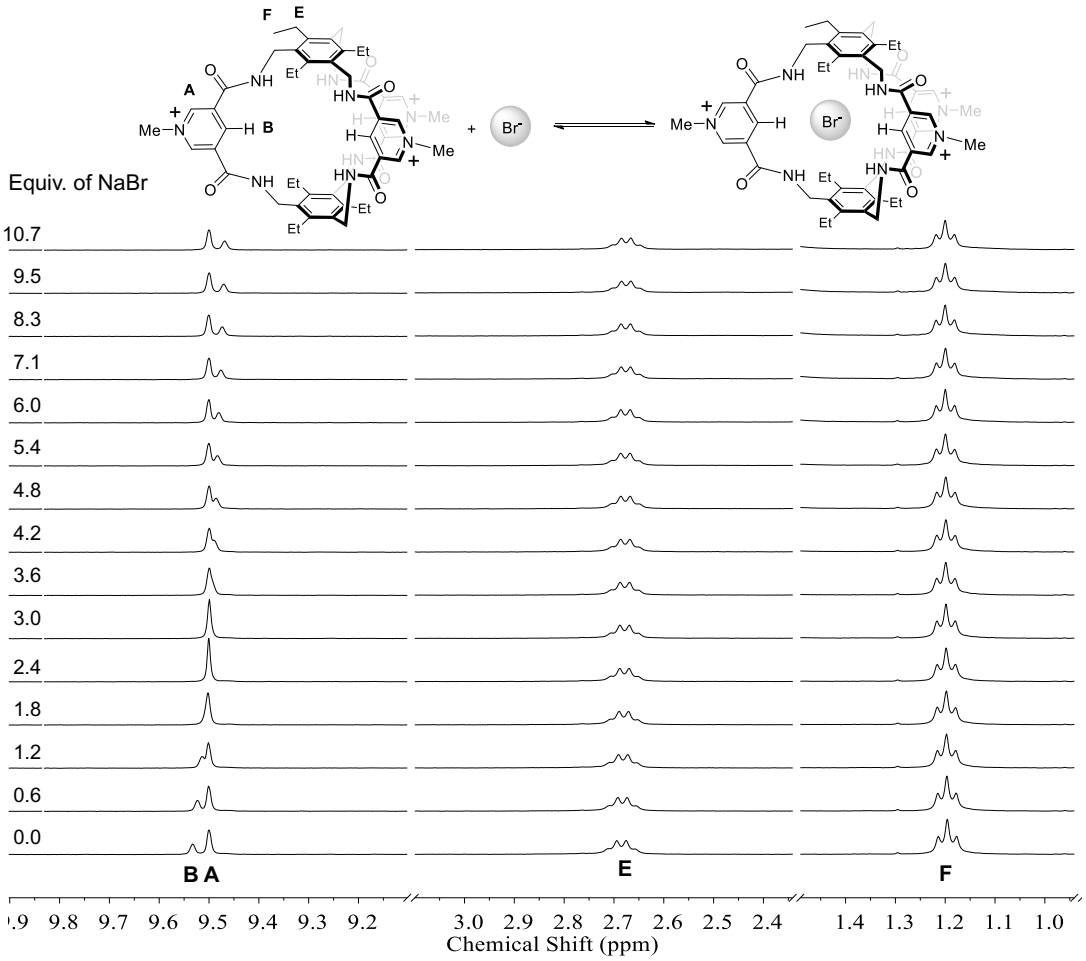

Fig. S25. ^{1}H NMR spectra (400 MHz, D_2O, 298 K) of $TPPC^{3+}$•$3Cl^-$ (0.42 mM) titrated with NaBr.

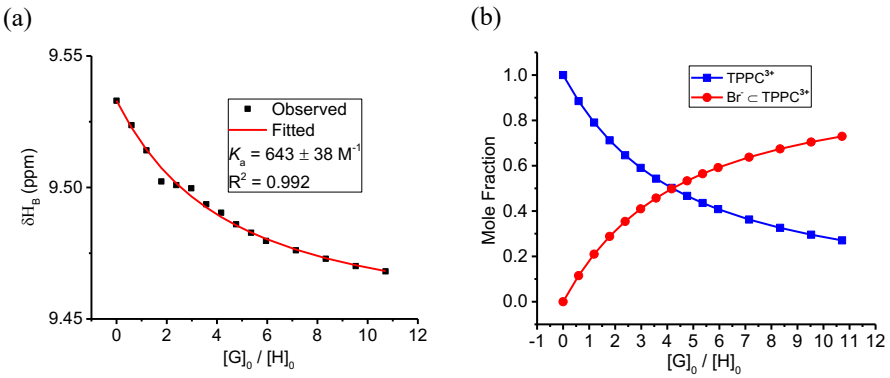

Fig. S26. (a) Titration isotherm created by monitoring changes in the chemical shift of proton B for $TPPC^{3+}$•$3Cl^-$ (0.42 mM) caused by the addition of NaBr in D_2O at 298 K. Red lines are the curve fitting using a 1:1 host-guest binding model. (b) Calculated changes of mole fractions for $TPPC^{3+}$ (blue trace) and $Br^-\subset TPPC^{3+}$ (red trace) over the guest-host molar ratio.

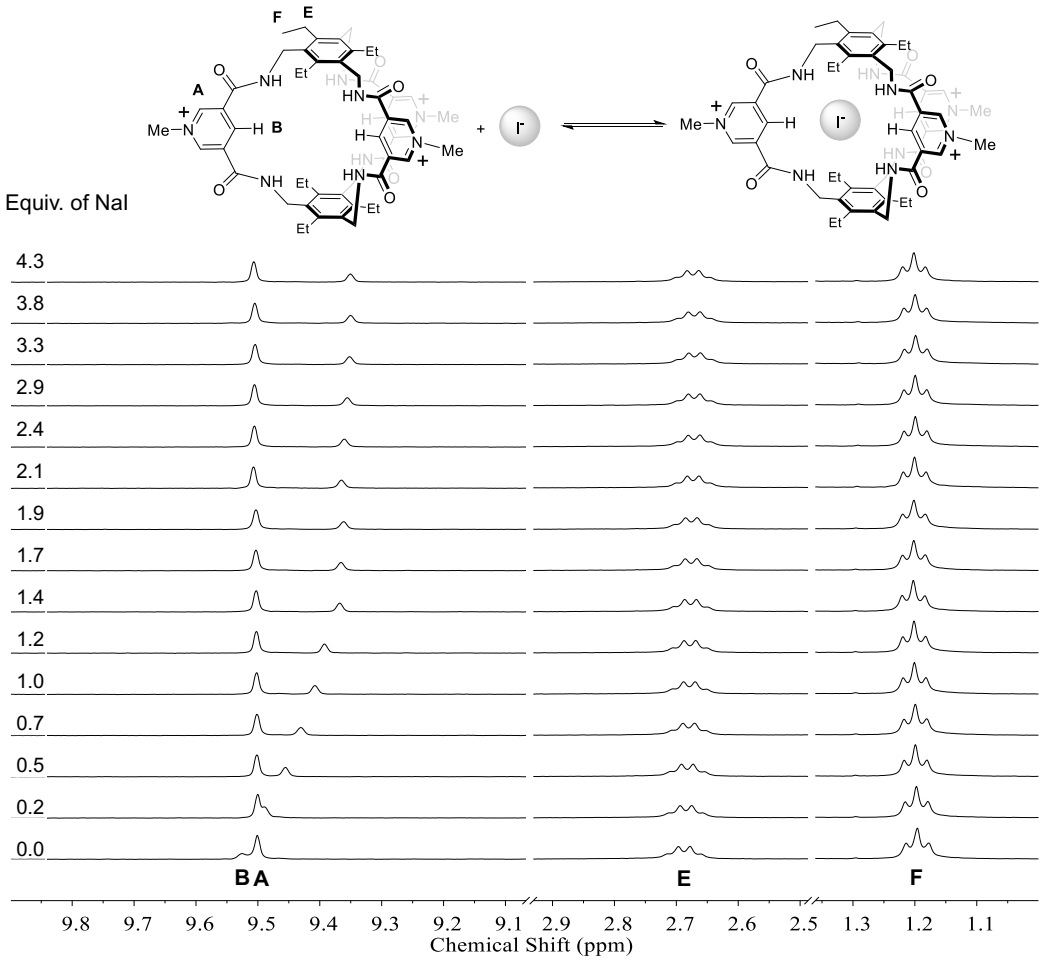

Fig. S27. ^{1}H NMR spectra (400 MHz, D_2O, 298 K) of $TPPC^{3+}$•3Cl^{-} (0.42 mM) titrated with NaI.

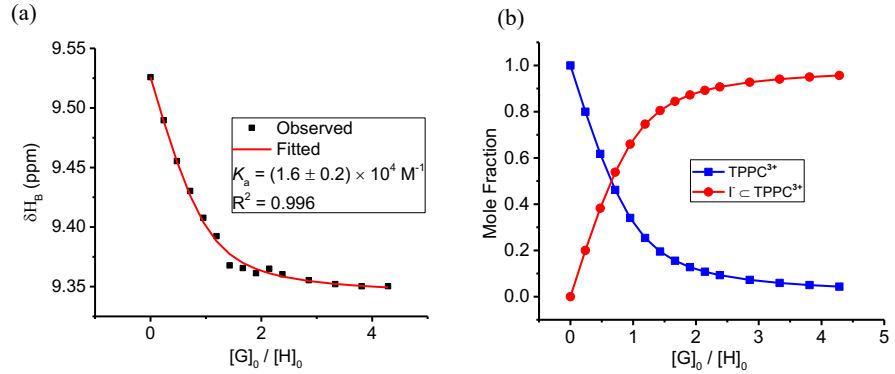

Fig. S28. (a) Titration isotherm created by monitoring changes in the chemical shift of proton B for $TPPC^{3+}$•3Cl^{-} (0.42 mM) caused by the addition of NaI in D_2O at 298 K. Red lines are the curve fitting using a 1:1 host-guest binding model. (b) Calculated changes of mole fractions for $TPPC^{3+}$ (blue trace) and $I^{-}\subset TPPC^{3+}$ (red trace) over the guest-host molar ratio.

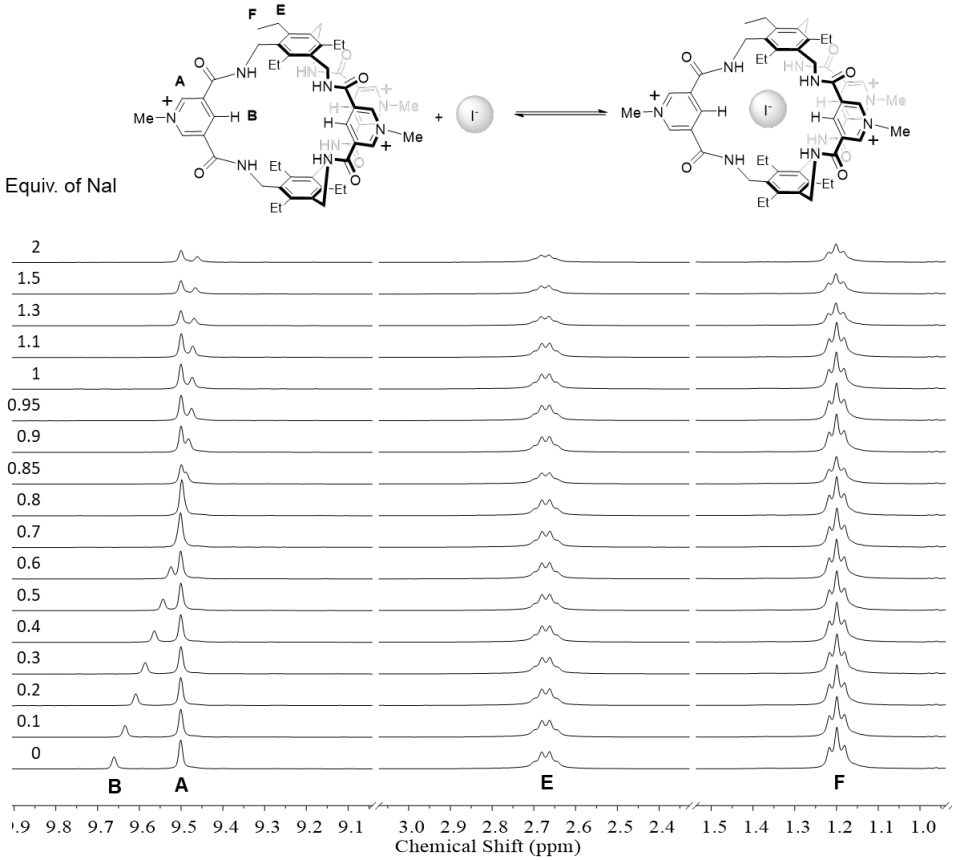

Fig. S29. ^{1}H NMR spectra (400 MHz, D_2O, 298 K) of $TPPC^{3+}$•$3Cl^-$ (3.0 mM) titrated with NaI.

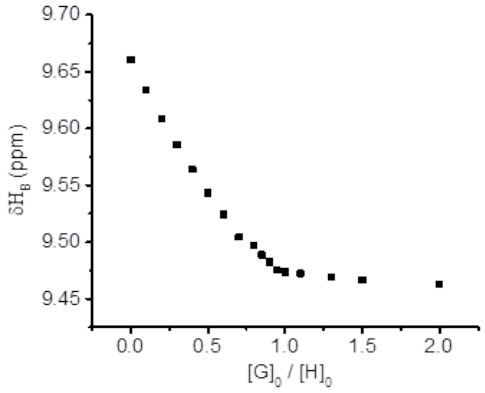

Fig. S30. Titration isotherm created by monitoring changes in the chemical shift of proton B for $TPPC^{3+}$•$3Cl^-$ (3.0 mM) caused by the addition of NaI in D_2O at 298 K. The shift of proton B stopped after adding 1 equivalent of I^-, indicating a 1:1 binding stoichiometry between $TPPC^{3+}$ and I^- in D_2O.

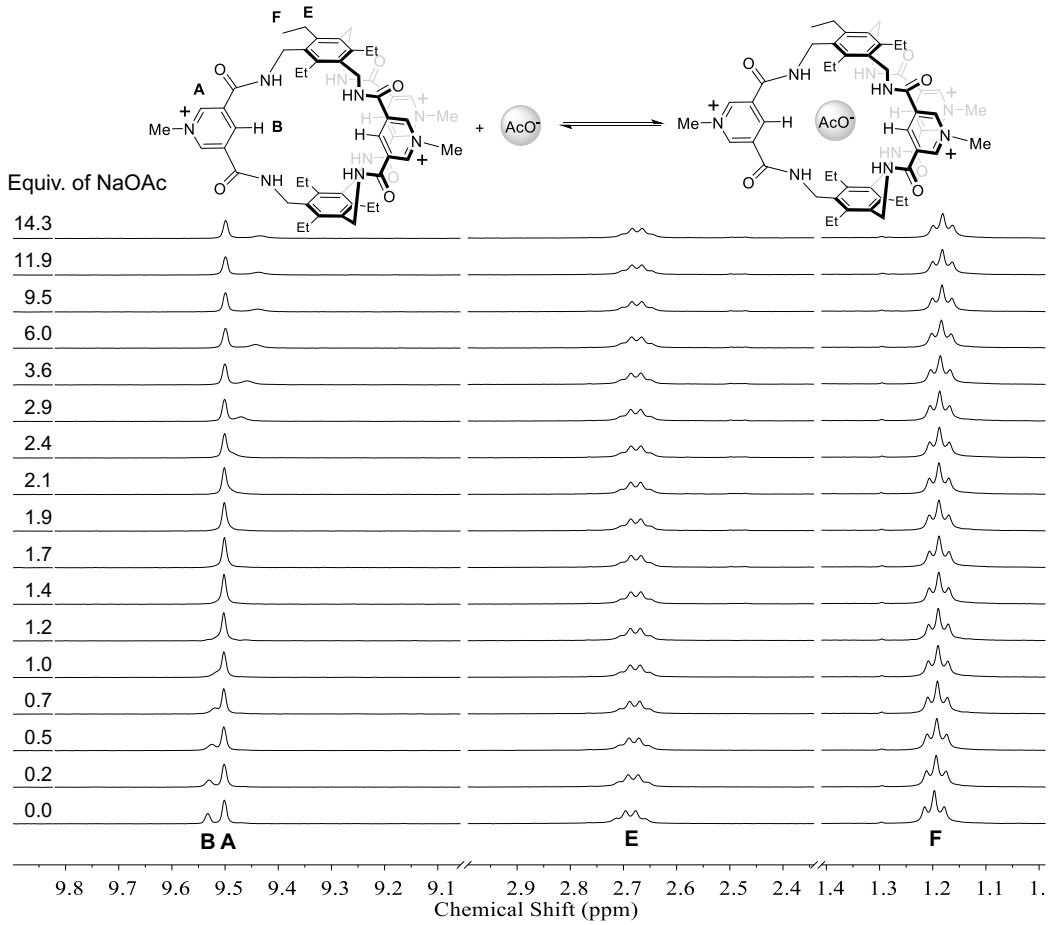

Fig. S31. ^{1}H NMR spectra (400 MHz, D_2O, 298 K) of $TPPC^{3+}$•$3Cl^-$ (0.42 mM) titrated with NaOAc.

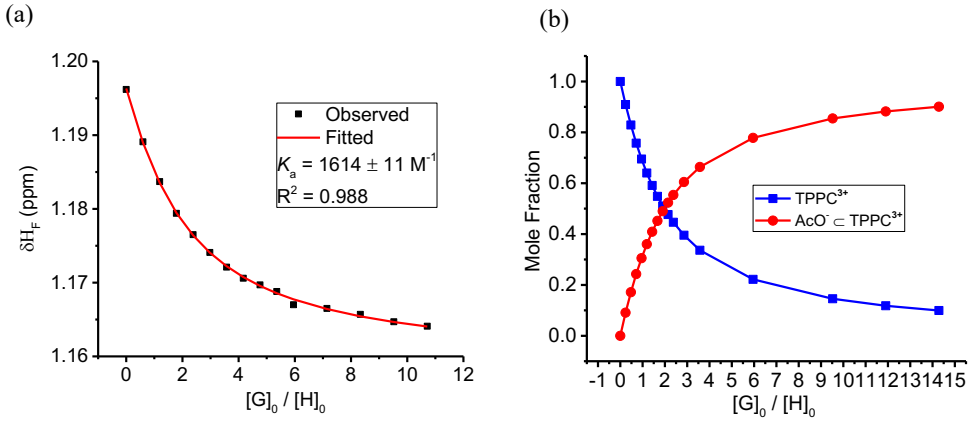

Fig. S32. (a) Titration isotherm created by monitoring changes in the chemical shift of proton F for $TPPC^{3+}$•$3Cl^-$ (0.42 mM) caused by the addition of NaOAc in D_2O at 298 K. Red lines are the curve fitting using a 1:1 host-guest binding model. (b) Calculated changes of mole fractions for $TPPC^{3+}$ (blue trace) and $AcO^-\subset TPPC^{3+}$ (red trace) over the guest-host molar ratio.

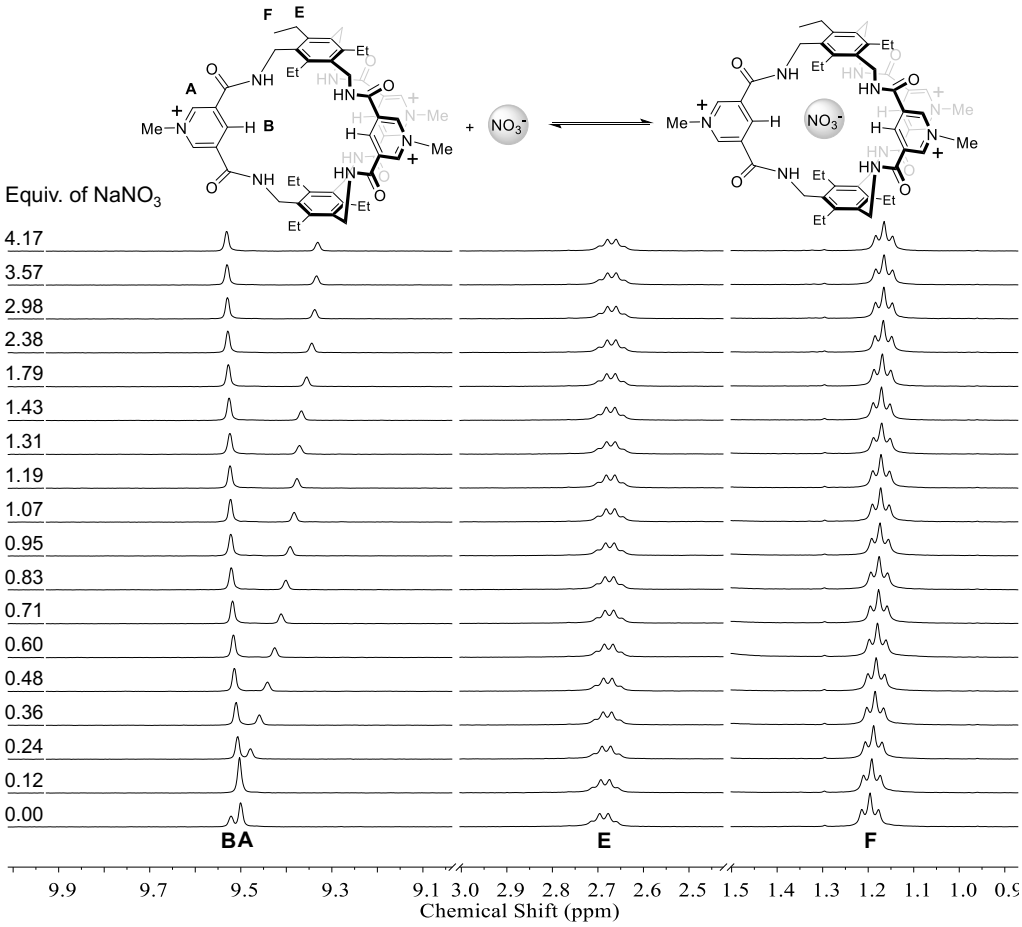

Fig. S33. ^{1}H NMR spectra (400 MHz, D_2O, 298 K) of $TPPC^{3+}$•$3Cl^-$ (0.42 mM) titrated with $NaNO_3$.

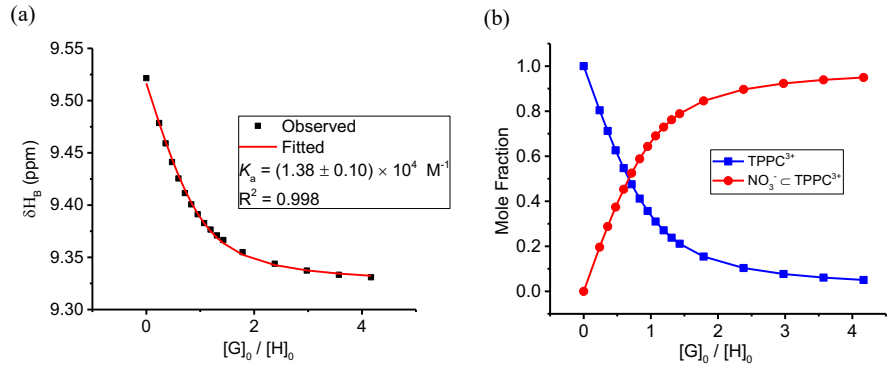

Fig. S34. (a) Titration isotherm created by monitoring changes in the chemical shift of proton B for $TPPC^{3+}$•$3Cl^-$ (0.42 mM) caused by the addition of $NaNO_3$ in D_2O at 298 K. Red lines are the curve fitting using a 1:1 host-guest binding model. (b) Calculated changes of mole fractions for $TPPC^{3+}$ (blue trace) and $NO_3^-\subset TPPC^{3+}$ (red trace) over the guest-host molar ratio.

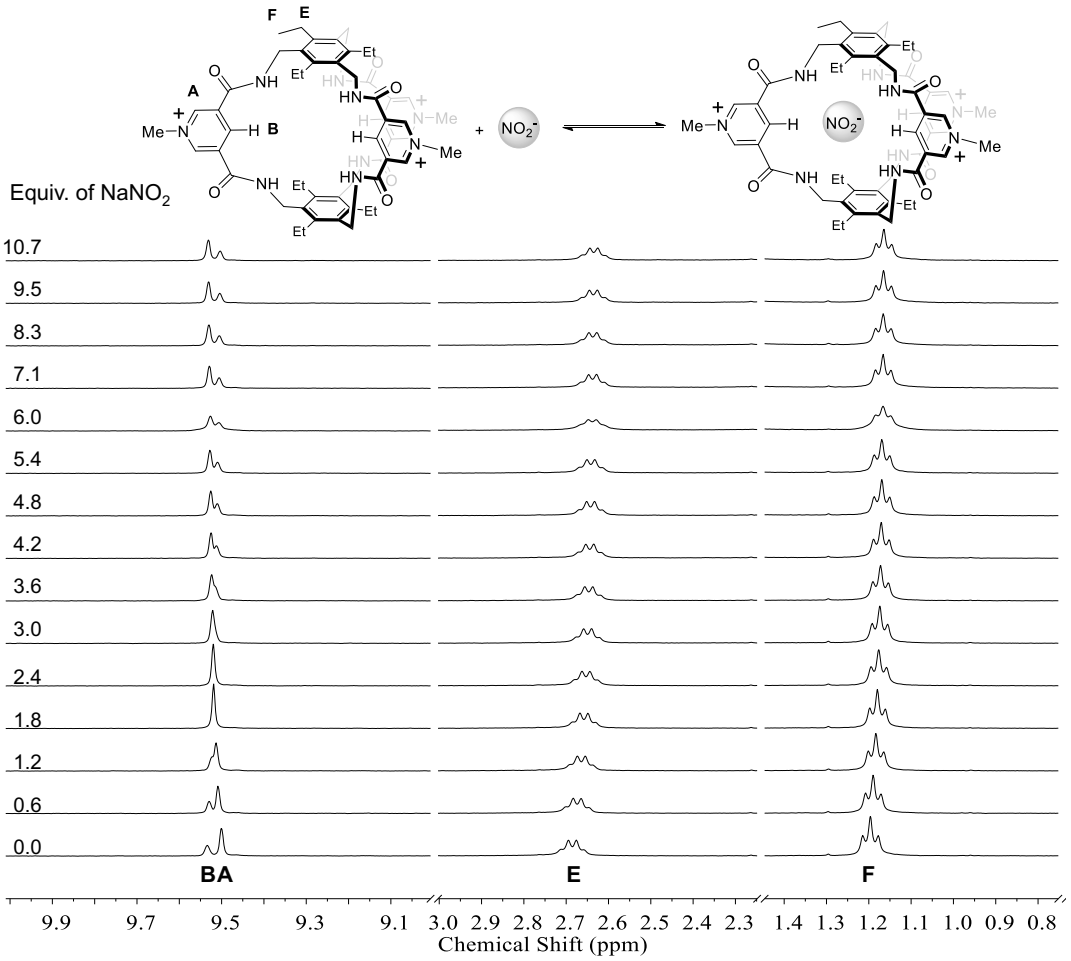

Fig. S35. ^{1}H NMR spectra (400 MHz, D_2O, 298 K) of $TPPC^{3+}$•$3Cl^-$ (0.42 mM) titrated with $NaNO_2$.

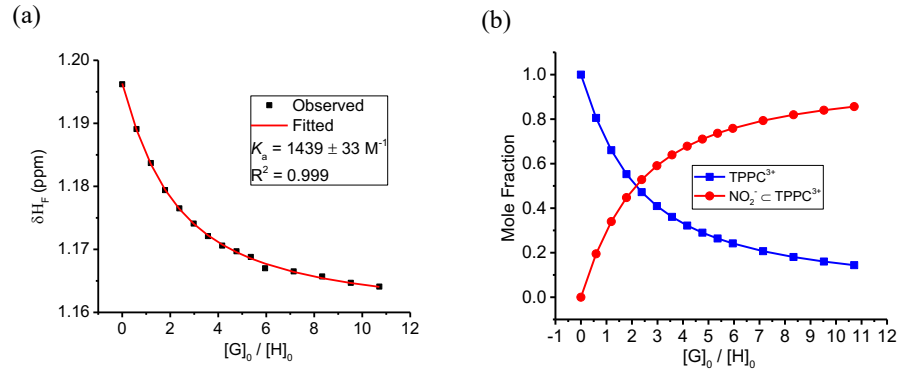

Fig. S36. (a) Titration isotherm created by monitoring changes in the chemical shift of proton F for $TPPC^{3+}$•$3Cl^-$ (0.42 mM) caused by the addition of $NaNO_2$ in D_2O at 298 K. Red lines are the curve fitting using a 1:1 host-guest binding model. (b) Calculated changes of mole fractions for $TPPC^{3+}$ (blue trace) and $NO_2^- \subset TPPC^{3+}$ (red trace) over the guest-host molar ratio.

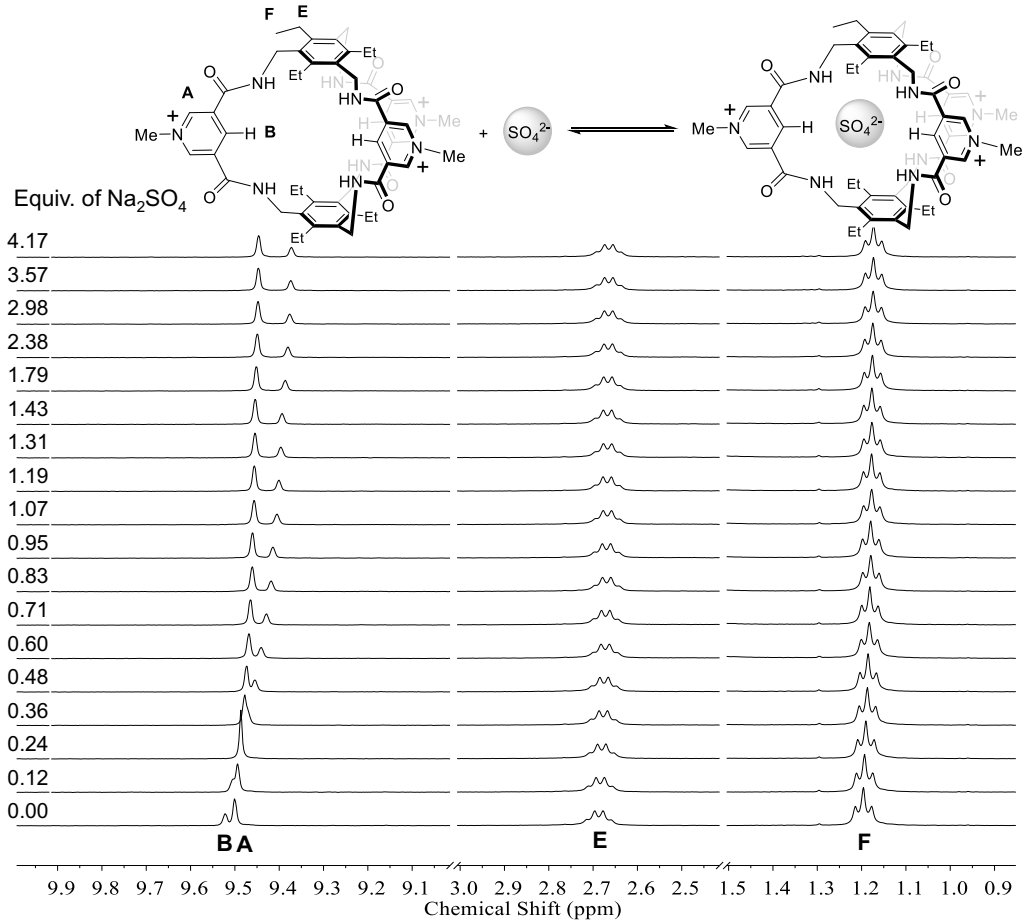

Fig. S37. ^{1}H NMR spectra (400 MHz, D_2O, 298 K) of $TPPC^{3+}$•$3Cl^{-}$ (0.42 mM) titrated with Na_2SO_4.

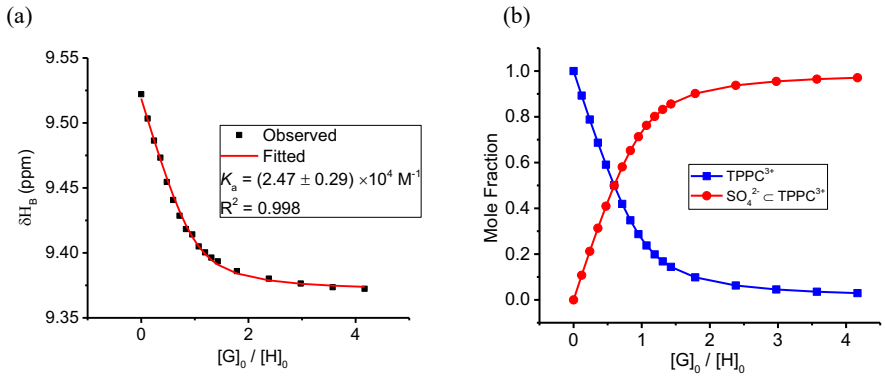

Fig. S38. (a) Titration isotherm created by monitoring changes in the chemical shift of proton B for $TPPC^{3+}$•$3Cl^{-}$ (0.42 mM) caused by the addition of Na_2SO_4 in D_2O at 298 K. Red lines are the curve fitting using a 1:1 host-guest binding model. (b) Calculated changes of mole fractions for $TPPC^{3+}$ (blue trace) and $SO_4^{2-}\subset TPPC^{3+}$ (red trace) over the guest-host molar ratio.

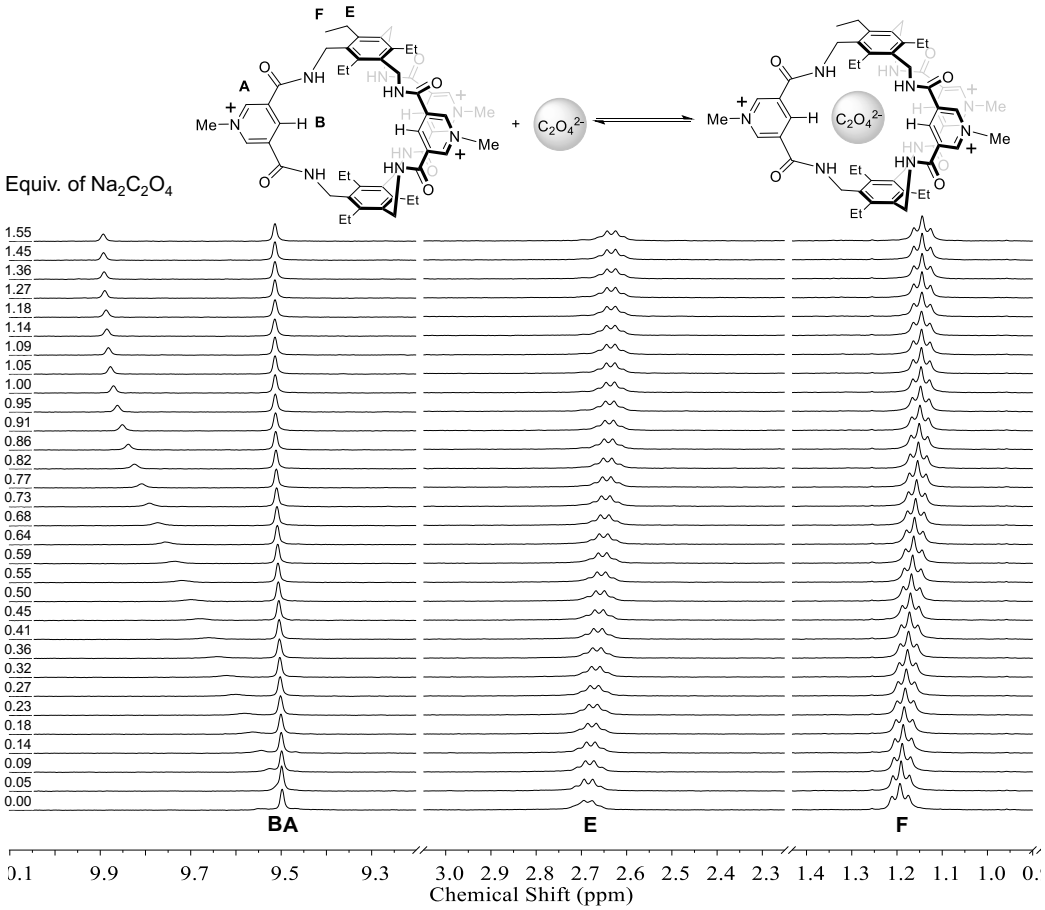

Fig. S39. ^{1}H NMR spectra (400 MHz, D_2O, 298 K) of $TPPC^{3+}$•$3Cl^-$ (0.11 mM) titrated with $Na_2C_2O_4$.

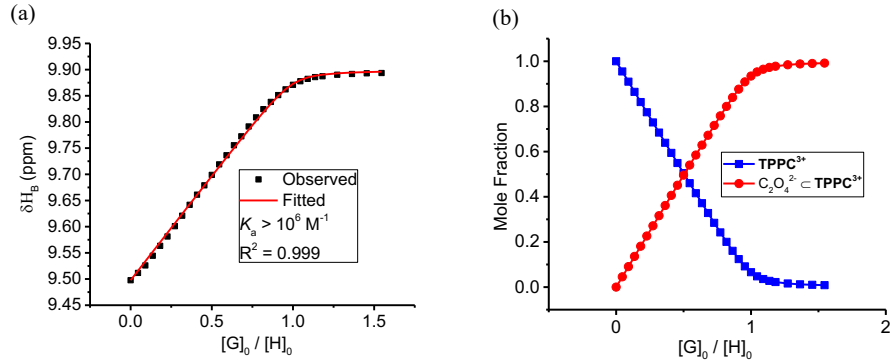

Fig. S40. (a) Titration isotherm created by monitoring changes in the chemical shift of proton B for $TPPC^{3+}$•$3Cl^-$ (0.11 mM) caused by the addition of $Na_2C_2O_4$ in D_2O at 298 K. Red lines are the curve fitting using a 1:1 host-guest binding model. (b) Calculated changes of mole fractions for $TPPC^{3+}$ (blue trace) and $C_2O_4^{2-} \subset TPPC^{3+}$ (red trace) over the guest-host molar ratio.

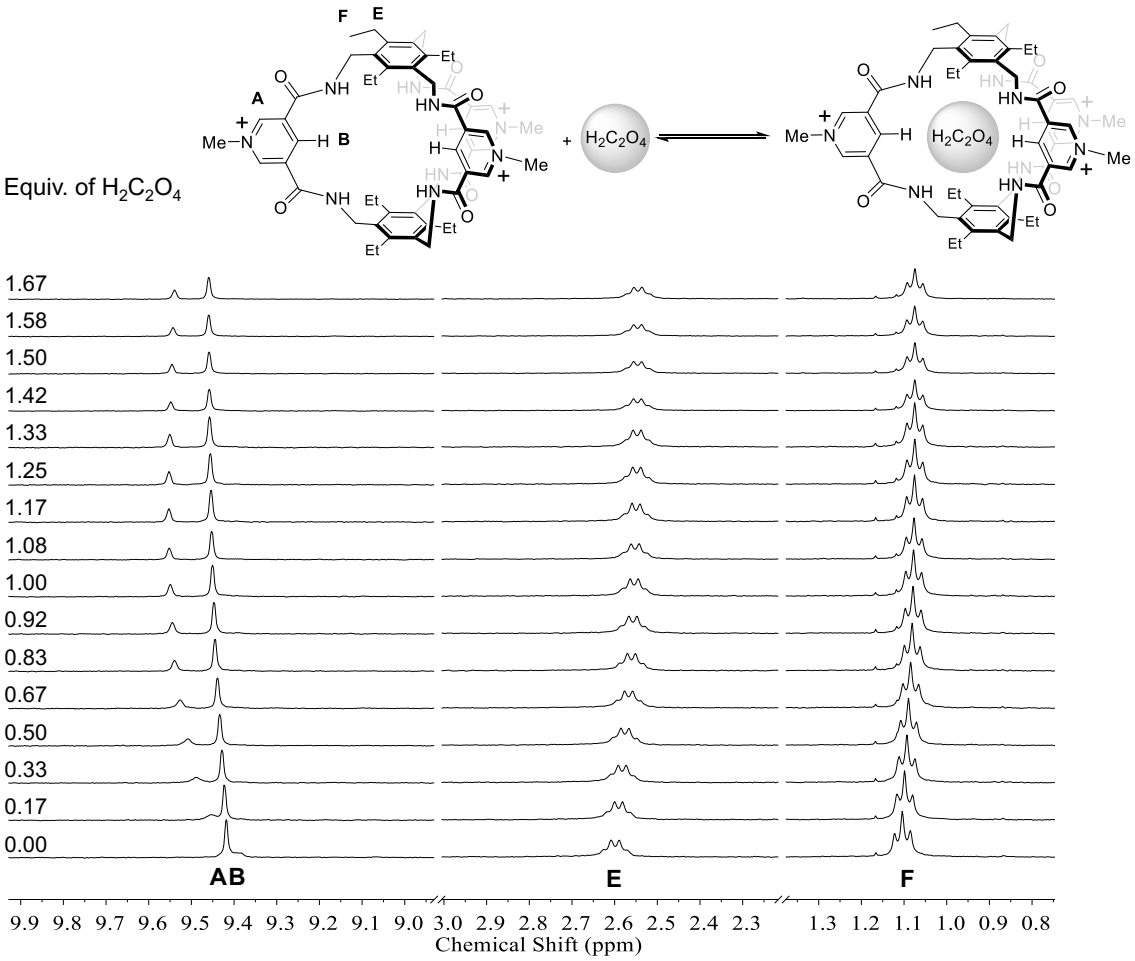

Fig. S41. ^{1}H NMR spectra (400 MHz, D_2O, 298 K) of $TPPC^{3+}$•$3Cl^-$ (0.19 mM) titrated with $H_2C_2O_4$.

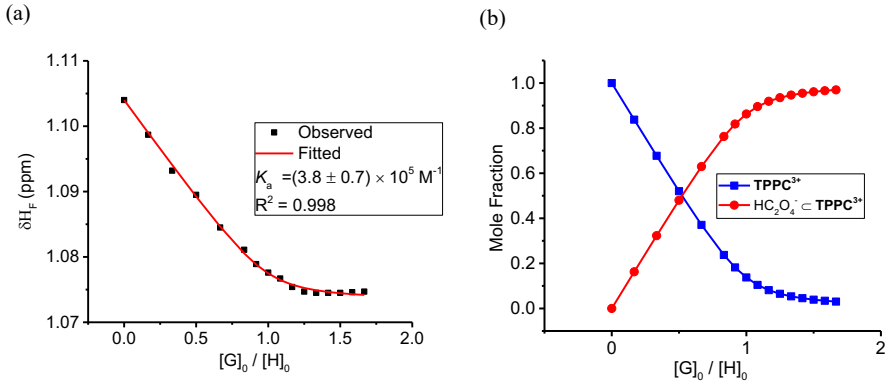

Fig. S42. (a) Titration isotherm created by monitoring changes in the chemical shift of proton F for $TPPC^{3+}$•$3Cl^-$ (0.12 mM) caused by the addition of $H_2C_2O_4$ in D_2O at 298 K. Red lines are the curve fitting using a 1:1 host-guest binding model. (b) Calculated changes of mole fractions for $TPPC^{3+}$ (blue trace) and $HC_2O_4^- \subset TPPC^{3+}$ (red trace) over the guest-host molar ratio.

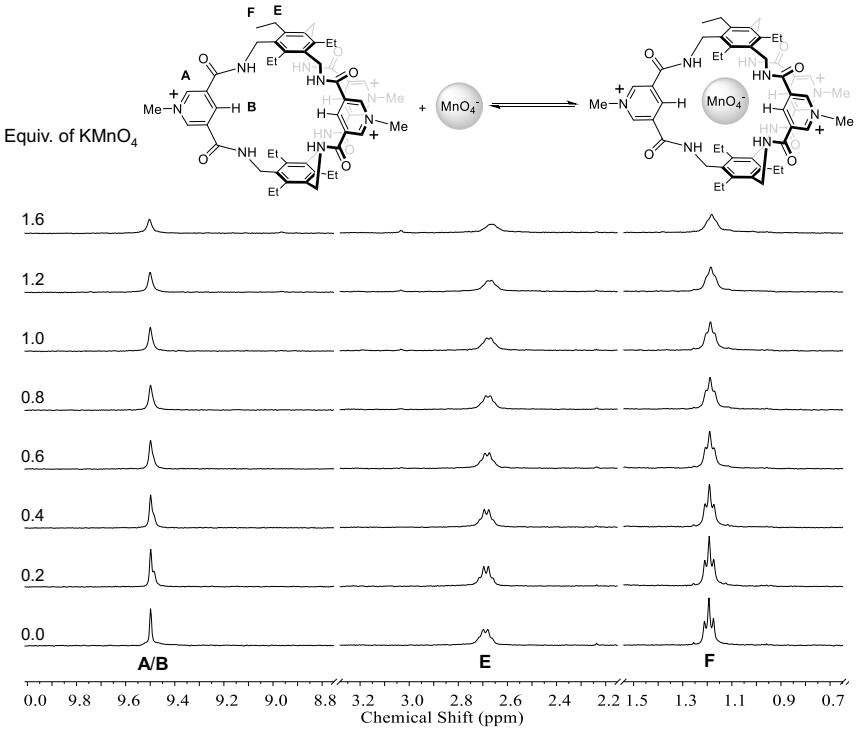

Fig. S43. ^{1}H NMR spectra (400 MHz, D_2O, 298 K) of $TPPC^{3+}$•3Cl^- (0.1 mM) titrated with $KMnO_4$, showing no change in chemical shift.

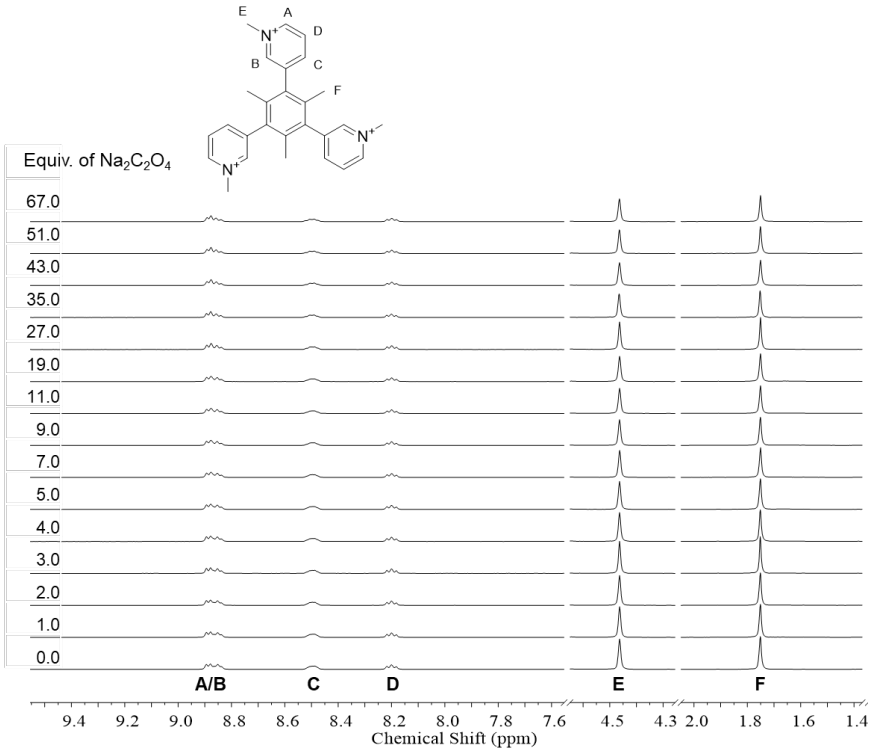

Fig. S44. ^{1}H NMR spectra (400 MHz, D_2O, 298 K) of TPy^{3+}•3Cl^- (4 mM) titrated with $Na_2C_2O_4$, showing no obvious change in chemical shift.

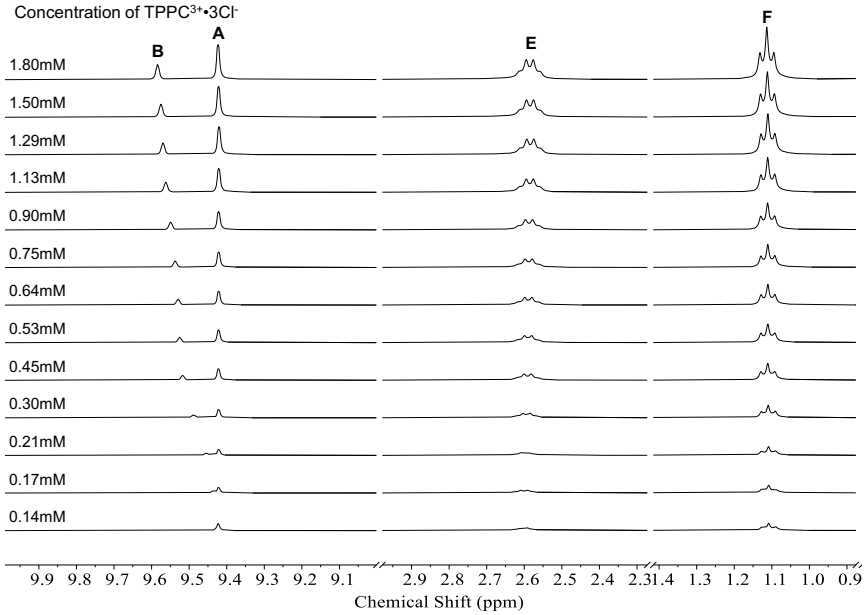

Fig. S45. ^{1}H NMR spectra (400 MHz, D_2O, 298 K) of a sample of $TPPC^{3+}$•$3Cl^{-}$ diluted from 1.80 mM to 0.14 mM.

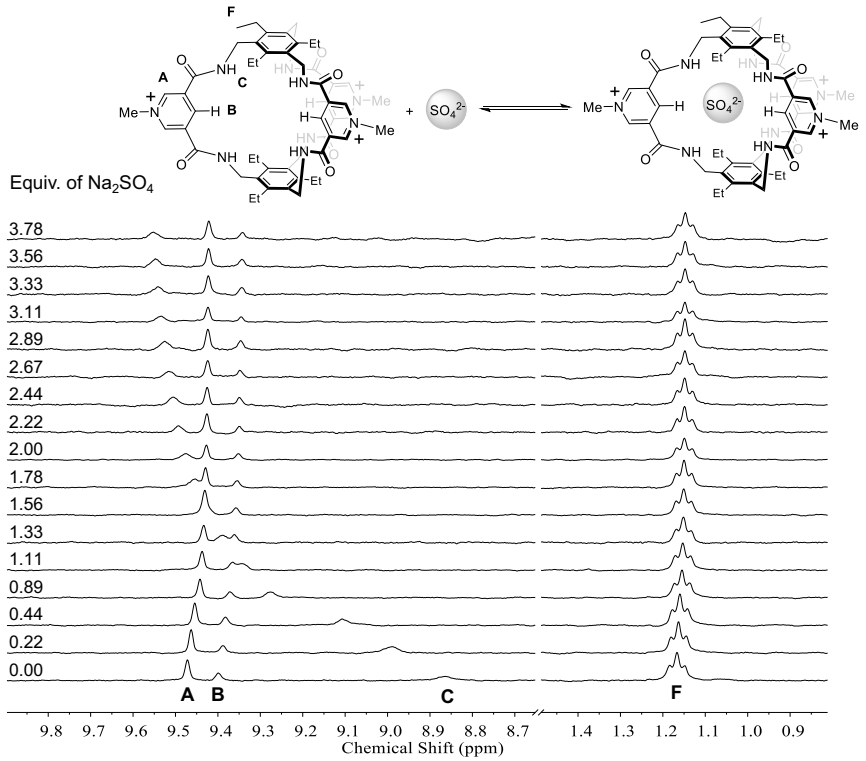

Fig. S46. ^{1}H NMR spectra (400 MHz, 90% H_2O+10% D_2O, 298 K) of $TPPC^{3+}$•$3Cl^{-}$ (0.09 mM) titrated with Na_2SO_4.

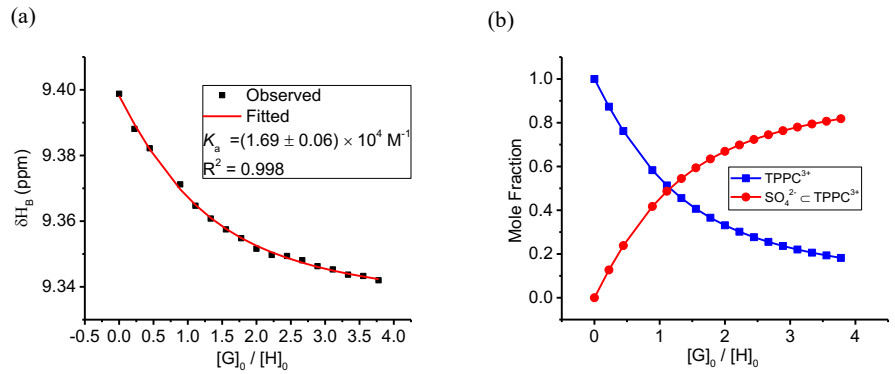

Fig. S47. (a) Titration isotherm created by monitoring changes in the chemical shift of proton B and for $TPPC^{3+}$•3Cl^- (0.09 mM) caused by the addition of Na_2SO_4 in a mixture of 10% D_2O and 90% H_2O at 298 K. Red lines are the curve fitting using a 1:1 host-guest binding model. (b) Calculated changes of mole fractions for $TPPC^{3+}$ (blue trace) and $C_2O_4^{2-}$⊂ $TPPC^{3+}$ (red trace) over the guest-host molar ratio.

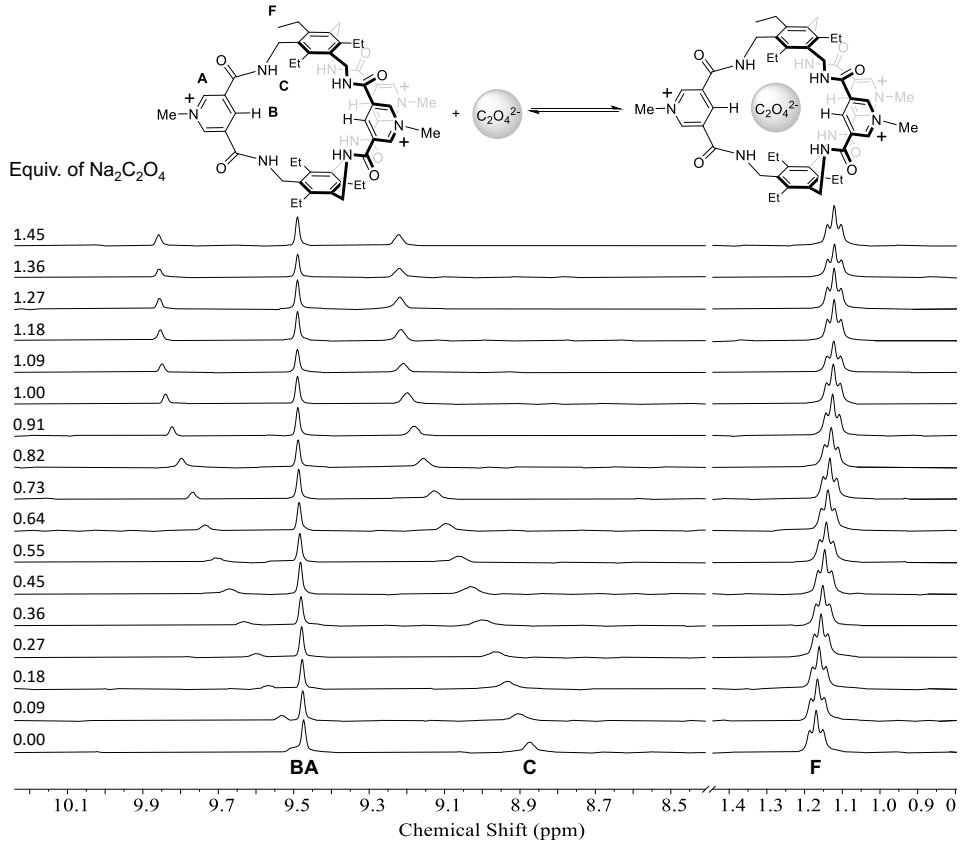

Fig. S48. ^{1}H NMR spectra (400 MHz, 90% H_2O+10% D_2O, 298 K) of $TPPC^{3+}$•3Cl^- (0.22 mM) titrated with $Na_2C_2O_4$.

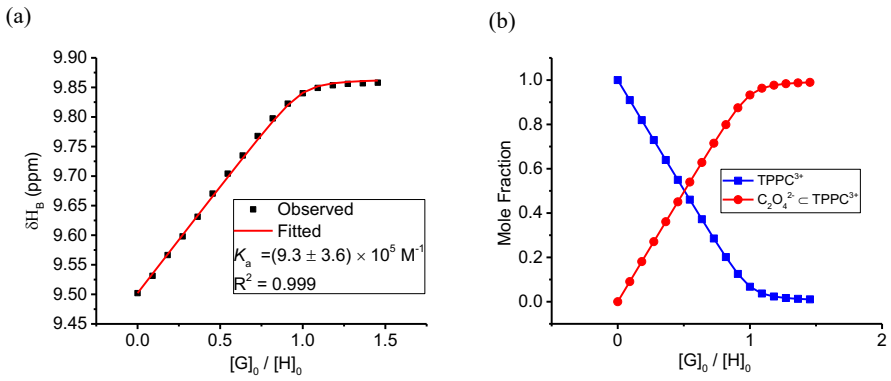

Fig. S49. (a) Titration isotherm created by monitoring changes in the chemical shift of proton B for $TPPC^{3+}$•$3Cl^-$ (0.22 mM) caused by the addition of $Na_2C_2O_4$ in a mixture of 10% D_2O and 90% H_2O at 298 K. Red lines are the curve fitting using a 1:1 host-guest binding model. (b) Calculated changes of mole fractions for $TPPC^{3+}$ (blue trace) and $C_2O_4^{2-}$⊂ $TPPC^{3+}$ (red trace) over the guest-host molar ratio.

5. Isothermal Titration Calorimetry

Isothermal titration was performed on the MicroCal iTC_{200} system at 23 °C. The experiments were conducted in the 200 μL working volume of the sample cell. The capacity of the injection syringe was 40 μL. The stirring speed was set at 750 rpm. Host and guest solutions were prepared in H_2O. A host solution was placed in the titration cell, and the guests were loaded into the titration syringe. In each case, 20-25 injections were performed. The heat of dilution was measured by titrating the guest into a blank solution. The heat of dilution was subtracted before analyzing with MicroCal iTC_{200} software using a 1:1 host-guest binding model and plotted by Origin Lab software.

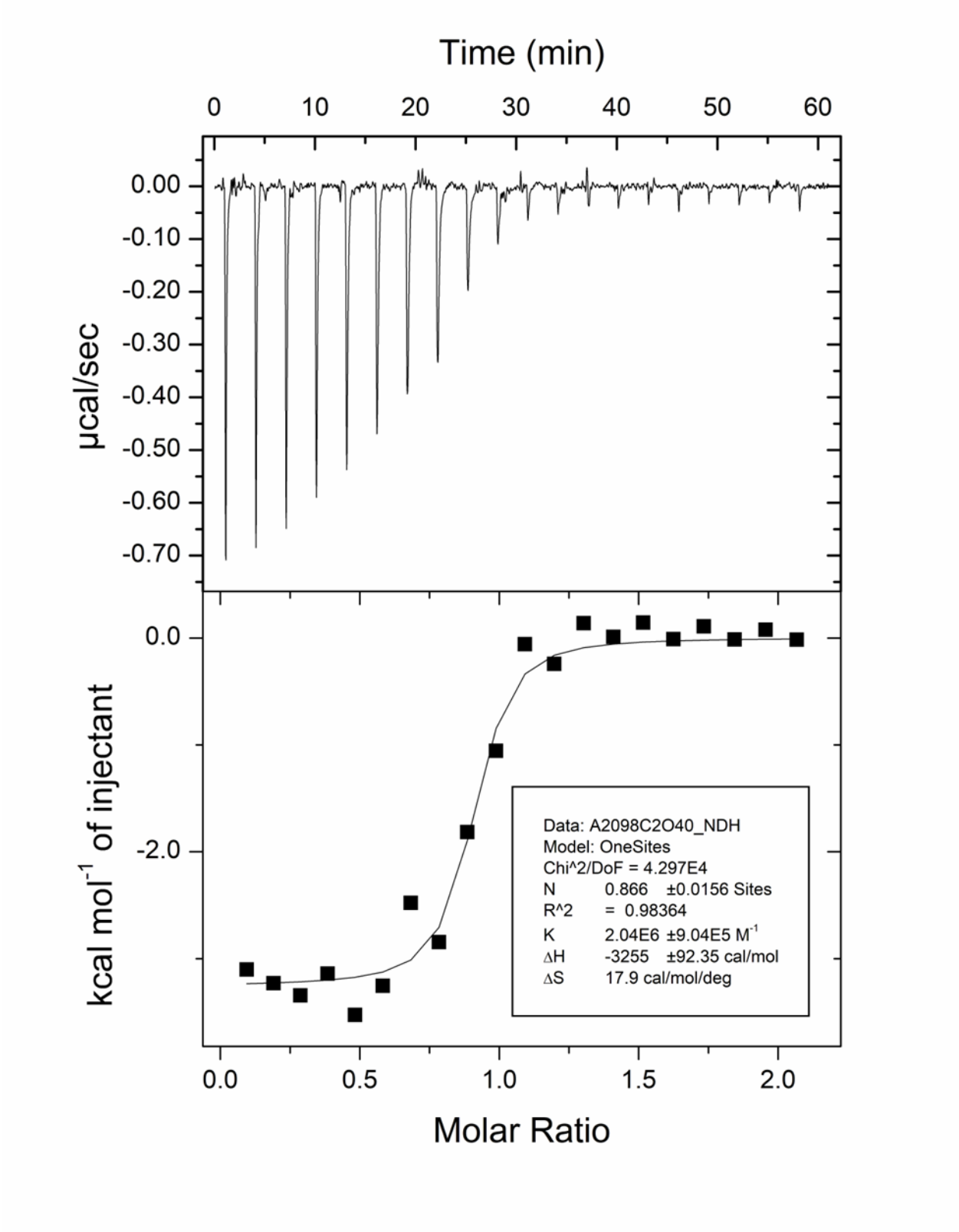

Fig. S50. ITC titration profile of $TPPC^{3+}•3Cl^-$ (0.10 mM) with $Na_2C_2O_4$ in H_2O.

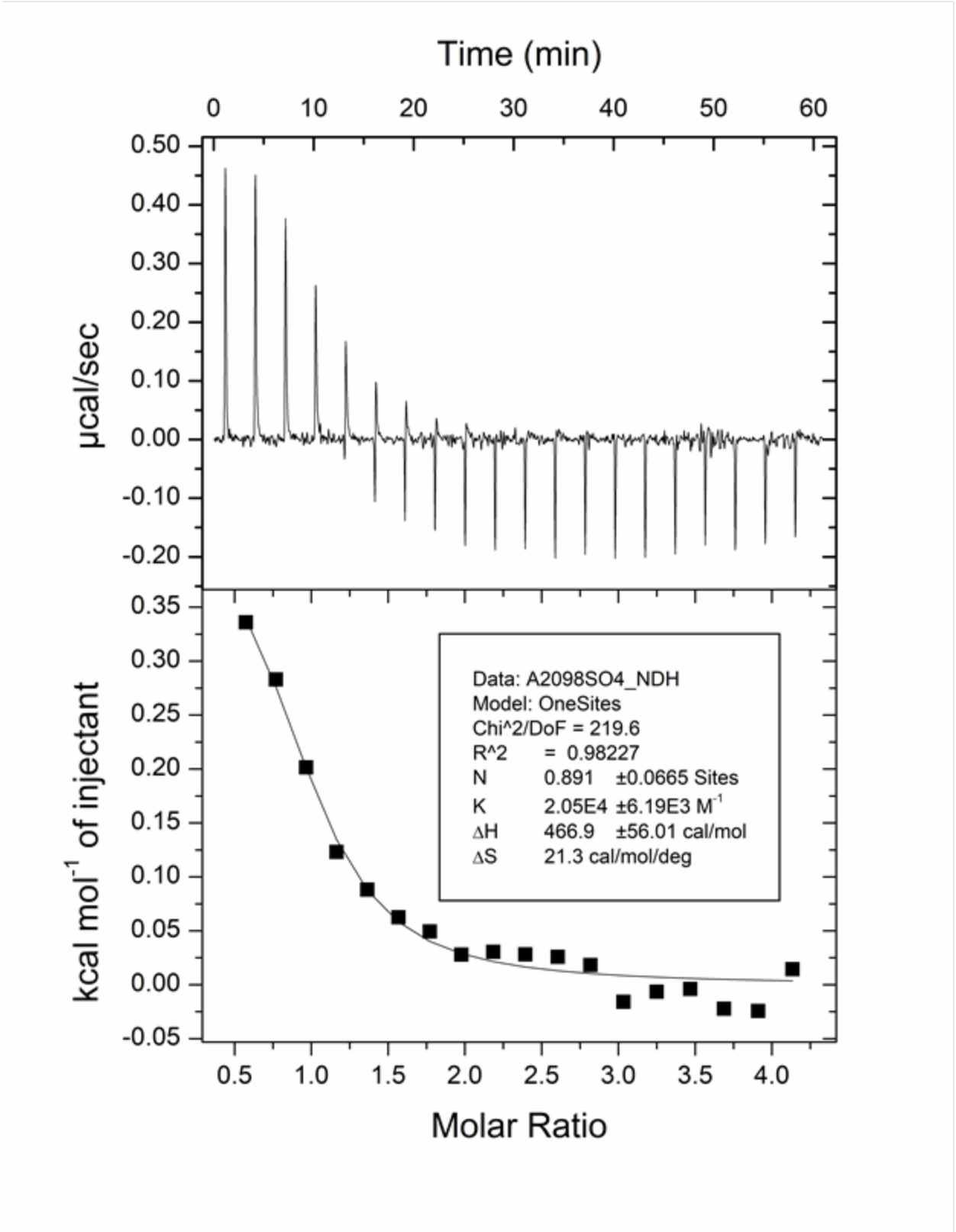

Fig. S51. ITC titration profile of $TPPC^{3+}•3Cl^-$ (0.50 mM) with Na_2SO_4 in H_2O.

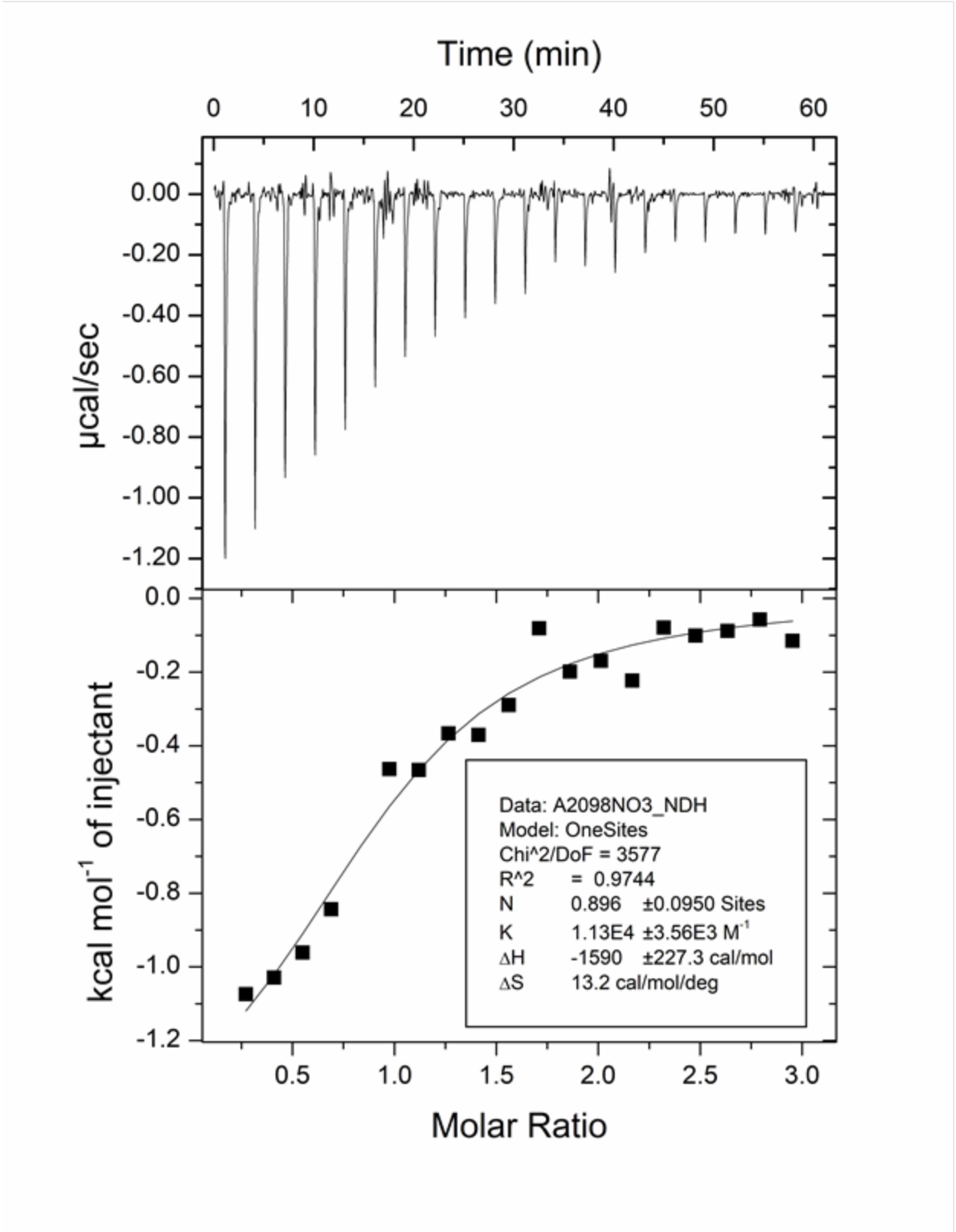

Fig. S52. ITC titration profile of $TPPC^{3+}•3Cl^-$ (0.35 mM) with $NaNO_3$ in H_2O.

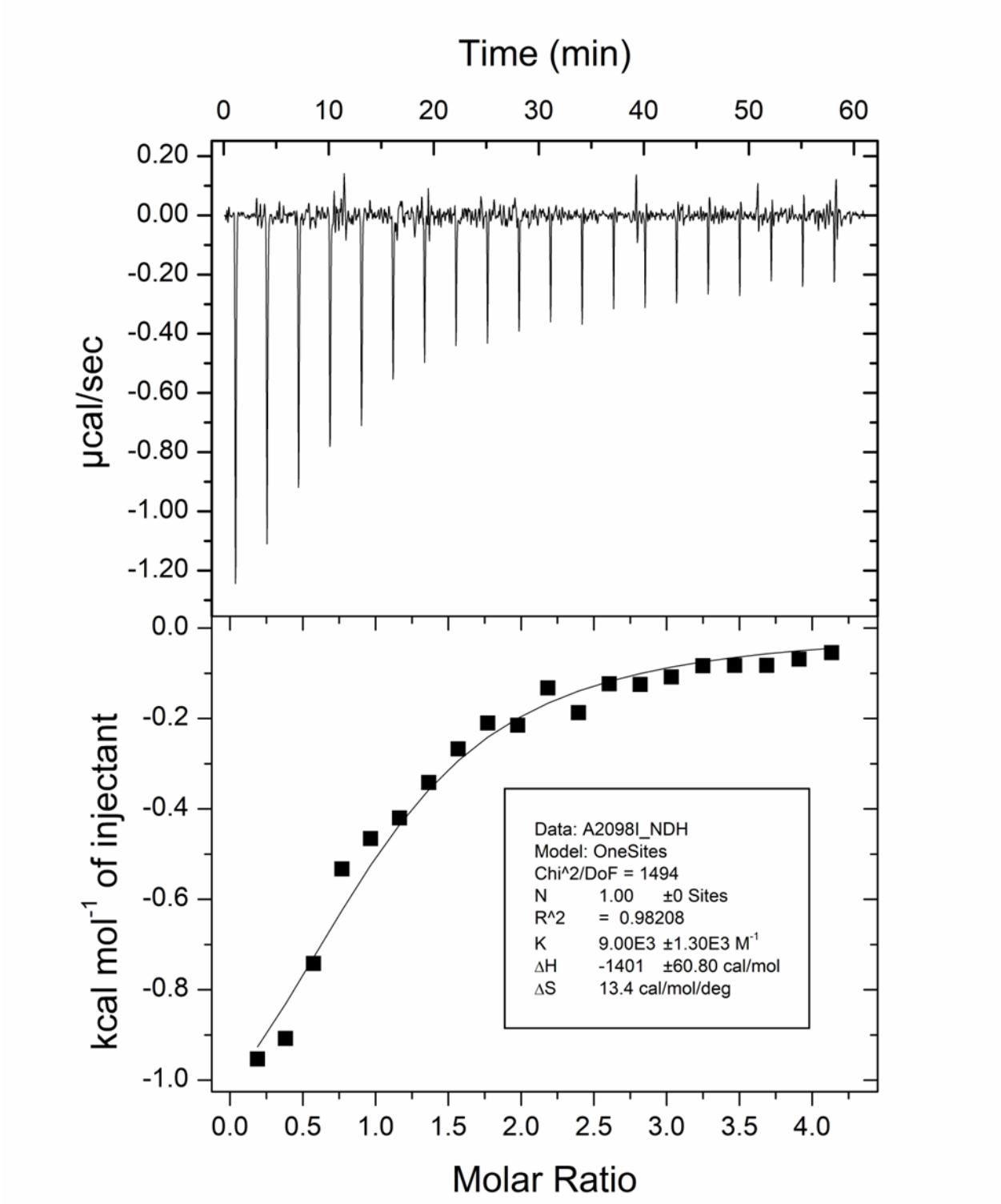

Fig. S53. ITC titration profile of $TPPC^{3+}•3Cl^-$ (0.25 mM) with NaI in H_2O.

6. Catalysis Study by UV-Vis Spectroscopy

The reaction between $H_2C_2O_4$ and $KMnO_4$ was investigated by UV-Vis absorption spectroscopy. A glass cuvette was initially filled with a solution of $KMnO_4$ (0.2 mM, 3mL). The change of the characteristic absorption band of $KMnO_4$ between 400 nm and 700 nm was monitored over 95 minutes after adding $H_2C_2O_4$. Under the same conditions, catalytic amounts (0.2% –10% loading) of $TPPC^{3+}•3Cl^-$ were added to the reaction mixture, and the change of the absorption band of KMnO4 between 400 nm and 700 nm was monitored over 95 minutes. For all experiments, the spectrum was collected every five minutes.

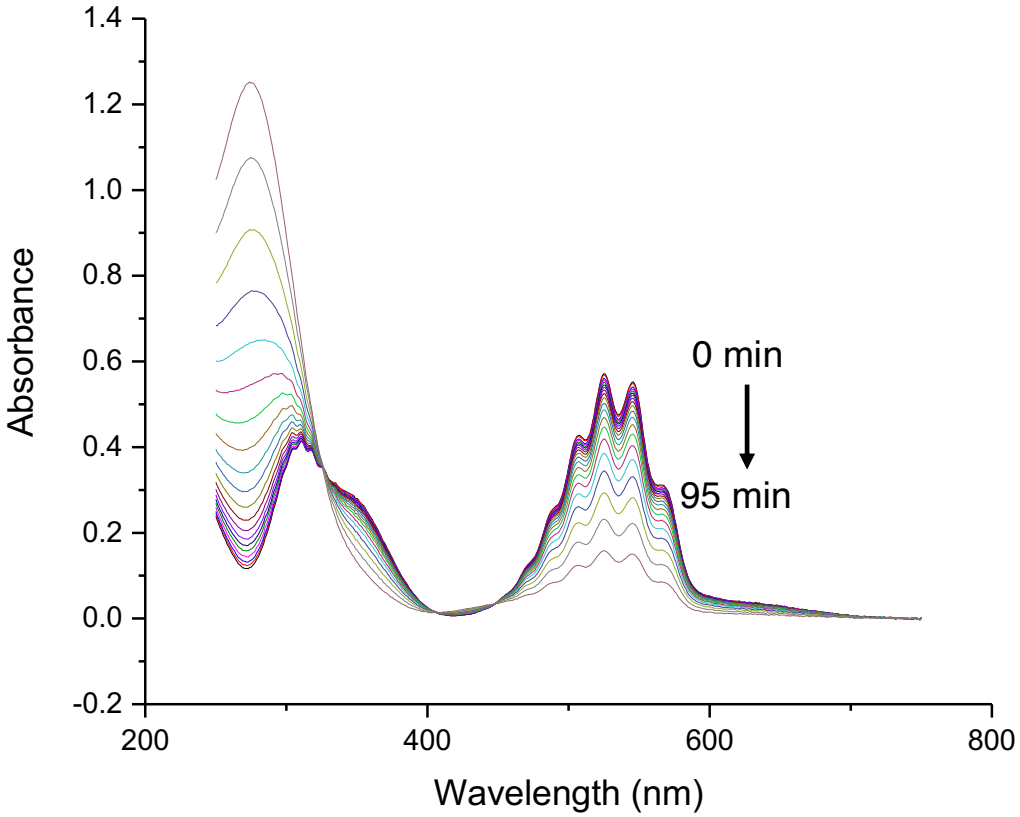

Fig. S54. Change of UV-Vis absorption spectra of a mixture of $KMnO_4$ (0.2 mM) and $H_2C_2O_4$ (1.0 mM) in H_2O over 95 min.

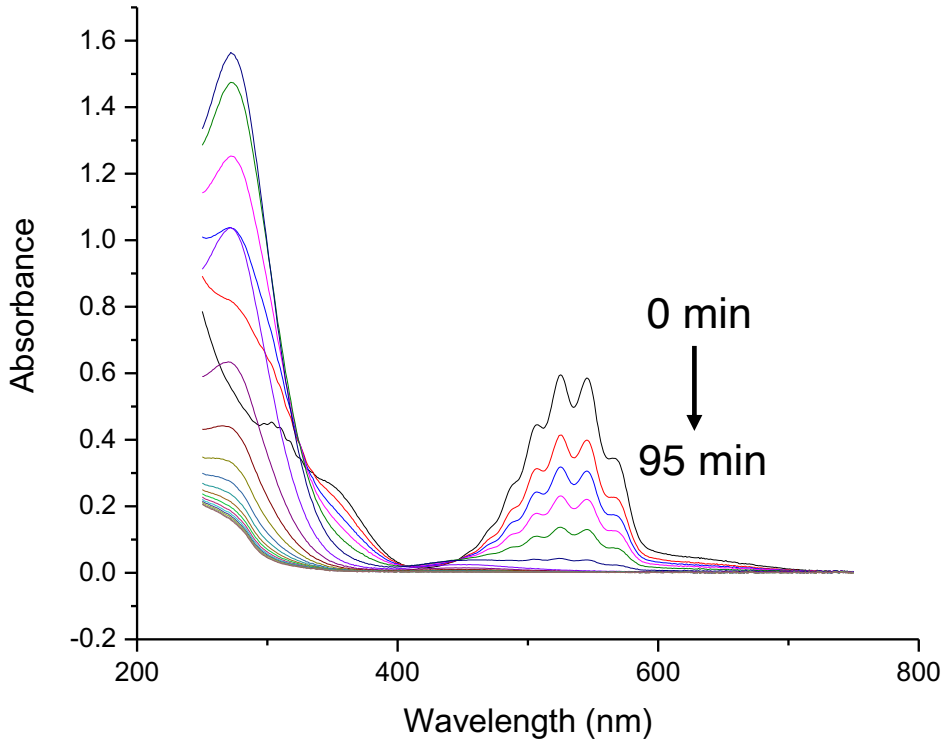

Fig. S55. Change of UV-Vis absorption spectra of a mixture of $KMnO_4$ (0.2 mM), $H_2C_2O_4$ (1.0 mM), and $TPPC^{3+}•3Cl^-$ (20 μM, 10%) in H_2O over 95 min.

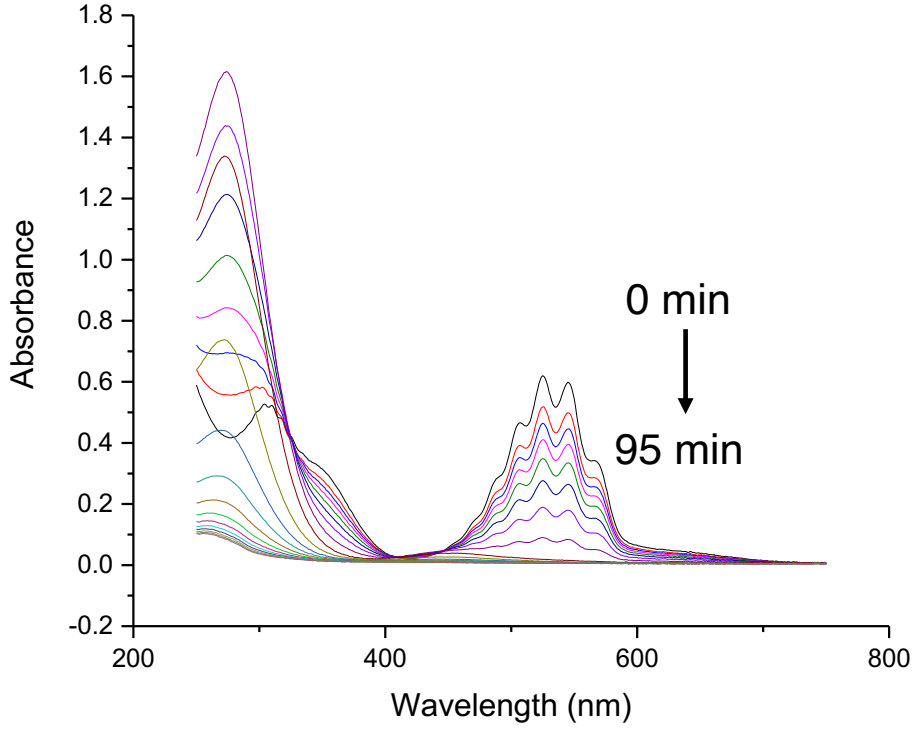

Fig. S56. Change of UV-Vis absorption spectra of a mixture of $KMnO_4$ (0.2 mM), $H_2C_2O_4$ (1.0 mM), and $TPPC^{3+}•3Cl^-$ (10 μM, 5%) in H_2O over 95 min.

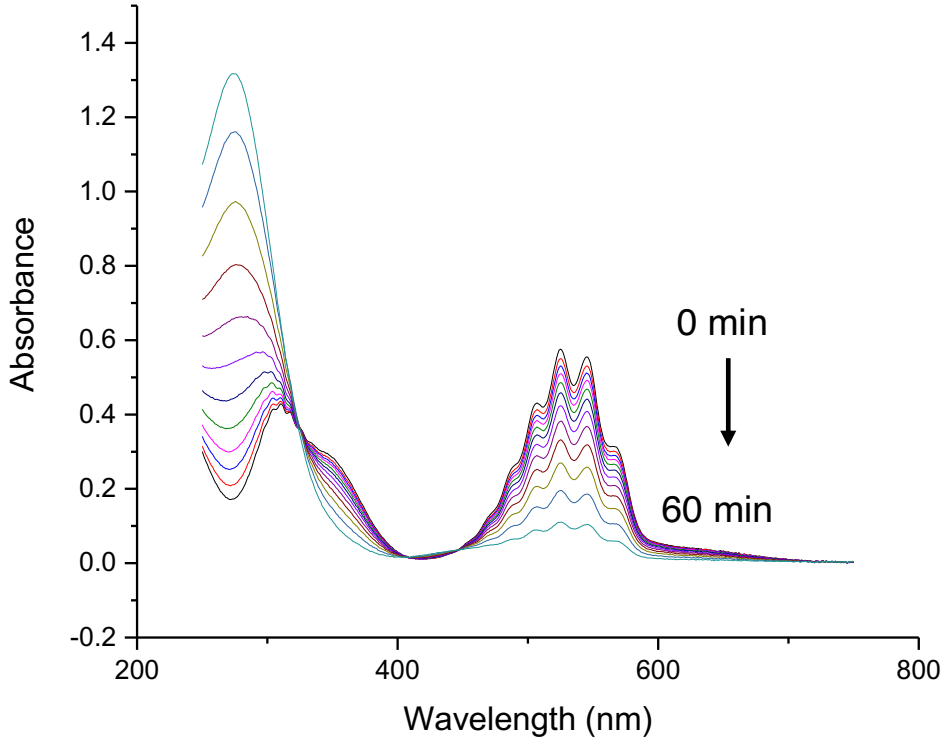

Fig. S57. Change of UV-Vis absorption spectra of a mixture of $KMnO_4$ (0.2 mM), $H_2C_2O_4$ (1.0 mM), and $TPPC^{3+}•3Cl^-$ (2 μM, 1%) in H_2O over 95 min.

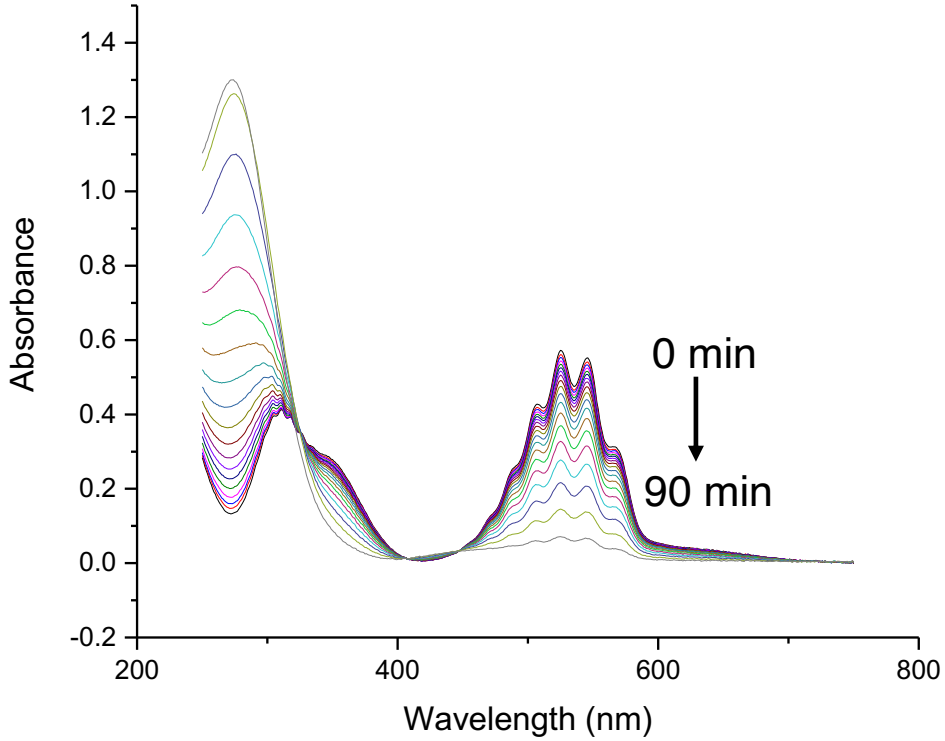

Fig. S58. Change of UV-Vis absorption spectra of a mixture of $KMnO_4$ (0.2 mM), $H_2C_2O_4$ (1.0 mM), and $TPPC^{3+}•3Cl^-$ (0.4 μM, 0.2%) in H_2O over 95 min.

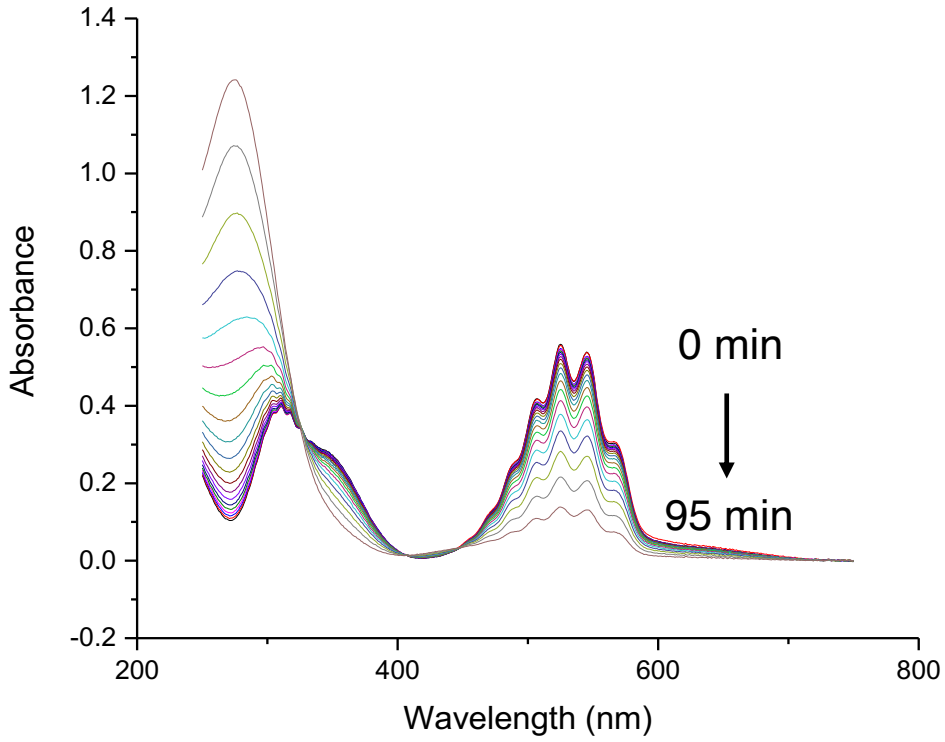

Fig. S59. Change of UV-Vis absorption spectra of a mixture of $KMnO_4$ (0.2 mM), $H_2C_2O_4$ (1.0 mM), and $TPPC^{3+}•3Cl^-$ (0.04 μM, 0.02%) in H_2O over 95 min.

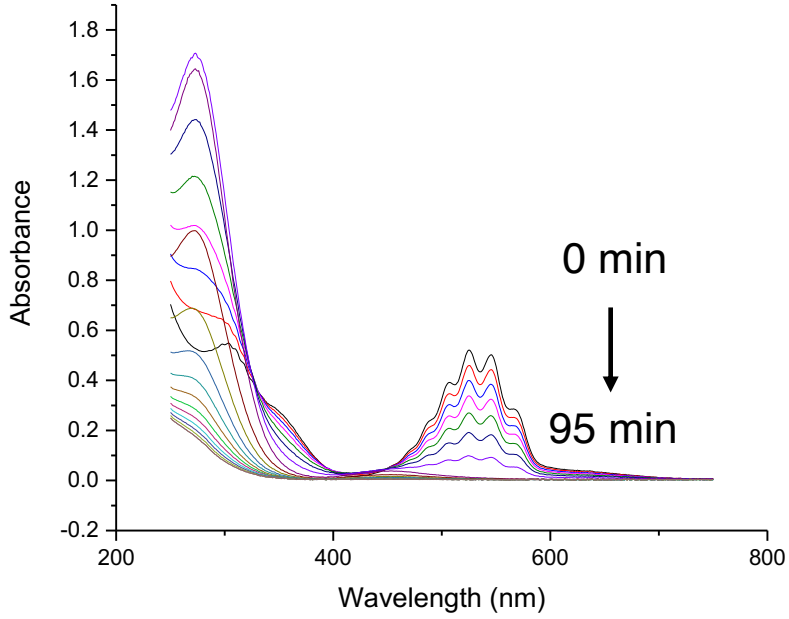

Fig. S60. Change of UV-Vis absorption spectra of a mixture of $KMnO_4$ (0.2 mM), $H_2C_2O_4$ (1.0 mM), $TPPC^{3+}•3Cl^-$ (20 μM, 10%) and Na_2SO_4 (10 mM) in H_2O over 95 min.

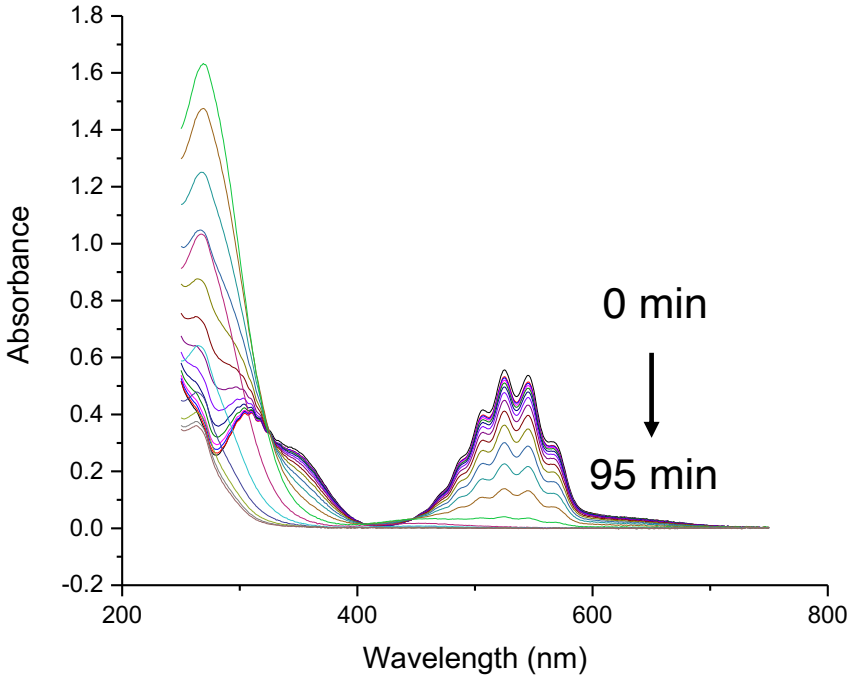

Figure S61. Change of UV-Vis absorption spectra of a mixture of $KMnO_4$ (0.2 mM), $H_2C_2O_4$ (1.0 mM), and $TPy^{3+}•3Cl^-$ (20 μM, 10%) in H_2O over 95 min.

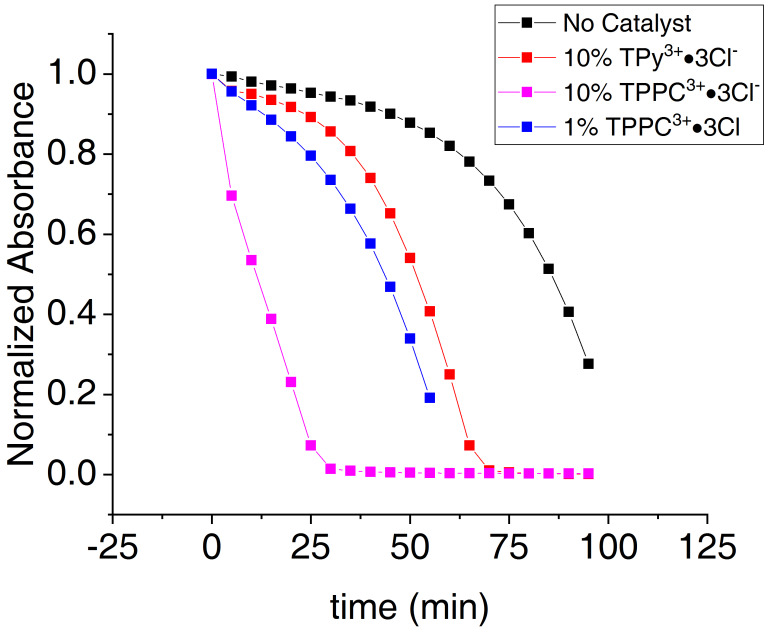

Fig. S62. The changes in absorbance at 525 nm for a $KMnO_4$ solution (0.2 mM) over 95 minutes, demonstrating the effects of $TPy^{3+}•3Cl^-$ (20μM, 10%) and $TPPC^{3+}•3Cl^-$ on the reaction rate acceleration of $H_2C_2O_4$ (1 mM) oxidation.

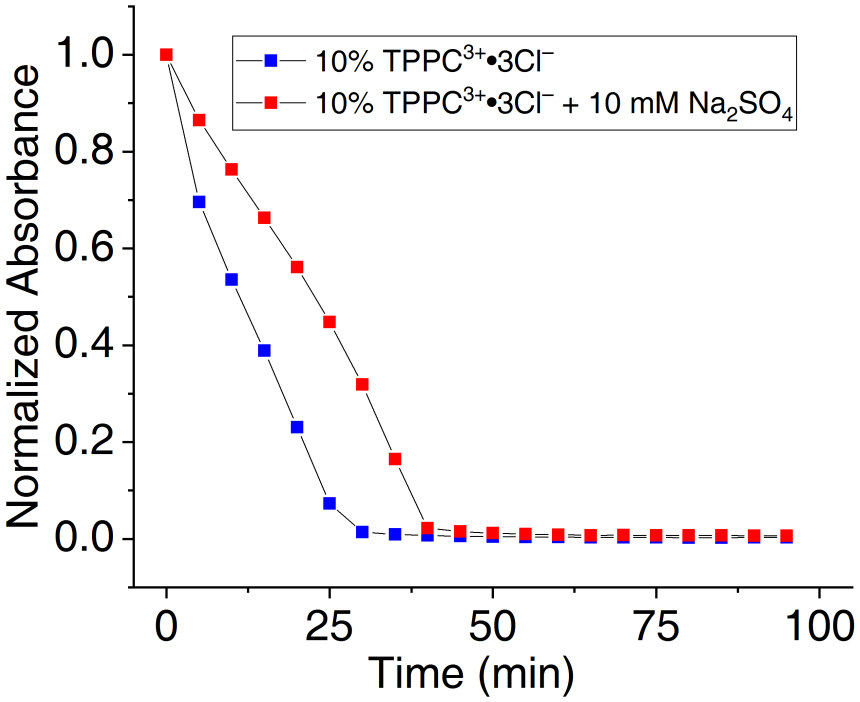

Fig. S63. The changes in absorbance at 525 nm for a $KMnO_4$ solution (0.2 mM) over 95 minutes, demonstrating the effects of Na_2SO_4 (10 mM) on the reaction rate post addition of $H_2C_2O_4$ (1 mM) and $TPPC^{3+}•3Cl^-$ (0.02 mM).

Calculation of catalytic turnover number (TON)

The turnover number (TON) is calculated based on the following formula:

$$TON = \frac{moles\ of\ reactant\ consumed\ with\ the\ help\ of\ TPPC^{3+}}{moles\ of\ catalyst}$$

Under 1% catalyst loading of $TPPC^{3+}•3Cl^-$, 88% of $KMnO_4$ was reduced by $HC_2O_4^-$ within 60 min. In the absence of the catalyst, only 18% of $KMnO_4$ was reduced by $HC_2O_4^-$. Therefore, the moles of reactant consumed with the help of $TPPC^{3+}•3Cl^-$ can be calculated as:

(moles of reactant consumed in the presence of $TPPC^{3+}•3Cl^-$) – (moles of reactant consumed in the absence of $TPPC^{3+}•3Cl^-$)

= (0.2 mM*0.88-0.2 mM*0.18)*3 mL

The mole of the catalyst = (0.2 mM*0.01)*3 mL

Using the equation above, the TON can be calculated as:

$$\boldsymbol{TON = \frac{(0.2\ mM * 0.88 - 0.2 mM * 0.18) * 3\ mL}{(0.2\ mM * 0.01) * 3\ mL} = 70}$$

7. X-Ray Crystallography Data and Analysis

X-ray data and analysis for imine cage 4 (CCDC number: 2334098)

Single crystals of imine cage 4 were obtained by slow diffusion of MeOH to a solution of the cage molecule in CH_2Cl_2. X-ray diffraction data were measured on Bruker D8 Venture Photon II diffractometer equipped with a Cu Kα INCOATEC ImuS micro-focus source (λ = 1.54178 Å). Indexing was performed using APEX4[S3] (Difference Vectors method). Data integration and reduction were performed using SaintPlus [S4]. Absorption correction was performed by the multi-scan method implemented in SADABS [S5]. The space group was determined using XPREP implemented in APEX3. The structure was solved using SHELXT [S \6] and refined using SHELXL-2019/1 [S7] (full-matrix least-squares on F2) through OLEX2 interface program [S8]. The ellipsoid plot was made with Platon [S9]. Disordered solvent molecules were refined with restraints. Some of the disordered atoms were refined as O atoms (tentatively H_2O or CH_3OH). Data and refinement conditions are shown in Table S1.

Table S1 Crystal data and structure refinement for imine cage 4.	
Identification code	2094
Empirical formula	$C_{53.64}H_{68.34}Cl_{2.02}N_9O_{3.43}$
Moiety formula	C_{51} H_{57} N_9, 1.012(CH_2Cl_2), 1.627(CH_3OH), 1.403(H_2O), 0.404$(O)_{solv}$
Formula weight	965.77
Temperature/K	100.00
Crystal system	monoclinic
Space group	$P2_1/n$
a/Å	14.9701(3)
b/Å	24.0962(6)
c/Å	15.7004(4)
α/°	90
β/°	116.0400(10)
γ/°	90
Volume/$Å^3$	5088.6(2)
Z	4
$\rho_{calc}g/cm^3$	1.261
μ/mm^{-1}	1.579
F(000)	2060.0
Crystal size/mm^3	0.25 × 0.18 × 0.07
Radiation	CuKα (λ = 1.54178)
2Θ range for data collection/°	6.804 to 159.084
Index ranges	$-18 \leq h \leq 19$, $-30 \leq k \leq 30$, $-19 \leq l \leq 18$
Reflections collected	120441
Independent reflections	10976 [R_{int} = 0.0354, R_{sigma} = 0.0160]
Data/restraints/parameters	10976/80/713
Goodness-of-fit on F^2	1.036
Final R indexes [I>=2σ (I)]	R_1 = 0.0480, wR_2 = 0.1308
Final R indexes [all data]	R_1 = 0.0506, wR_2 = 0.1331
Largest diff. peak/hole / e $Å^{-3}$	0.67/-0.37

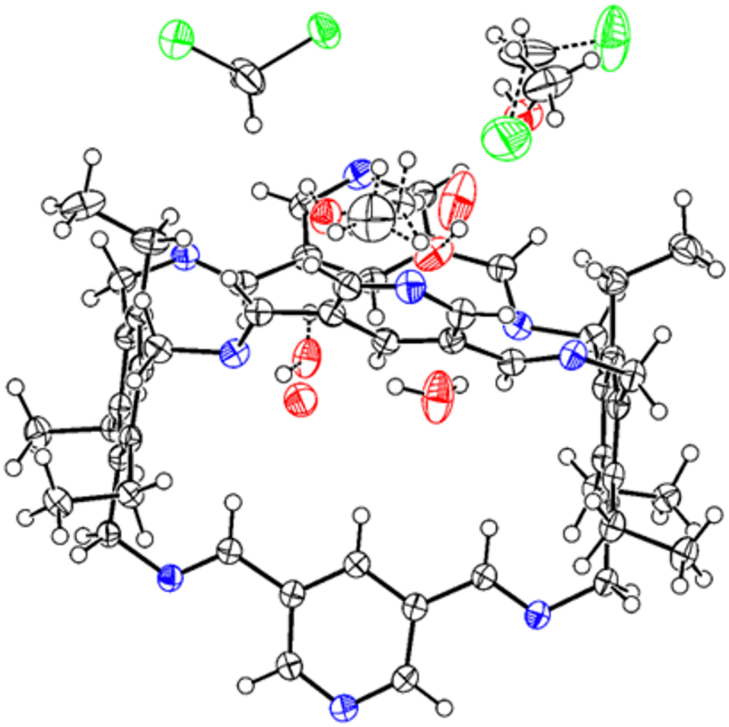

Fig. S64. The ellipsoid plot of the imine cage 4. Anisotropic displacement parameters were drawn at a 50% probability level.

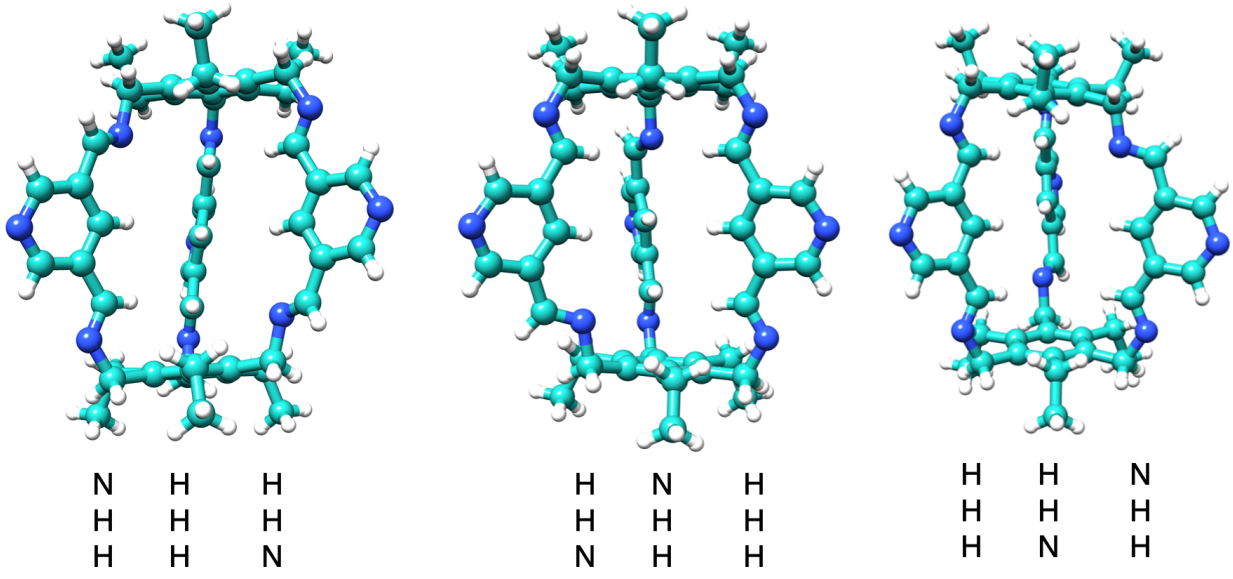

Fig. S65. Front and side views of the imine cage 4, showing the different orientations of the three pyridine bridges. Solvent molecules were omitted for the sake of clarity.

X-ray data and analysis for $TPPC^{3+}•3Cl^-$ (CCDC number: 2334101)

Single crystals of $TPPC^{3+}•3Cl^-$ were obtained by slow diffusion of iPr_2O into a solution of $TPPC^{3+}•3Cl^-$ in DMSO. X-ray diffraction data were measured on Bruker D8 Venture Photon II diffractometer equipped with a Cu Kα INCOATEC ImuS micro-focus source (λ = 1.54178 Å). Indexing was performed using APEX4 [S3] (Difference Vectors method). Data integration and reduction were performed using SaintPlus [S4]. Absorption correction was performed by the multi-scan method implemented in SADABS [S5]. The space group was determined using XPREP implemented in APEX3. The structure was solved using SHELXT [S6] and refined using SHELXL-2019/1 [S7] (full-matrix least-squares on F2) through OLEX2 interface program [S8]. The ellipsoid plot was made with Platon [S9]. Due to disorder the locations of some Cl^- anions are tentative. Disordered solvent molecules were refined with restraints. Some of the disordered atoms were refined as O atoms (tentatively H_2O but also DMSO/DMF/ACN were possible). Data and refinement conditions are shown in Table S2.

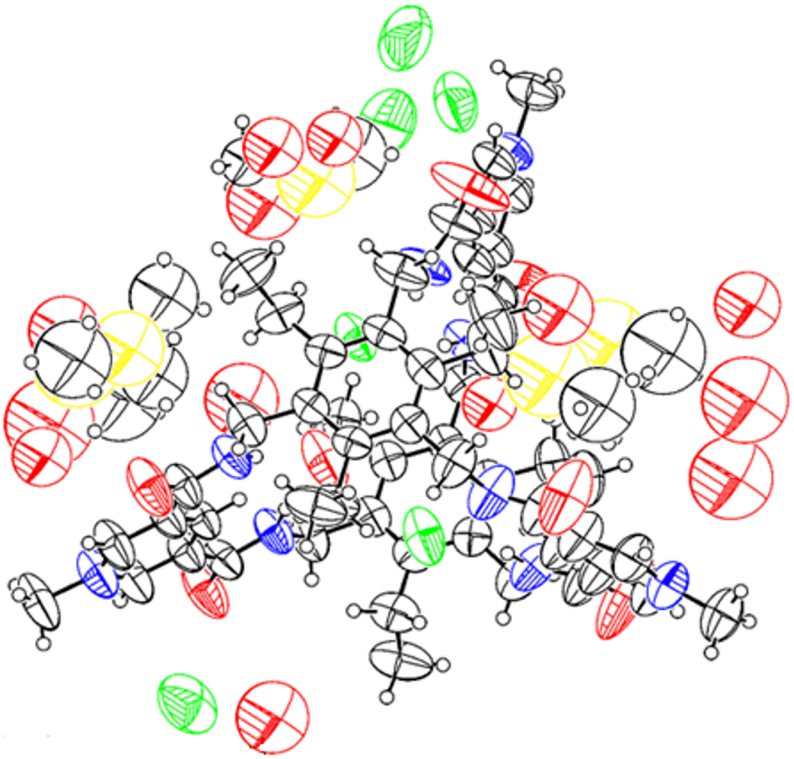

Fig. S66. The ellipsoid plot of $TPPC^{3+}•3Cl^-$. Anisotropic displacement parameters were drawn at a 50% probability level.

Table S2 Crystal data and structure refinement for $TPPC^{3+}•3Cl^{-}$.

Identification code	117_4_3
Empirical formula	$C_{57.3}H_{75.91}Cl_3N_9O_{12.41}S_{1.65}$
Moiety formula	$C_{54}H_{66}N_9O_6$, 3(Cl), 1.651(C_2H_6SO), 4.764$(O)_{solv}$
Formula weight	1248.66
Temperature/K	107.00
Crystal system	triclinic
Space group	P-1
a/Å	14.9459(6)
b/Å	15.2203(7)
c/Å	18.4006(8)
α/°	67.614(3)
β/°	81.558(3)
γ/°	68.560(3)
Volume/$Å^3$	3602.4(3)
Z	2
$\rho_{calc}g/cm^3$	1.151
μ/mm^{-1}	2.079
F(000)	1319.0
Crystal size/mm^3	0.04 × 0.03 × 0.02
Radiation	CuKα (λ = 1.54178)
2Θ range for data collection/°	5.194 to 99.5
Index ranges	$-14 \le h \le 14$, $-15 \le k \le 15$, $-18 \le l \le 18$
Reflections collected	49602
Independent reflections	7315 [R_{int} = 0.1471, R_{sigma} = 0.1103]
Data/restraints/parameters	7315/1269/815
Goodness-of-fit on F^2	1.295
Final R indexes [I>=2σ (I)]	R_1 = 0.1361, wR_2 = 0.3432
Final R indexes [all data]	R_1 = 0.1968, wR_2 = 0.3934
Largest diff. peak/hole / e $Å^{-3}$	0.64/-0.36

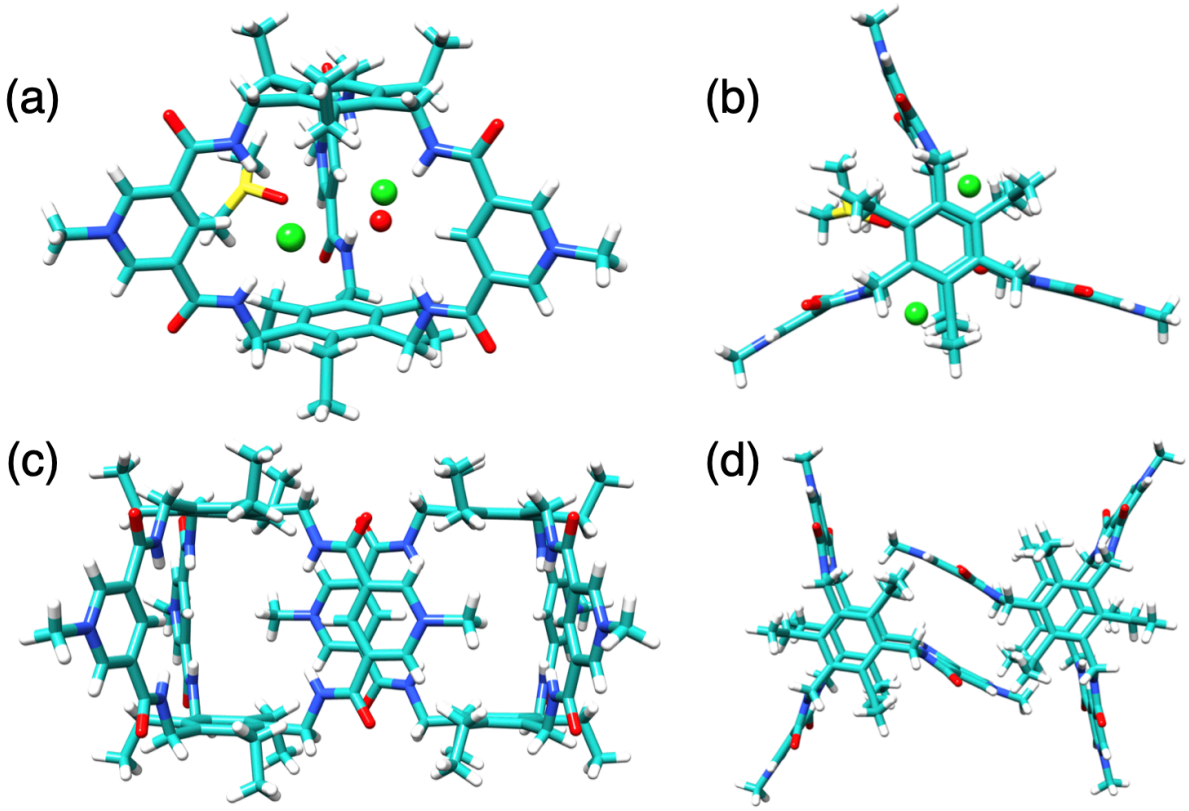

Fig. S67. (a) Front and (b) top view of $TPPC^{3+}$ encapsulated with two Cl^{-}, one H_2O, and one DMSO guests. (c) Front and (d) top view of dimeric $TPPC^{3+}$ in the crystal lattice.

X-ray data and analysis for $TPPC^{3+}$•$3I^{-}$ (CCDC number: 2334102)

Single crystals of $TPPC^{3+}$•$3I^{-}$ were obtained by slow diffusion of Et_2O into a solution of $TPPC^{3+}$•$3PF_6^{-}$ and tetraethyl ammonium iodide in MeCN. X-ray diffraction data were measured on Bruker D8 Venture Photon II diffractometer equipped with a Cu Kα INCOATEC ImuS micro-focus source (λ = 1.54178 Å). Indexing was performed using APEX4 [S3] (Difference Vectors method). Data integration and reduction were performed using SaintPlus [S4]. Absorption correction was performed by the multi-scan method implemented in SADABS [S5]. The space group was determined using XPREP implemented in APEX3. The structure was solved using SHELXT [S6] and refined using SHELXL-2019/1 [S7] (full-matrix least-squares on F2) through OLEX2 interface program [S8]. The ellipsoid plot was made with Platon [S9]. Disordered solvent molecules were refined with restraints. Some of the disordered atoms were refined as O atoms (tentatively H_2O). Data and refinement conditions are shown in Table S3.

Table S3 Crystal data and structure refinement for $TPPC^{3+}•3I^-$

Identification code	VL_CX_2098PF6_TEAI_1_ACN_Et2O
Empirical formula	$C_{65.04}H_{85.33}I_3N_{14.52}O_{8.38}$
Moiety formula	$C_{54}H_{66}N_9O_6$, 3(I), 5.519(C_2H_3N), 1.39(H_2O), 0.994$(O)_{solv}$
Formula weight	1585.36
Temperature/K	100.00
Crystal system	monoclinic
Space group	$P2_1/n$
a/Å	14.8832(2)
b/Å	32.8405(5)
c/Å	15.3240(2)
α/°	90
β/°	102.8042(7)
γ/°	90
Volume/Å^3	7303.69(18)
Z	4
ρ_{calc}g/cm^3	1.442
μ/mm^{-1}	10.573
F(000)	3213.0
Crystal size/mm^3	0.09 × 0.04 × 0.02
Radiation	CuKα (λ = 1.54178)
2Θ range for data collection/°	5.382 to 158.522
Index ranges	$-16 \le h \le 18$, $-40 \le k \le 41$, $-19 \le l \le 19$
Reflections collected	156372
Independent reflections	15540 [R_{int} = 0.0518, R_{sigma} = 0.0296]
Data/restraints/parameters	15540/197/963
Goodness-of-fit on F^2	1.039
Final R indexes [I>=2σ (I)]	R_1 = 0.0355, wR_2 = 0.1003
Final R indexes [all data]	R_1 = 0.0367, wR_2 = 0.1012
Largest diff. peak/hole / e Å^{-3}	1.76/-1.27

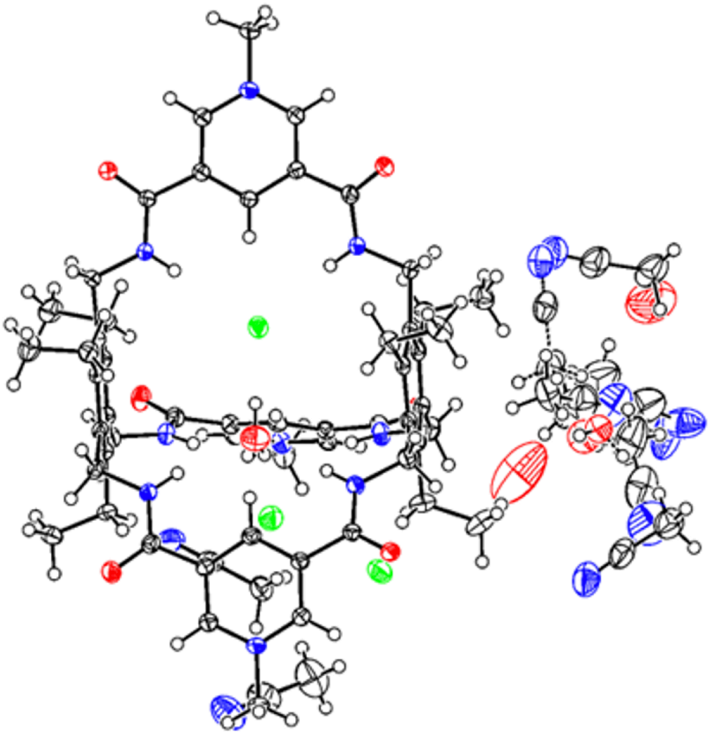

Fig. S68. The ellipsoid plot of $TPPC^{3+}$•$3I^{-}$. Anisotropic displacement parameters were drawn at a 50% probability level.

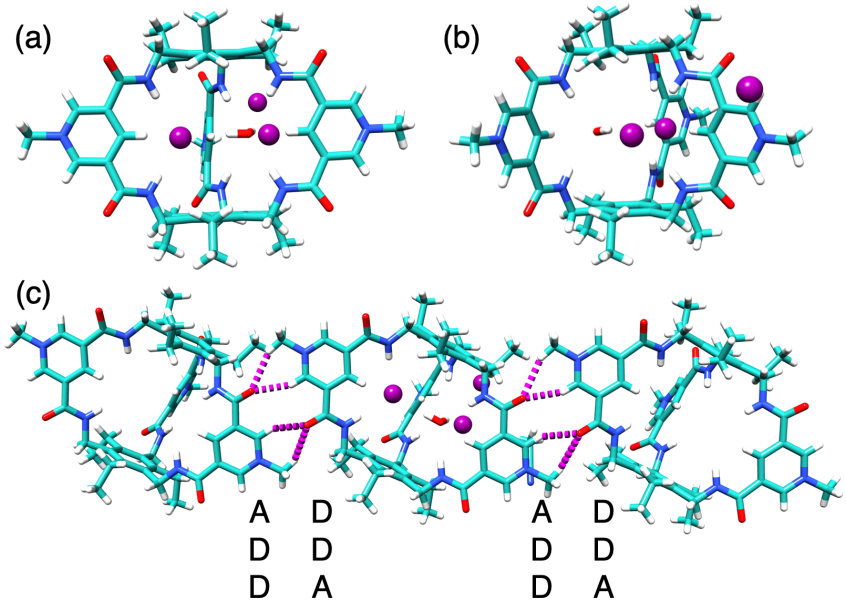

Fig. S69. Front (a) and side-on (b) view of $TPPC^{3+}$•$3I^{-}$. (c) ADD‑DDA hydrogen bonding arrays observed between $TPPC^{3+}$•$3I^{-}$ in the crystal lattice.

X-ray data and analysis for $TPPC^{3+}•3CF_3COO^-$ (CCDC number: 2334103)

Single crystals of $TPPC^{3+}•3CF_3COO^-$ were obtained by slow diffusion of iPr_2O into a solution of $TPPC^{3+}•3Cl^-$ and TFA in MeCN. X-ray diffraction data were measured on Bruker D8 Venture Photon III diffractometer equipped with a Cu Kα INCOATEC ImuS micro-focus source (λ = 1.54178 Å). Indexing was performed using APEX4 [S3] (Difference Vectors method). Data integration and reduction were performed using SaintPlus [S4]. Absorption correction was performed by the multi-scan method implemented in SADABS [S5]. The space group was determined using XPREP implemented in APEX3. The structure was solved using SHELXT [S6] and refined using SHELXL-2019/1 [S7] (full-matrix least-squares on F2) through OLEX2 interface program [S8]. The contribution of heavily disordered content in structural voids was treated as diffuse using a solvent mask procedure implemented in the Olex2 program [S8]. The ellipsoid plot was made with Platon [S9]. Data and refinement conditions are shown in Table S4.

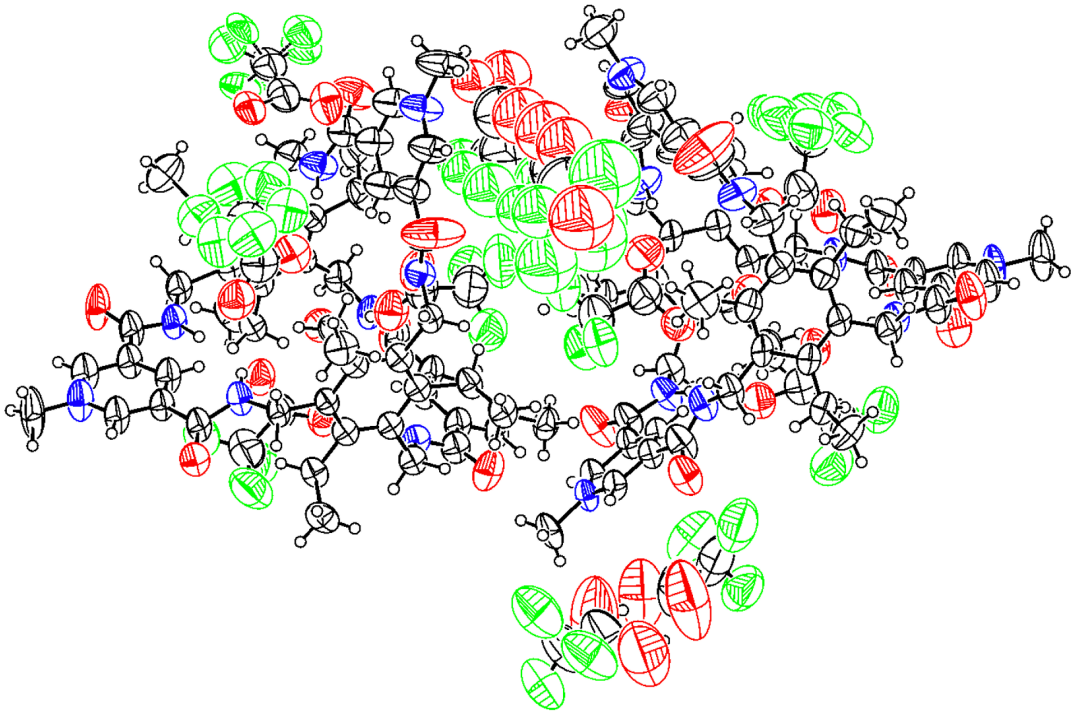

Fig. S70. The ellipsoid plot of $TPPC^{3+}•3CF_3COO^-$. Anisotropic displacement parameters were drawn at a 50% probability level.

Table S4. Crystal data and structure refinement for $TPPC^{3+}•3CF_3COO^-$.	
Identification code	127_7
Empirical formula	$C_{64.2}H_{67}F_{15.31}N_9O_{17.7}$
Moiety formula	C_{54} H_{66} N_9 O_6, 3($C_2F_3O_2$), 2.1C_2HF_3O2, 1.5(H_2O)
Formula weight	1538.84
Temperature/K	100.00
Crystal system	triclinic
Space group	P-1
a/Å	13.0460(10)
b/Å	25.708(2)
c/Å	27.482(2)
α/°	113.091(5)
β/°	99.699(5)
γ/°	92.773(5)
Volume/Å^3	8290.6(11)
Z	4
ρ_{calc}g/cm^3	1.233
μ/mm^{-1}	0.983
F(000)	3179.0
Radiation	CuKα (λ = 1.54178)
2Θ range for data collection/°	6.156 to 71.464
Index ranges	$-9 \leq h \leq 9$, $-19 \leq k \leq 19$, $-20 \leq l \leq 20$
Reflections collected	54411
Independent reflections	7551 [R_{int} = 0.1251, R_{sigma} = 0.0891]
Data/restraints/parameters	7551/3397/2051
Goodness-of-fit on F^2	1.367
Final R indexes [I>=2σ (I)]	R_1 = 0.1091, wR_2 = 0.3060
Final R indexes [all data]	R_1 = 0.1366, wR_2 = 0.3349
Largest diff. peak/hole / e Å^{-3}	0.69/-0.37

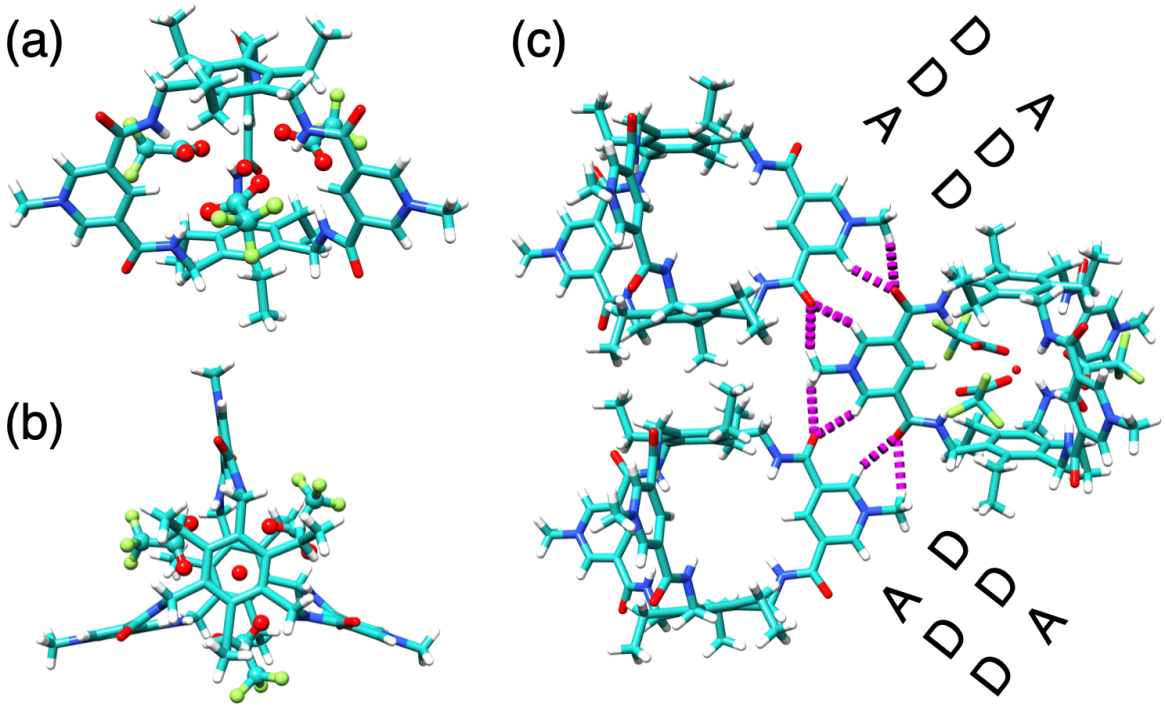

Fig. S71. (a) Front and top (b) view of $TPPC^{3+}$•$3CF_3COO^-$. (c) ADD‑DDA hydrogen bonding arrays observed between $TPPC^{3+}$•$3CF_3COO^-$ in the crystal lattice.

8. Computational Analysis

Structural optimization

The *xyz* coordinates for the calculations were either extracted from the X-ray single crystal data or directly created using GaussView 6 program. All optimizations were performed with density functional theory (DFT) in the Orca program [S10] (version 5.0.3) using the Becke '88 exchange and Lee-Yang-Parr correlation (BLYP) functional [S11], the Ahlrich's double zeta Def2-SVP basis sets [S12] with geometrical counterpoise (gCP) scheme [S13], and Grimme's third-generation dispersion correction [S14] with Beck Johnson damping (D3BJ). To speed up the DFT optimizations, the Coulomb integral [S15] and numerical chain-of-sphere integration [S16] for the HF exchanges (RIJCOSX) method were applied with the Def2/J auxiliary basis (AuxJ) [S17]. All optimizations were performed in a water continuum with the Conductor-like Polarizable Continuum Model (CPCM) in Orca. Frequency calculations of the resulting optimized structures reveal no imaginary frequency, suggesting the optimized structures were in local energy minima.

Visualization of Noncovalent Interactions

Independent Gradient Model (IGM) analysis [S18] is an approach to identify and visualize intermolecular interactions. Strong polar attractions and weak van der Waals contacts are visualized as an iso-surface with blue and green colors, respectively. DFT optimized structures were used as input files. The binding surface was calculated by Multiwfn 3.6 program [S19] through function 20 (visual study of weak interaction) and visualized by Chimera software [S20].

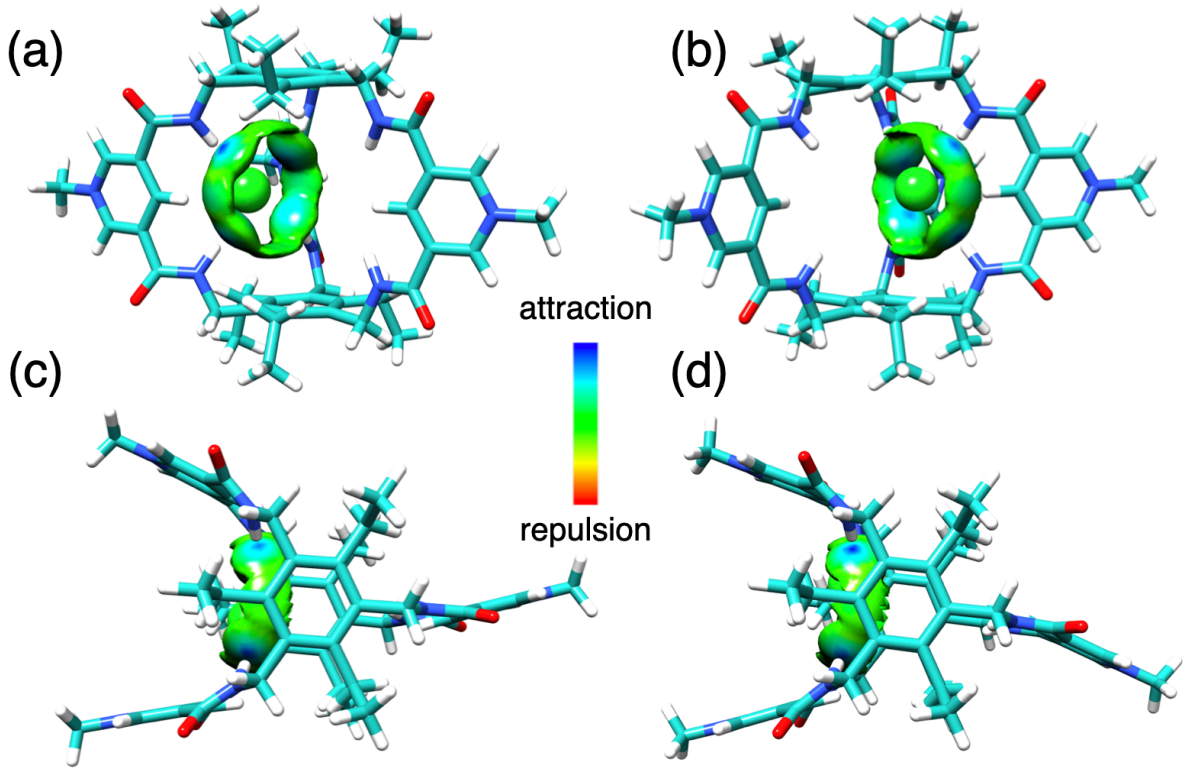

Fig. S72. Front (a), side-on (b), top (c), and bottom (d) view of $Cl^{-}\subset TPPC^{3+}$ from IGM analysis showing a noncovalent interaction isosurface of $\delta g^{inter} = 0.003$ a.u; color coding in the electron density range of $-0.05<\text{sign}(\lambda_2)\rho<+0.05$ a.u.

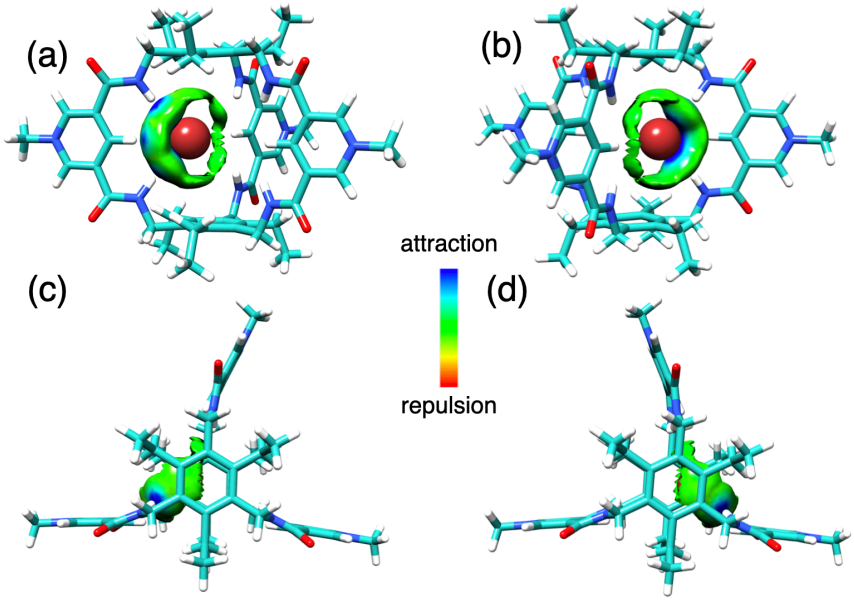

Fig. S73. Front (a), side-on (b), top (c), and bottom (d) view of $Br^{-}\subset TPPC^{3+}$ from IGM analysis showing a noncovalent interaction isosurface of δg^{inter} = 0.003 a.u; color coding in the electron density range of –0.05<sign (λ_2)ρ <+0.05 a.u.

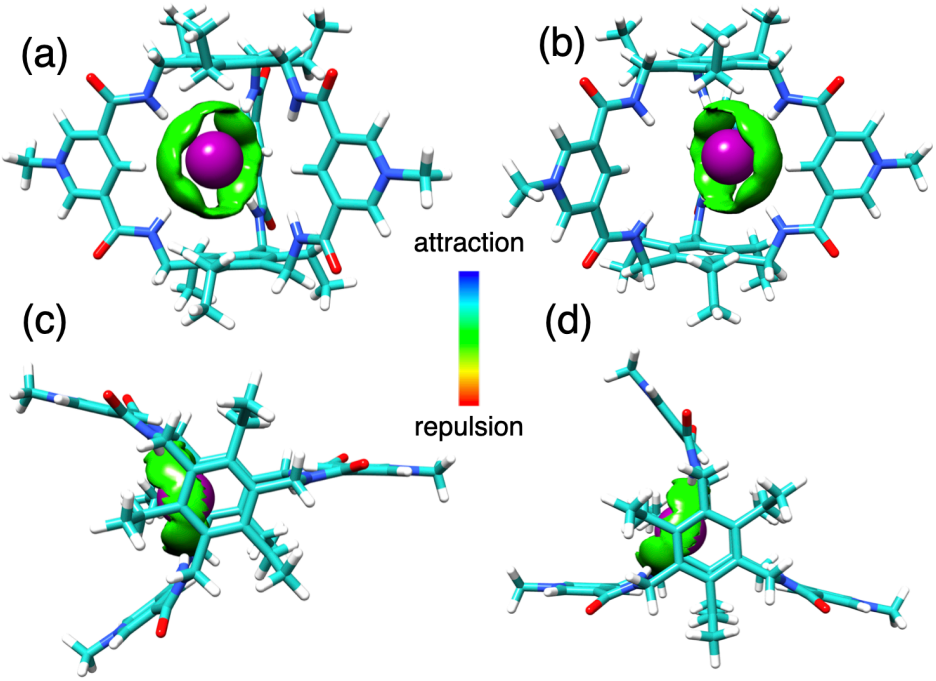

Fig. S74. Front (a), side-on (b), top (c), and bottom (d) view of $I^{-}\subset TPPC^{3+}$ from IGM analysis showing a noncovalent interaction isosurface of δg^{inter} = 0.003 a.u; color coding in the electron density range of –0.05<sign (λ_2)ρ <+0.05 a.u.

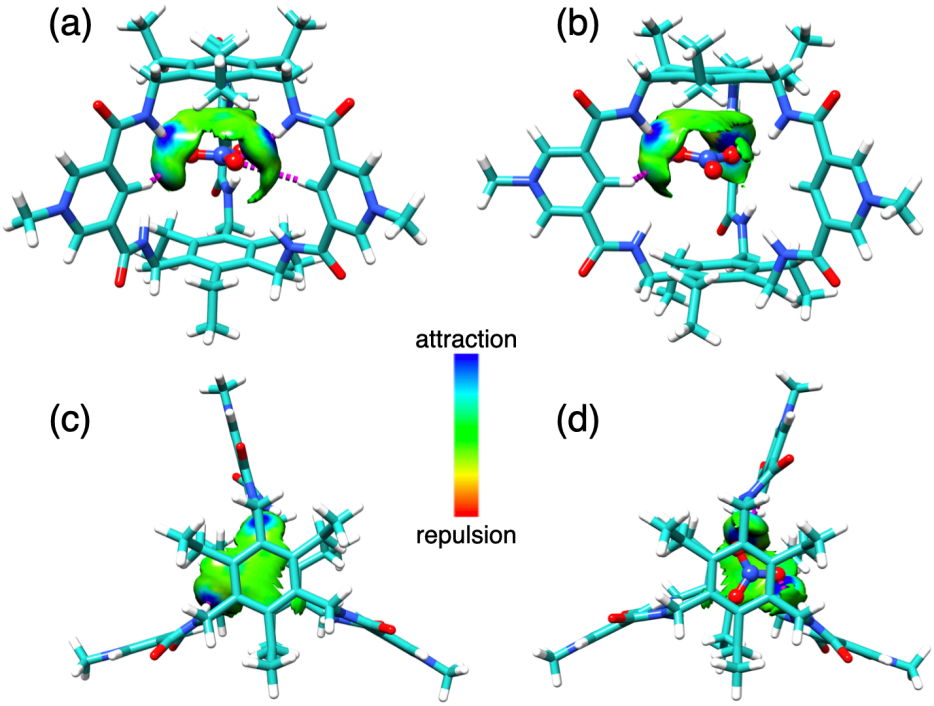

Fig. S75. Front (a), side-on (b), top (c), and bottom (d) view of NO_3^-⊂TPPC^{3+} from IGM analysis showing a noncovalent interaction isosurface of δg^{inter} = 0.003 a.u; color coding in the electron density range of –0.05<sign (λ_2)ρ <+0.05 a.u.

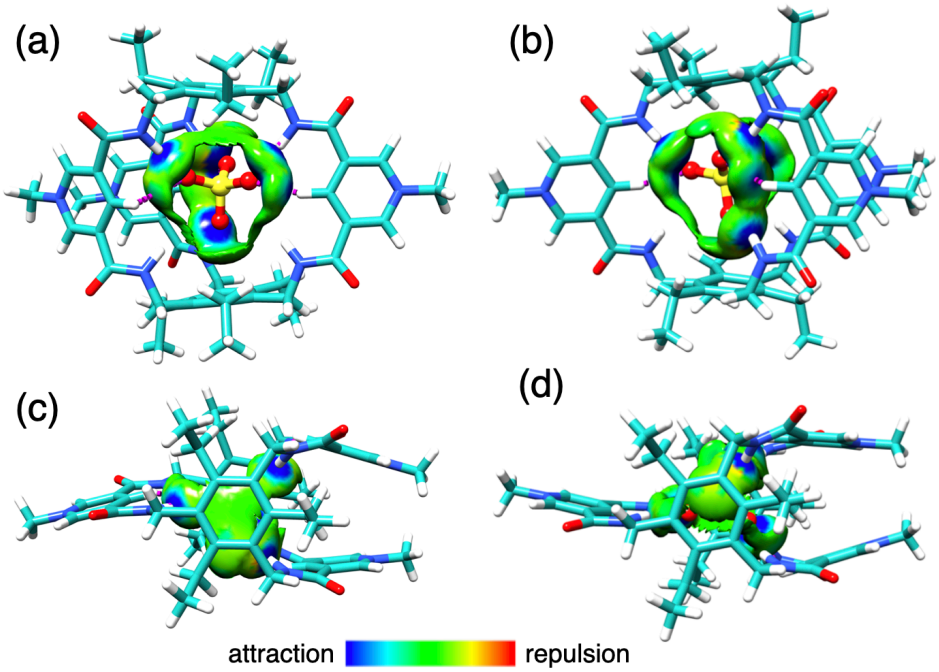

Fig. S76. Front (a), side-on (b), top (c), and bottom (d) view of SO_4^{2-} ⊂TPPC^{3+} from IGM analysis showing a noncovalent interaction isosurface of δg^{inter} = 0.003 a.u; color coding in the electron density range of –0.05<sign (λ_2)ρ <+0.05 a.u.

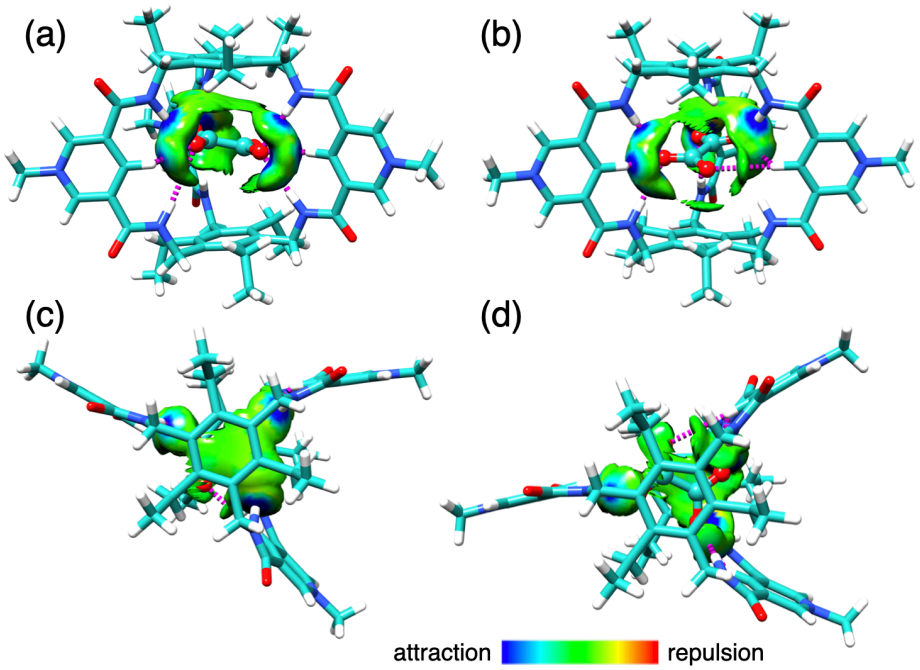

Fig. S77. Front (a), side-on (b), top (c), and bottom (d) view of $C_2O_4^{2-}$⊂TPPC^{3+} from IGM analysis showing a noncovalent interaction isosurface of $\delta g^{inter} = 0.003$ a.u; color coding in the electron density range of $-0.05 < \text{sign}(\lambda_2)\rho < +0.05$ a.u.

9. References

S1 D. Brynn Hibbert and P. Thordarson, *Chem. Commun.*, 2016, **52**, 12792–12805.
S2 P. Thordarson, *Chem. Soc. Rev.*, 2011, **40**, 1305–1323.
S3 APEX4 Software / Chemical Crystallography Bruker, Madison, Wisconsin, USA. 2022.
S4 Bruker SAINT Bruker AXS LLC, Madison, Wisconsin, USA.
S5 L. Krause, R. Herbst-Irmer, G. M. Sheldrick and D. Stalke, *J Appl Crystallogr*, 2015, **48**, 3–10.
S6 G. M. Sheldrick, *Acta Crystallogr A Found Adv*, 2015, **71**, 3–8.
S7 G. M. Sheldrick, *Acta Crystallogr C Struct Chem*, 2015, **71**, 3–8.
S8 O. V. Dolomanov, L. J. Bourhis, R. J. Gildea, J. A. K. Howard and H. Puschmann, *J Appl Crystallogr*, 2009, **42**, 339–341.
S9 A. L. Spek, *Acta Crystallogr E Cryst Commun*, 2020, **76**, 1–11.
S10 F. Neese, *WIREs Comput Mol Sci*, 2012, **2**, 73–78.
S11 A. D. Becke, *The Journal of Chemical Physics*, 1993, **98**, 5648–5652.
S12 F. Weigend and R. Ahlrichs, *Phys. Chem. Chem. Phys.*, 2005, **7**, 3297.
S13 H. Kruse and S. Grimme, *The Journal of Chemical Physics*, 2012, **136**, 154101.
S14 S. Grimme, J. Antony, S. Ehrlich and H. Krieg, *The Journal of Chemical Physics*, 2010, **132**, 154104.
S15 F. Weigend, *Phys. Chem. Chem. Phys.*, 2006, **8**, 1057.
S16 R. Izsák and F. Neese, *The Journal of Chemical Physics*, 2011, **135**, 144105.

S17 G. L. Stoychev, A. A. Auer and F. Neese, *J. Chem. Theory Comput.*, 2017, **13**, 554–562.
S18 C. Lefebvre, G. Rubez, H. Khartabil, J.-C. Boisson, J. Contreras-García and E. Hénon, *Phys. Chem. Chem. Phys.*, 2017, **19**, 17928–17936.
S19 T. Lu and F. Chen, *J Comput Chem*, 2012, **33**, 580–592.
S20 E. F. Pettersen, T. D. Goddard, C. C. Huang, G. S. Couch, D. M. Greenblatt, E. C. Meng and T. E. Ferrin, *J Comput Chem*, 2004, **25**, 1605–1612.